Doctoral Thesis
Pablo Sobrón Sánchez
Valladolid, June 2008

Acidic Aqueous Solutions and Sulfate-Rich Mineralogy: Raman Investigations of Rio Tinto, Spain, a Model for Acid Mine Drainage and a Potential Martian Analog

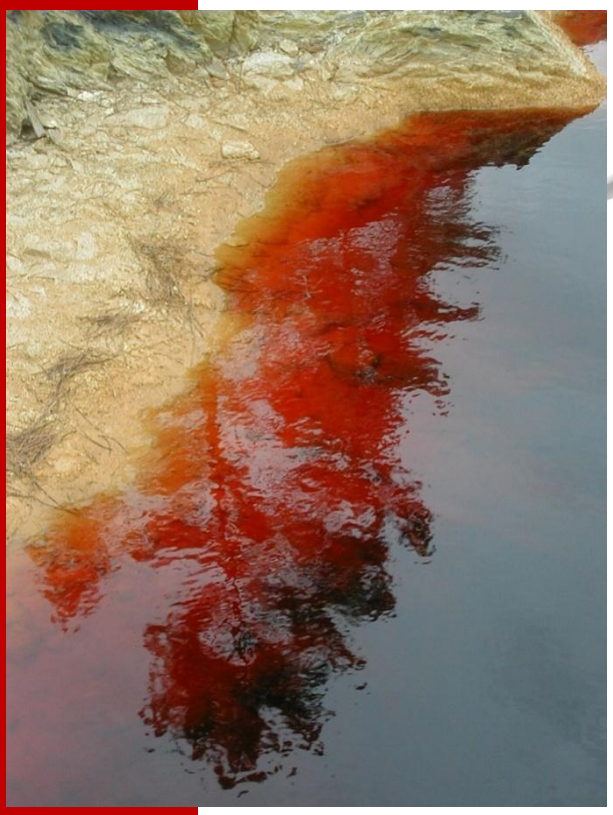

University of Valladolid
UVa

Departamento de Física de la Materia Condensada, Cristalografía y Mineralogía.
Facultad de Ciencias, Universidad de Valladolid

Acidic Aqueous Solutions and Sulfate-Rich Mineralogy: Raman Investigations of Rio Tinto, Spain, a Model for Acid Mine Drainage and a Potential Martian Analog

Thesis submitted by Pablo Sobrón Sánchez to obtain the degree
of Doctor Europeus from the University of Valladolid, Spain

Directors: Fernando Rull Pérez, Francisco Sobrón Grañón

Valladolid, Spain, June 2008

Acknowledgments

When I was suggested to pursue a PhD at the University of Valladolid, I didn't realize the magnitude of the enterprise I was getting into. Many ideas, many projects, many dreams that one way or another have crystallized in this dissertation, but only through the invaluable inputs from countless people I am indebted to.

Claus J. Nielsen spent innumerable hours of effort, concentration, advises and criticisms to the challenges we proposed. Ulrich M. Eide worked tirelessly to lead them to safe port. Tusen takk venner.

I felt like at home when working with Janice L. Bishop. She provided, and still does, the support that only someone with personal and scientific skills like hers is able to offer. This work would have been much weaker without the collection of samples and the collection of knowledge supplied by Charles N. Alpers. David F. Blake, Philippe Sarrazin and Will Brunner brought the valuable point of view of the X-rays. Gracias amigos.

Shiv K. Sharma and Anupam Misra offered me their enthusiastic support and spared no efforts to get the most out of my short visit to their lab. Mahalo hoapili.

As always, Aurelio Sanz and Jesús Medina have worked hard recording dozens of spectra, contributing suggestions, and keeping the coherence despite the rapid pace of work. Fernando Rull y Francisco Sobrón inspired me with the characteristic features of two privileged persons, two great men. Thank you guys.

I owe a lot to Clarisa. She supported my project and collaborated with the design of this thesis to the smallest detail. ;)

The Ministry of Education and Science (MEC), the Research Council of Spain (CSIC), and the Centro de Astrobiología (CAB) have partially funded this thesis. The Research Council of Norway (Norges forskningsråd), the NASA Astrobiology Institute (NAI), the American Philosophical Society (APS), and the University of Valladolid (UVa) facilitated several research stays overseas. Additionally, the NAI, the European Space Agency (ESA), the Research Council of France (CNRS), the International Union of Pure and Applied Chemistry (IUPAC) and the European Astrobiology Network Association (EANA) have allowed me to attend numerous international courses and conferences through travel grants, which have contributed to a great extent to improve the quality of this work.

Table of Contents

Contents

Tabla de Contenidos

Contenidos

Figure Index

Table Index

Scope and structure

Sulfate minerals are found in the Earth and can be associated with volcanism, hydrothermalism, evaporation, or mining. The natural process of acid rock drainage (ARD) is often intensified by such activities. For instance, as a result of mining, large amounts of sulfides are exposed to water, air, and often microbes that catalyze the oxidation. As a consequence, waters currently draining oxidized sulfide deposits and mine-waste sites have particularly high concentrations of dissolved sulfate and metals. Contamination of natural waters by acid mine drainage (AMD) has a negative impact in the surrounding environments. On the other hand, the discovery of jarosite on Mars as indicative of the likely existence of a former acidic Martian environment, and its association with other water-related minerals (for instance gypsum, kieserite and bassanite) awakens astrobiological interest. Mars sulfate mineralogy may provide the best means for the understanding of ancient aqueous environments comprising a pre-biotic chemistry, or even hosting ancient life.

We believe that a characterization of the hydrogeochemistry of sulfate-rich sites is crucial in order to describe all of the different processes and settings of iron and sulfate deposition on Earth, serving a double purpose: (1) to describe the environmental impact of AMD, predicting the potential/evolution of AMD sites, and shaping AMD remediation strategies and (2) to develop and to refine analytical and instrumental techniques for the search and understanding of Exo/Astrobiology as well to determine constraints on the Martian mineralogy and surface processes.

Rio Tinto (SW Spain) environment is a sound example of AMD environments, and is accepted by some as a geo/bio/mineralogical setting on our planet which offers comparable scenarios to those on Mars, and where technologies for Martian exploration can be defined and tested.

Raman spectroscopy is regarded as a powerful characterization technique for the sulfate systems due to its intrinsic features: it requires little or no sample preparation prior to spectra collection, and allows real-time identification of species in acidic waters and associated precipitates and very rapid quantification of their abundance, among others. Furthermore, recent advances in optics, lasers and

From left to right: Geographical location of the Mars analog sites targeted in this PhD thesis, image displaying the reddish/orange extremely acidic waters and iron sulfate efflorescences in Rio Tinto, Spain (photo by P.S.), and false color Pancam image of Cape Verde rock layers in Victoria Crater taken by MER Opportunity (image credit: NASA/JPL/Cornell), where iron sulfates are likely present.

detector systems allow for the development of compact field Raman instruments for *in-situ* analyses. This fact, together with the capabilities of the Raman spectroscopy for the unambiguous characterization of mineral phases and potential biosignatures, make the Raman technique an outstanding tool for the exploration of sulfate-rich areas, and most likely for the Martian surface and subsurface. A landmark for the technique is the selection of a Raman spectrometer as a *fundamental instrument* within the upcoming European Space Agency (ESA) ExoMars mission.

Considering the above-mentioned statements, the present PhD thesis focuses on a Raman spectroscopic characterization of the hydrogeochemistry of Rio Tinto. For this purpose, the following research strategy was established:

1. To characterize the natural acidic waters and the natural precipitate minerals and efflorescent salts from selected sites within the Rio Tinto area and to situate them in the context of precipitation and evaporation models (sequences) for the mineral phases.

2. To identify the primary chemical species, their basic equilibriums and association processes, and their transport phenomena in synthetic solutions with chemical compositions similar to those of the natural acidic systems of Rio Tinto.

3. To develop algorithms for the Raman data processing in order to design a robust methodology for qualitative and quantitative measurements on

the Raman spectra. This methodology is the basis for the thermodynamic analysis of the equilibriums and associated processes.

According to this scheme, this dissertation has been structured in six chapters, each of them containing the following information:

- Chapter 1 is an introductory chapter. The geological, chemical and historical framework of the Rio Tinto area is reviewed, including mineralogy, hydrochemistry and the biogenic processes acting in the river as a driving force for mineral precipitation.

- Chapter 2 is an overview of the Raman technique fundamentals, as well as a description of the Raman-based equipment used for the experiments. Complementary techniques and instruments used in this PhD are briefly described.

- Chapter 3 deals with the problem of the Raman data processing. Algorithms developed for obtaining the maximum information from the Raman spectra are presented, including filtering, baseline removal, signal-to-noise improvement, band fitting and mineral identification against dedicated databases.

- Chapter 4 describes the investigations on acidic aqueous systems, both natural and synthetic. The diffusion properties of sulfuric acid and the physico-chemical structure of Rio Tinto-like aqueous synthetic systems are reported. The Raman spectroscopy of selected stream waters from Rio Tinto is discussed.

- Chapter 5 deals with the Raman spectroscopy of sulfate precipitates and efflorescences from Rio Tinto in micro mode. Additionally, the Raman spectroscopy of another AMD related site, the Richmond Mine in Iron Mountain (California) is presented. Finally, a combined

Raman/Reflectance/X-ray Diffraction study on Rio Tinto samples is reported.

- Chapter 6 presents an overview of the achievements of this thesis, conclusions and future lines of investigation.

Chapter 1

introduction: the historical and geo/biochemical framework of the Rio Tinto area, Spain

The Rio Tinto's (Spanish for Tinto (dark red) River) basin flows through the Iberian Pyrite Belt (Figure 1.1), one of the world biggest formations of sulfur complexes (Boulter, 1996; Leistel *et al.*, 1998). The Iberian Pyrite Belt is more than 250 km long with maximum width of 75 km. More than 80 massive-sulfur deposits have been detected, along with 300 manganese deposits (Mellado *et al.* 2006). The Rio Tinto mines are perhaps the oldest mines in the world. At least, their mineral wealth was legendary already in the Bronze Age. According to the myth, these are "the fabled mines of King Solomon", but aside legends, it is a fact that the Great Britain-based Rio Tinto Company made the Rio Tinto mines one of the most important suppliers of iron, copper and sulfur in the world (Avery, 1974). Figure 1.2 shows a picture of an opencast mine named Corta Atalaya. With its 1200 m long, 900 m wide and 350 m deep pit, it is considered Europe's biggest open-cast mine. Corta Atalaya was probably the most ambitious project of the Rio Tinto Company, and was mined until the early 1980s. The satellite picture in Figure 1.3 displays an area of some 900 km^2, which gives an idea of the dimension of the mining developed in the site.

The 5000 years-lasting mining (Avery, 1974) in the area was thought to be the direct cause of the river's unusual acidity (mean pH 2.3 (Amils *et al.* 2002)) and reddish color. The surface and subsurface minerals give the soil of the region shades of blue, green, yellow, red and brown (Figures 1.4 to 1.8). A picture of the chemical processes of acid mine drainage (AMD), and in particular of the Rio Tinto environment can be summarized in the following chemical reactions (Nordstrom *et al.*, 2000):

$$2FeS_2 + 7O_2 + 2H_2O \rightarrow 2FeSO_4 + 2H_2SO_4 \quad (1.1)$$

$$2Fe^{2+} + 1/2\ O_2 + 2H^+ \rightarrow 2Fe^{3+} + H_2O \quad (1.2)$$

$$Fe^{3+} + 3H_2O \rightarrow Fe(OH)_3 + 3H^+ \quad (1.3)$$

$$FeS_2\ (s) + 15/4\ O_2 + 7/2\ H_2O \leftrightarrow 4H^+ + 2SO_4^- + Fe(OH)_3\ (s) \quad (1.4)$$

Equation (1.1) depicts the oxidation of inorganic sulfur to sulfate with the subsequent production of sulfuric acid. The next step (Eqn (1.2)) shows how ferrous iron is oxidized to form ferric iron and water. When drainage containing these

Figure 1.1. Iberian Pyrite belt (yellow area)

pollutants reaches the stream, it becomes diluted and the pH of the solution rises. The increase in pH allows ferric hydroxide ($Fe(OH)_3$, "yellow-boy") to precipitate out. This chemical reaction is illustrated in Eqn (1.3). As indicated in Eqn (1.4), a net of four moles of hydrogen ions (H^+) are liberated for each mole of pyrite (FeS_2) oxidized, making this one of the most acidic weathering reactions known.

Water cleaning and recovery programs were prepared and funded in order to mitigate the environmental impact of the acid drainage from the mining sites (Serrano *et al.*, 1995). Particularly, aquatic plants and animals are highly damaged and groundwater supplies are contaminated as a consequence of AMD. However, not all of the aquatic life development is disrupted by AMD. The presence of chemolithotrophic organisms, such as iron-oxidizing bacteria and sulfur-oxidizing bacteria in Rio Tinto waters was first reported by López-Archilla *et al.* (1993). Large amounts of Fe^{3+} are found in Rio Tinto's water (Allen *et al.*, 1996; Amils *et al.* 2002; Fernández-Remolar *et al.*, 2005), but abiotic oxidation of Fe^{2+} is a very slow process (Singer and Stumm, 1970). *Thiobacillus ferrooxidans*, an iron and sulfur-oxidizing bacteria is known to

Figure 1.2. Picture of Corta Atalaya open-cast mine in the 1980's (left) and nowadays (right; credit T. Acosta)

catalyze these reactions at low pH, increasing reaction rates by several orders of magnitude (Nordstrom and Southam, 1997; López-Archilla *et al.*, 2001).

The oxidation/reduction processes described in Eqns (1.1) to (1.4) are known to occur naturally (Runnells *et al.*, 1992). In fact, the acid rock drainage is a natural process; however human activities such as mining dramatically accelerate these geochemical reactions rates by providing greater exposure of minerals to air and water through mine workings, waste rock and tailings. In the case of Rio Tinto, minerals are also exposed to the local microbial diversity. These microorganisms are thought to be more than just spectators of the oxidation-reduction processes occurring in the Rio Tinto environment and, actually, they play a very active role in this game and are believed to be the true culprits to Rio Tinto today's condition (López-Archilla *et al.*, 2001; Amils *et al.*, 2002). The iron and sulfur oxidation/reduction cycles and the

Figure 1.3. Satellite picture of the Rio Tinto mine area. Corta Atalaya pit can be observed in the mid-left part of the picture. White-to-gray areas are mine-weathered extensions of land in the search for iron ore, copper, silver and other mineral ores

participation by different microorganisms in the processes have been nicely cartooned by Amils *et al.* (2002). Most of this microbial community has been described as autotrophic, thus suggesting that its interaction with the environment is the main source of the extreme conditions of the Rio Tinto environment.

The discovery of ferric hydroxides/oxyhydroxides, jarosites (iron-bearing sulfates thought to have formed via aqueous activity) and other sulfate-bearing minerals in the Meridiani region provides strong evidence that liquid water once flowed on the Martian surface (Klingelhöffer *et al.*, 2004; Rieder *et al.*, 2004; Lane *et al.*, 2004; Clark *et al.*, 2005). It is suggested that sulfate deposits enriched in iron and mixed iron oxy-hydroxide were precipitated from meltwaters (Burns *et al.*, 1984), thought to have been acidic (Clark and van Hart., 1981). Most recently, Knoll *et al.* (2005) proposed other alternatives for the formation of sulfate-bearing minerals in Meridiani. For instance, iron(III)-rich hydrated sulfates from oxidized sulfides observed in the

Figure 1.4. Dark red water near the river's source and yellow/white efflorescences

outcrops at Meridiani may occur as a result of long-term reactions, none of them requiring the presence of biology. Also hydrothermalism and volcanism could have played a role shaping the Meridiani surface conditions. Thus the definition of Rio Tinto as a terrestrial Martian analog in terms of mineral paragenesis must be regarded with caution.

However, given the association of microorganisms such as *Acidithiobacillus ferrooxidans* with the aqueous oxidation of sulfides in Rio Tinto, and whether sulfates on Mars may have been formed or not through biomediated pathways, deposits of sulfate precipitates on Mars may be ideal sites to search for extinct life on that planet. For this purpose, Rio Tinto provides a very important scenario where the processes (both biomediated and inorganic) by which sulfates occur on Earth can be fully characterized and understood. Additionally, Rio Tinto is an outstanding testing ground for the development and refinement of new technologies and instruments for the

Figure 1.5. Tinto's watercourse heading South, towards the Atlantic Ocean

search and understanding of Exo/Astrobiology, as shown during the course of NASA's M.A.R.T.E. project (Mars Astrobiology Research and Technology Experiment, 2005). A robotic drill that might one day be used on Mars was tested out at the edge of the Peña de Hierro (Spanish for iron crag) mining pit in Rio Tinto shown in Figure 1.9.

Figure 1.6. Dark red water and a beach of white sulfate efflorescences

Figure 1.7. Reddish/yellowish water at the exit of a former mine tunnel

Figure 1.8. Yellowish-to-orange acidic water evaporates leaving crusts of precipitates (from less soluble to more soluble salts) in the stones

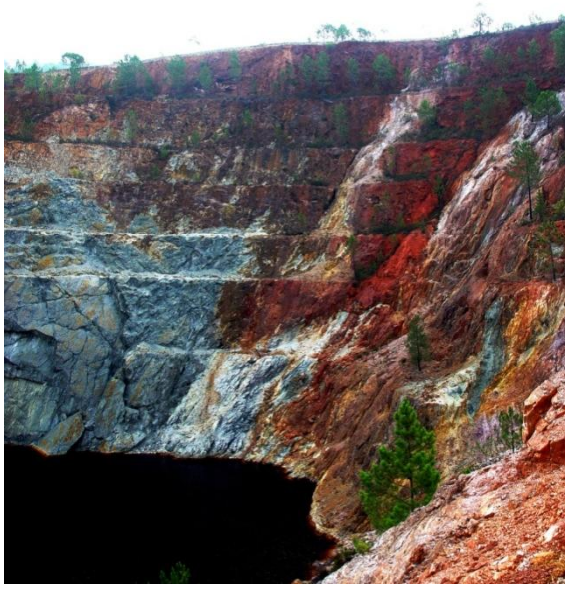

Figure 1.9. Peña de Hierro, considered one of the sources of the river

Chapter 2

introduction: methods and instruments

This chapter gives an overview of the Raman spectroscopy fundamentals. The Raman equipment used for the experiments related to this PhD is described. VNIR reflectance and X-ray diffraction are introduced as complementary analysis techniques. The Raman spectroscopy of the sulfate ion is also described.

2.1. Raman spectroscopy fundamentals

Raman spectroscopy is a technique that has experienced a tremendous revival due to technological advances in lasers, detectors and spectroscopic optical systems. The inelastic scattering of light was first demonstrated by Sir Chandrasekhara Venkata Raman (Raman and Krishnan, 1928) and independently by Grigory Landsberg and Leonid Mandelstam (Landsberg and Mandelstam, 1928).

When light strikes a sample, a small fraction of the incident photons (10^{-5} to 10^{-9}) interacts with vibrations in the sample and is scattered at higher or lower energy (Raman scattered). Raman spectroscopy involves the measurement of the difference in energy between the incident light and the Raman scattered photons, which corresponds to the energy of the vibrational transitions.

From a classical point of view, the interaction can be regarded as a perturbation of the molecule's electric field. The quantum mechanics approach describes the scattering as an excitation to a virtual state lower in energy than a real electronic transition with nearly coincident de-excitation and a change in vibrational energy. The scattering event occurs in the order of 10^{-14} seconds. The virtual state description of scattering is shown in Figure 2.1.

A Raman spectrum is a plot of the intensity of Raman scattered radiation as a function of its frequency difference from the incident radiation (usually in units of wavenumbers, cm^{-1}). This difference is called the Raman shift. Note that, because it is a difference value, the Raman shift is independent of the frequency of the incident radiation.

A typical Raman spectrometer is made up of three basic parts: the laser, the collection device, and the spectrograph.

- Laser: A laser is used to excite Raman spectra because it gives a coherent beam of monochromatic light. This gives sufficient intensity to produce a useful amount of Raman scattered light and allows for clean spectra, free

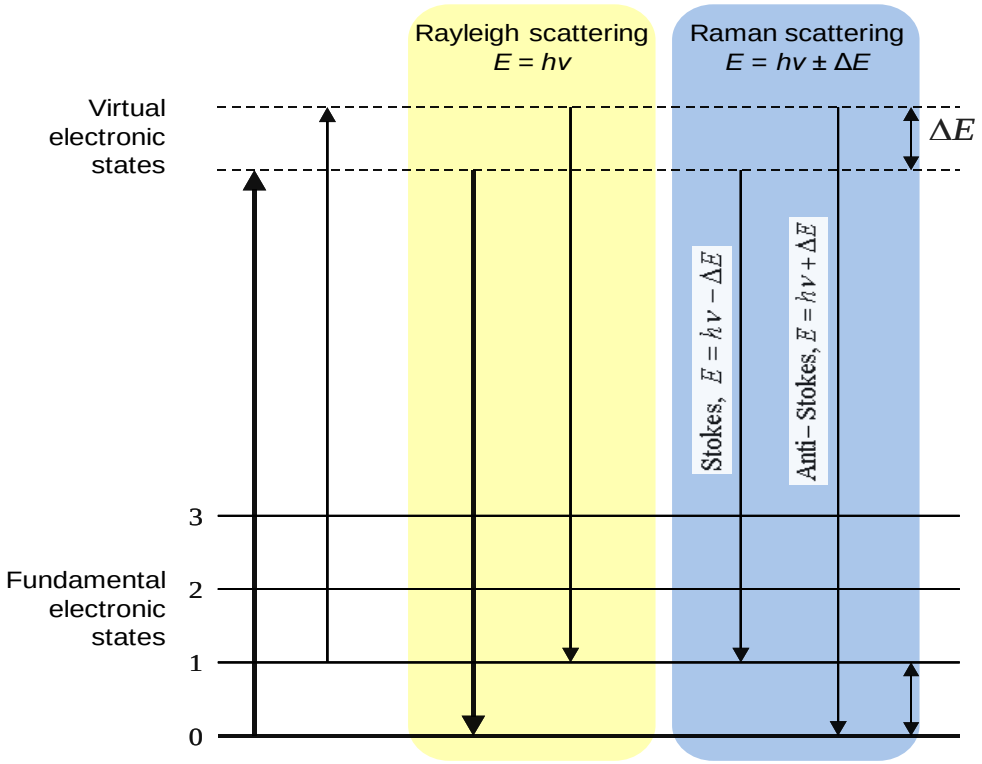

Figure 2.1. Energy level diagram explaining the Raman scattering processes

.

of extraneous bands. Lasers used for Raman spectroscopy must exhibit good wavelength stability and low background emission.

- Probe: The probe is a collection device that collects the scattered photons, filters out the Rayleigh scatter and any background signal from the fiber optic cables, and sends the Raman scattered light into the spectrograph. Many probes also focus and deliver the incident laser beam.

- Spectrograph: When Raman scattered photons enter the spectrograph, they are passed through a diffraction grating to separate them by wavelength and passed to a detector (PMT, CCD, ICCD, etc) which records the intensity of the Raman signal at each wavelength.

This section does not attempt to treat Raman theory and instrumentation in depth. Excellent books explain the details of the Raman technique (Woodward, 1967;

Chantry, 1971; Gilson and Hendra, 1972; Clark, 1975; Long, 1977). Instead we focus on the Raman spectroscopy of an exceedingly important molecule in this PhD thesis, the sulfate molecule, and on the Raman instrumentation used for the experiments concerning this thesis.

2.2. Raman spectroscopy of the sulfate ion

The sulfate ion is a polyatomic anion with the empirical formula SO_4^{2-} and a molecular mass of 96.06 daltons; it consists of a central sulfur atom surrounded by four equivalent oxygen atoms in a tetrahedral arrangement. The sulfate ion carries a negative two charge and is the conjugate base of the bisulfate (or hydrogen sulfate) ion, HSO_4^-.

The free sulfate ion belongs to the high-symmetry pointgroup T_d. All the four fundamentals are Raman active (Nakamoto, 1997). Figure 2.2 displays the four normal vibrations of the sulfate ion.

Raman spectral studies of sulfate and bisulfate ions in aqueous solutions, including their equilibriums, have been reported by many workers (*e.g.* Irish and Chen, 1970; Chen and Irish, 1971a, 1971b; Dawson *et al.*, 1986; Cox *et al.*, 1987; Rull *et al.*, 1995; Myhre *et al.*, 2003). All these works share a similar band assignment for both sulfate and bisulfate ions' molecular vibrations. Table 2.1 shows the normal vibrational modes of sulfate and bisulfate along with the bands assignment used in this thesis.

If the symmetry of the ion is lowered by solvation, metal complexation, or protonation, the vibrational degeneracy is enhanced and the degenerate vibrations split. As a consequence, the T_d symmetry of the sulfate ion may be reduced to either C_{3v} , C_{2v}, or C_s (Nakamoto, 1997). Changes in the Raman spectrum of sulfate associated with those symmetry changes may be explained by means of group theory (Nakamoto, 1997). From the experimental point of view, Chio *et al.* (2005) and Wang *et al.* (2006) showed that the fundamental sulfate stretching vibration modes show a systematic

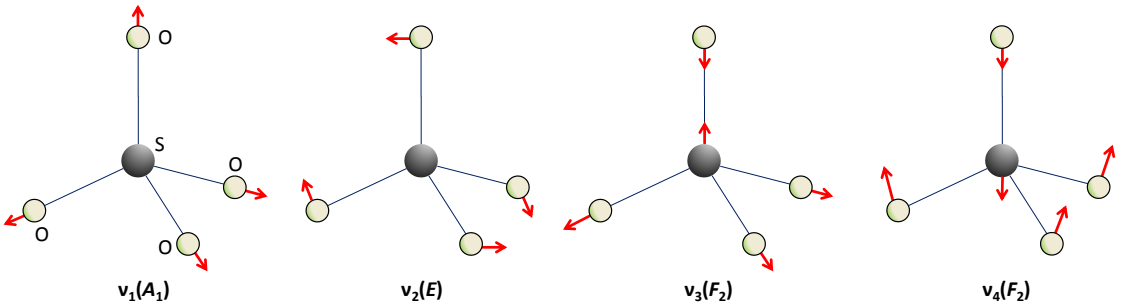

Figure 2.2. Normal vibrational modes of the sulfate ion. (Modified from Nakamoto, 1997)

.

peak-position shift toward lower wavenumbers when the hydration state increases. Raman peak shifts are also observed for the same vibration mode, and may be correlated to the ionic radius of the substitution cation in jarosites (Sasaki, 1998). Frost *et al.* (2000, 2005, 2006b) reported exhaustive Raman spectral studies on different types of sulfate minerals, both natural and synthetic. Nonetheless, is well known that the Raman spectra of natural samples differ considerably from the spectra of synthetic samples. Further, variable paragenesis and weathering conditions of the sulfate minerals and different experimental geometries, instrumentation, etc, are certainly reflected in the Raman spectra. For this reason, instead of relying on band assignations for the sulfate molecule from the literature, we have analyzed the Raman spectra of minerals in a sample-by-sample basis, searching for the spectral fingerprints of well-known molecular structures.

Table 2.1. Vibrational modes and wavenumbers (cm^{-1}) of the sulfate and bisulfate ions

Chemical species	ν_1 (symmetric stretching)	ν_2 (symmetric bending)	ν_3 (asymmetric stretching)	ν_4 (asymmetric bending)	Reference
SO_4^{2-}	983	450	1105	611	Nakamoto, 1997
HSO_4^-	885	422/480*	1051	595	Haldna *et al.*, 1987
					Myneni, 2000

*This vibrational mode of the bisulfate is characterized by two broad bands arising from the symmetry breakdown in the sulfate molecule due to the presence of hydrogen units within the molecular structure

2.3. Raman instrumentation

Several Raman instruments have been used during this work in order to maximize the experimental throughput. The characteristics of the samples and the nature of the analysis to perform were determining factors when choosing the right instrument among those available. Attending to the configuration of the spectrograph, two types of instruments were used: axial transmissive spectrograph configuration with holographic grating, and Czerny-Turner spectrographs. The principles of operation of both systems are sketched in Figure 2.3.

2.3.1. University of Valladolid, Spain

The Raman equipment at the University of Valladolid (ERICA: Grupo de Espectroscopía Raman e IR en Cosmogeoquímica y Astrobiología) used for this work is composed by the following elements:

- *Laser*: Research Electro-Optics model LSRP-3501; He-Ne, 35 mW @632.8 nm.
- *Spectrograph*: KAISER model HoloSpec f/1.8i with fixed transmission grating suitable for 633 nm; spectral range: 200-3800 cm^{-1}; maximum resolution 4 cm^{-1}.
- *Detector*: Andor CCD model iDus DV420A-OE-130; 1024×128 active pixel; 26× 26 μm^2 pixel size.
- *3D motion stage*: Prior Proscan II model H30V4; programmable motion.
- *Microscope*: Nikon model Eclipse E600; 10, 20, 50 and 100× magnification.
- *Raman probe*: Jobin-Yvon 633 nm, UMS type.

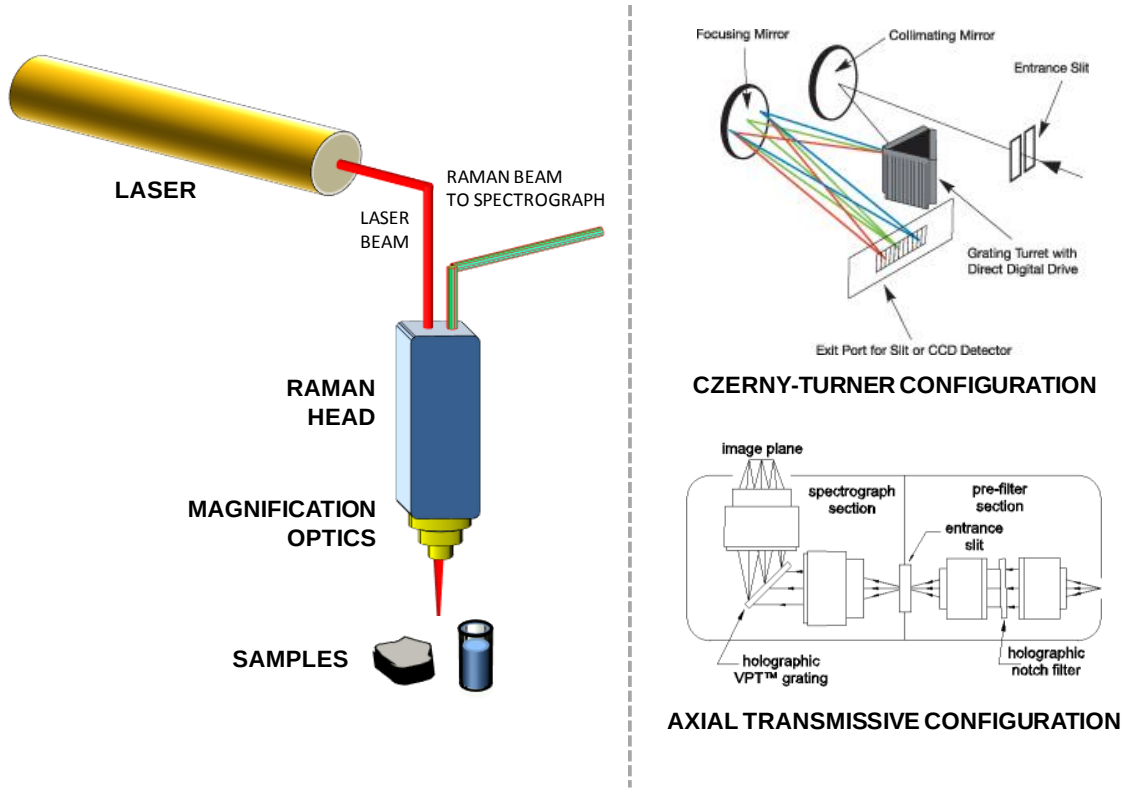

Figure 2.3. Typical configuration of a Raman experiment (left) and the two spectrograph configuration used in this work (top figure from Andor Technology PLC (2008); bottom figure from Kaiser Optical Systems Inc. (2008)

- *Imaging camera*: CCD microscope camera JVC model TK-C1381EG PAL; 768x576 resolution.

The experiments described in section 5.3 were carried out using this equipment. A picture of the instrument is shown in Figure 2.4.

2.3.2. University of Oslo, Norway

The Raman equipment at the University of Oslo (Department of Chemistry) used for this work is composed by the following elements:

- *Laser*: Spectra-Physics Millenia diode pumped solid state laser; 12 W @ 532 nm.

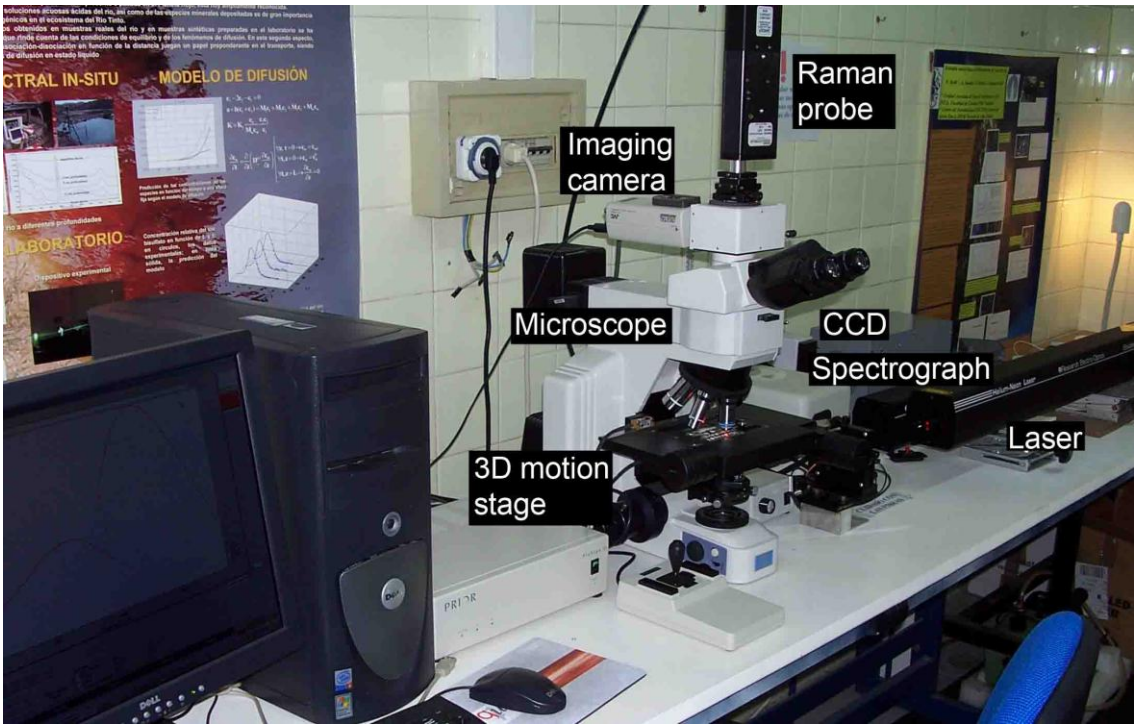

Figure 2.4. Picture of the Raman equipment at the group ERICA, University of Valladolid

.

- *Spectrometer*: Jobin Yvon T64000 spectrometer including microscope with motorized XYZ-stage; spectral range 250 to 1200 nm; maximum resolution 0.2 cm^{-1}.

- *Raman probe*: Raman Superhead Horiba Jobin-Yvon for 532 nm.

Experiments in sections 4.2, 4.3, and 4.4 were carried out using this equipment. A picture of the instrument is shown in Figure 2.5.

2.3.3. University of Hawaii at Manoa, Hawaii, USA

The Raman equipment at the University of Hawaii at Manoa (HIGP: Hawaii Institute for Geophysics and Planetology) used for micro-Raman investigations is a WiTec alpha300 R system which combines a confocal microscope provided with a feedback-controlled, piezo-driven XYZ-scan stage, with a very sensitive spectroscopy system. A frequency-doubled solid-state Nd:YAG laser at 532 nm (also provided by

Figure 2.5. Picture of the Raman equipment at the University of Oslo

WiTec) is used as the excitation source. Experiments in sections 4.5 and 5.2 were carried out using this instrument. Figure 2.6 shows a picture of the instrument with all its components.

2.3.4. SETI Institute, Mountain View, California, USA

The Raman equipment at SETI Institute (Mountain View, California) is a Renishaw inVia microscope. In integrates a XYZ motorized positioning stage and an extremely sensitive dispersive spectrometer. The system is also equipped with multiple lasers, with automatic software switching of excitation wavelength. The experiments in

Figure 2.6. Picture of the Raman equipment at the HIGP, University of Hawaii at Manoa

section 5.4 were carried out using this instrument with the 633 nm laser source. Figure 2.7 shows a picture of the instrument.

2.4. Complementary techniques

2.4.1. Visible Near-Infrared Reflectance (VNIR) spectroscopy

When solar radiation hits a target surface, it may be transmitted, absorbed or reflected. What wavelengths are absorbed and what reflected depend on the material. A visible/near infrared (VNIR) reflectance spectrum of a material is a plot of the fraction of radiation reflected as a function of the incident wavelength and serves as a unique signature for the material. Therefore, a material can be identified from its spectral reflectance signature if the sensing system has sufficient spectral resolution.

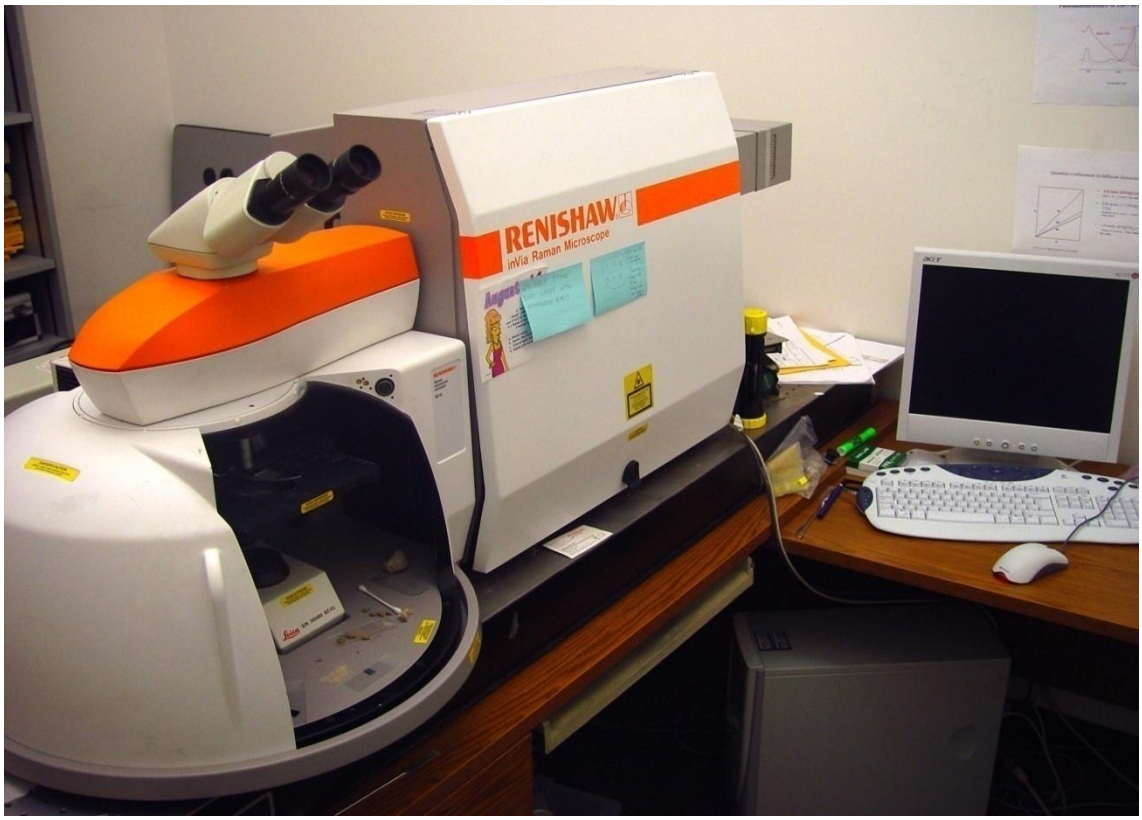

Figure 2.7. Picture of the Raman equipment at the SETI institute

The VNIR spectra were measured in the present PhD using a FieldSpec®ProFR from Analytical Spectral Devices (ASD) with a contact probe and solar simulated light source. Figure 2.8 shows a picture of the instrumental set-up for laboratory spectra collection.

2.4.2. X-ray diffraction

XRD is a powerful technique to accurately identify both elemental composition and crystallographic orientation. When X-rays interact with a crystalline substance, one gets a diffraction pattern. While the correlation function in Raman spectroscopy is a temporal function, in XRD it is a space function. The scattered X-rays contain both angular and intensity information. The main use of powder diffraction is to identify

Figure 2.8. Picture of the field portable VNIR equipment used at the SETI institute. Photograph by Janice L. Bishop

components in a sample by a search/match procedure. Furthermore, the areas under the peak are related to the amount of each phase present in the sample. Definitive mineralogical analysis through the determination of crystal structure (*i.e.*, powder XRD) is the standard to which all other techniques are compared. On Earth, about 6,500 minerals are recognized by the International Mineralogical Association.

The XRD system used for the analyses of mineral samples along this PhD thesis is the portable Terra (inXitu Inc.) XRD system for rock and mineral analysis. The instrument is also known as "mini-Chemin" since it relies on the same concept as the Chemin IV (a field portable version on the Chemin instrument onboard NASA's MSL) although it has been completely reconfigured relative to it (Sarrazin *et al.* 2007).

Further information concerning this instrument can be found elsewhere (inXitu Rock and Mineral Analyzer, 2008). Figure 2.9 shows a picture of the Terra instrument while analyzing sulfate efflorescences from Iron Mountain Mine (California).

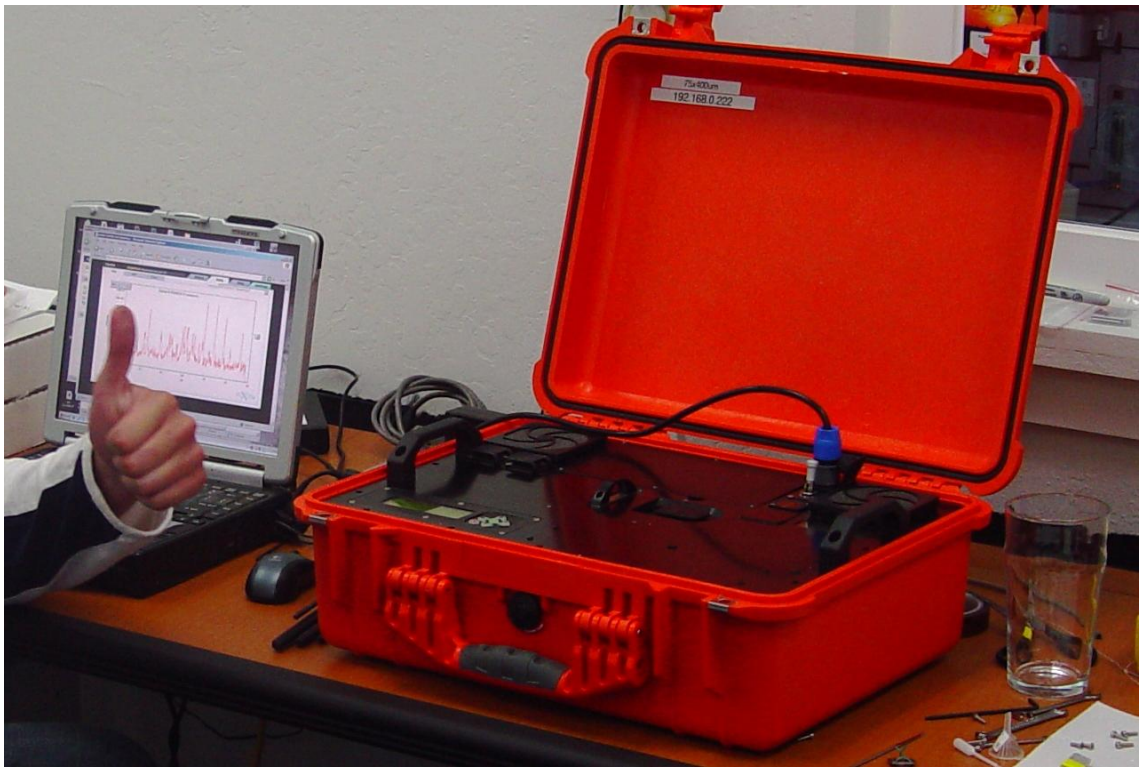

Figure 2.9. Picture of Terra XRD system at inXitu Inc. headquarters at Mountain View, California

Chapter 3

software development

This chapter presents the analytical tools developed for Raman data post-processing. Routines for baseline correction, de-noising, Fourier self-deconvolution, band-fitting, and band identification of the Raman spectra are described and discussed.

3.1. Introduction

A typical Raman spectrum can be regarded as the output, in the form of a signal, to a certain input given by a physical device. In most cases, the input is composed not only by information from the sample but by background signals. Besides, the measurement systems introduce certain noise which is invariably reflected in the spectra as a baseline, although it could contribute in many other ways. As a consequence, a Raman spectrum (Figure 3.1) results as the combination of a deterministic signal, or Raman information from the sample and other contributions. Particularly, noise and baseline (background) are of great importance.

In the following sections we show the mathematical and physical basis of the software package developed for minimizing the impact of noise and background signals in the Raman spectrum, and therefore obtaining the maximum information from the Raman spectra. Automated band-fitting routines, as well as mineral search-match algorithms are also included in the software package for obtaining critical Raman band parameters and identification of spectral fingerprints against a mineral database, respectively.

3.2. Signal-to-noise ratio improvement

A Raman spectrum is the consequence of the diffraction phenomenon of a real process, the Raman effect. It is well known that the diffraction pattern of an object is the Fourier Transform (FT) of the object; thus a Raman spectrum can be considered as the FT of the Raman effect, and therefore is generally plotted as a function of the frequency, or the Raman shift. Strictly speaking, the plot of a Raman spectrum is a spectral power distribution.

Signal-to-noise ratio (SNR) improvement -or de-noising-, procedure must be preceded by an accurate characterization of the noise part of the signal. When a raw

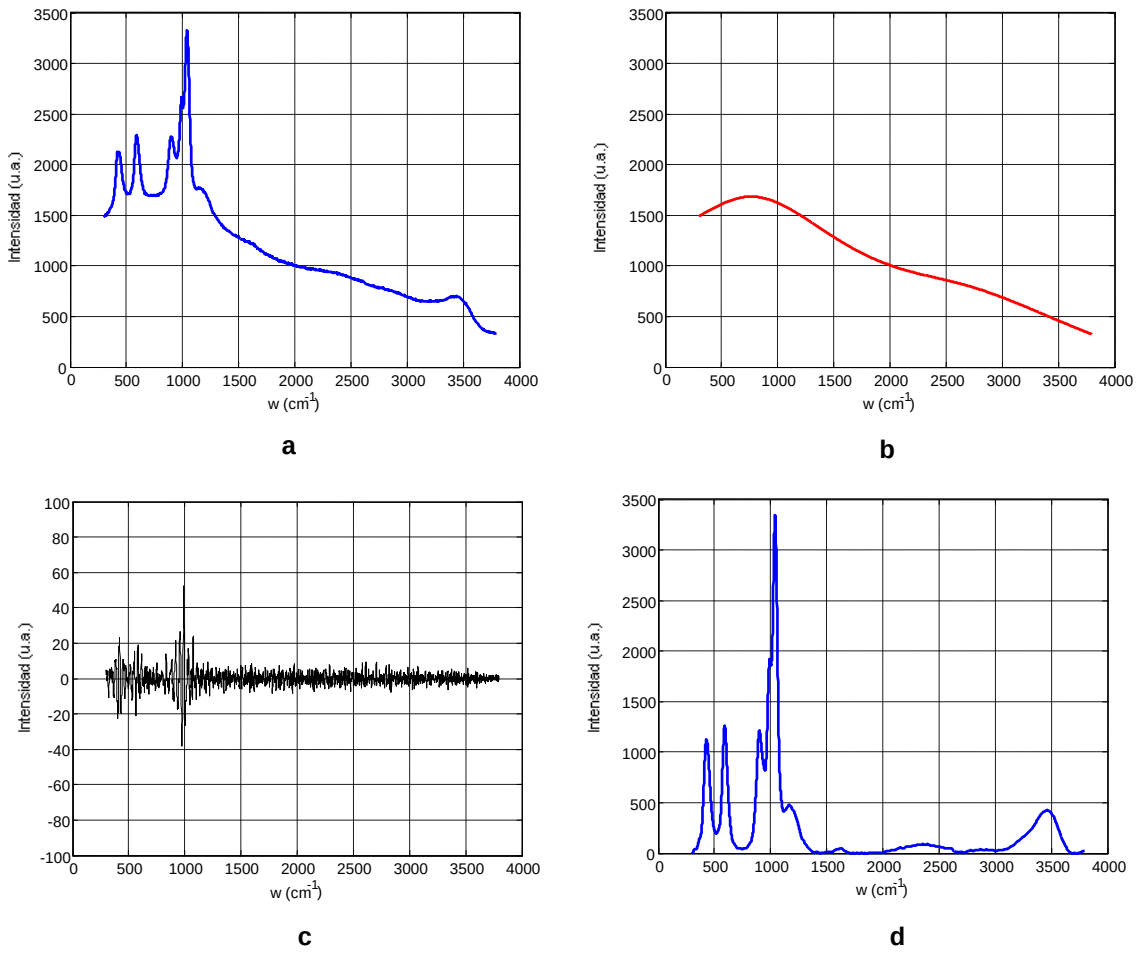

Figure 3.1. The Raman spectrum containing the information from the sample only (d) is obtained by subtracting the baseline (b) and the noise (c) to the raw spectrum (a)

Raman spectrum is plotted in the Raman shift/frequency-domain (FD), noise is a random signal distributed all over the spectral range, and overlaps to the Raman bands; however, in the Fourier transformed-domain, hereinafter time-domain (TD), noise is located in the short-time region whereas the Raman information is in the large-time region, as Fourier analyses suggests (Ewing, 1997). Frequency, *w*, and time, *t*, are related by the following expression:

$$t = 33.33\frac{2\pi}{w} \tag{3.1}$$

where *t* is given in picoseconds. By truncating the spectrum in the TD one can retain the signals arising from the Raman effect alone. The result in the FD is equivalent to that of a smoothing filter, since the blocked short times correspond to sharp intensity

changes, *i.e.* to the noise in the Raman spectrum. After the reverse FT is taken, the noise is considerably reduced whereas the Raman bands remain approximately the same. The use of a FT-based tool for de-noising allows for switching between the FD and the TD while preserving the physical sense of the Raman spectrum. This is the main reason why we have developed an algorithm based on the FT, or more precisely, on the Fast Fourier Transform (FFT) (Duhamel and Vetterli, 1990). Most commonly used methods for the de-noising of Raman spectra include the Savitzky-Golay algorithm (Savitzsky and Golay, 1967) and the Wavelet Transform (Chui, 1992). These techniques yield equivalent results as those of FFT while requiring longer computation times.

The three aforementioned operations: (1) FFT of the raw spectrum, (2) truncation of the transformed spectrum and (3) reverse FFT of the truncated spectrum are sequentially performed by our algorithm. Figure 3.2 shows a Raman spectrum in the region 300-1900 cm^{-1}. Contribution of noise is remarkable, however five bands centered at 395, 480, 630, 800, and 935 cm^{-1} can be readily identified. The FFT of the spectrum is computed using a routine based on one originally developed by Rader-Brenner (Rader and Brenner, 1976) and is plotted in Figure 3.3. The decay-like behavior of the FFT in the large-time region (from 0.65 forth) is typical of Raman signals. On the other hand, a wave-like trend in the FFT, such as that observed in the enlarged area of short-time region (0.2 to 0.65), is characteristic of noise. For the noise to be removed there is a need for a function which passes large time signals but attenuates signals lesser than the cutoff time. Such a function is called a lowpass filter. Lowpass filters are generally defined in the frequency domain (FT domain) of a time-signal. Hereinafter, however, we call lowpass filter a function defined in the time domain of a frequency-signal (the Raman spectrum).

Step-function filters offer good all-around performance, including maximal flatness, with the ideal response of unity in the passband and zero in the stopband, while requiring minimal time and memory consumption. The mathematical form of the filter is as follows:

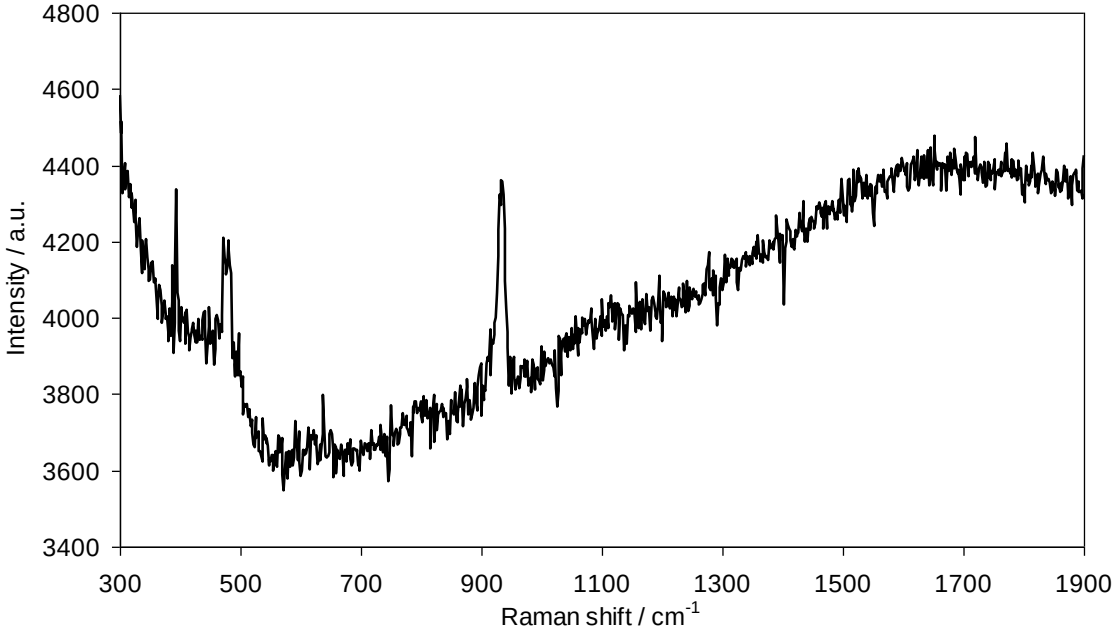

Figure 3.2. Raman spectrum in the region 300-1900 cm^{-1} displaying some bands

.

$$H(t) = \begin{cases} 1, & t \geq t_{co} \\ 0, & t < t_{co} \end{cases} \tag{3.2}$$

where t_{co} is the cutoff time. This filter is currently being considered within the software package for the on-board processing of the data outputs from the Raman-LIBS instrument on-board ESA ExoMars mission (Sobron *et al.*, 2008a).

When using a lowpass filter, some Raman information may be compromised if a significant amount of noise needs to be smoothed away. The cutoff time must therefore be carefully set in order to minimize induced distortions in the spectrum. Figure 3.4 shows the real part of the FFT of the spectrum overlaid to the low-pass filter representation. The transformed spectrum has been normalized-to-one and time-axis has been rescaled to percentage values, ranging 0 to 100. The t_{co} value shown in Figure 3.4 has been derived from a routine that minimizes the following error function:

$$\ln(e) = a + b_{co}^{1/2} \tag{3.3}$$

between two boundaries, $t_{co}^{\ l}$ and $t_{co}^{\ u}$. This empirical function is found to best correlate the cutoff time and the error introduced in the spectrum by the filter. e is defined as

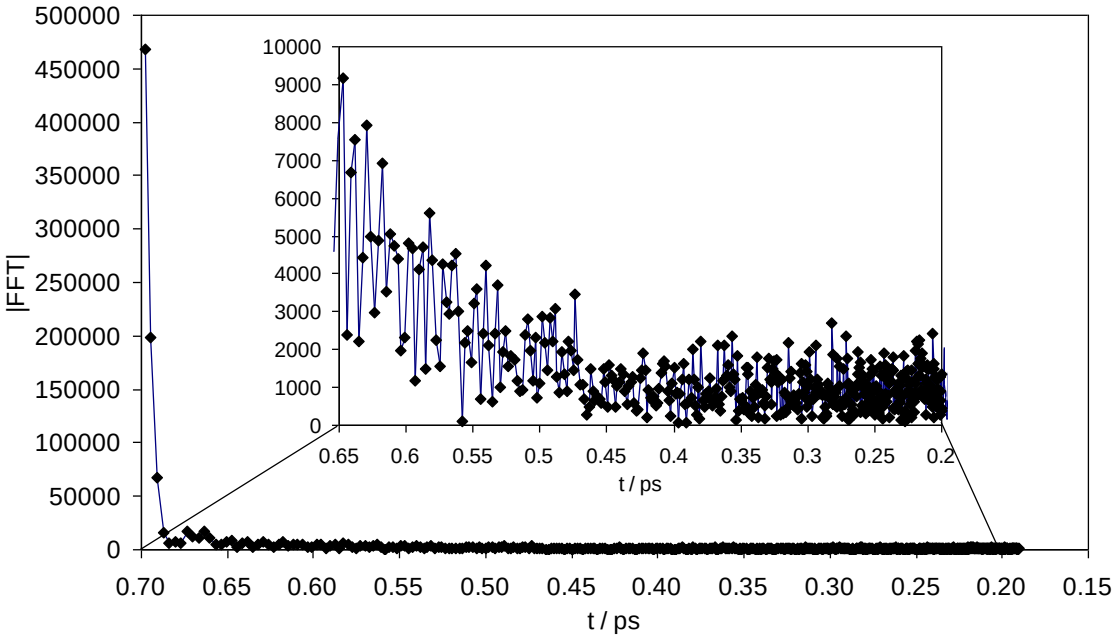

Figure 3.3. Fast Fourier Transform of the Raman spectrum in Figure 3.2

the intensity difference between the maxima of the raw and the filtered spectra, respectively, upon performing its reverse FFT. The parameters *a* and *b* are derived upon computing the error *e* introduced by two filters with t_{co}^{l} and t_{co}^{u} cutoff times, respectively. Typical values for t_{co}^{l} and t_{co}^{u} are 10 and 20, respectively. The threshold for the acceptable error caused by the filter is set to 5%.

The routine for performing the reverse FFT (Rader and Brenner, 1976) is analogous to that for the direct FFT, and yields the filtered Raman spectrum, as shown in Figure 3.5. The original spectrum is overlaid in gray color for comparison purposes. The most intense noise signatures have been attenuated, while the Raman bands are more clearly visible now, as for instance the band centered at 395 cm^{-1}, otherwise highly corrupted by noise.

Since the applications covered by this PhD are not restricted by processing speed-limited computers, other types of filters including the Butterworth (Butterworth, 1930) and modified step-filters (Kauppinen *et al.*, 1981a) were considered for de-noising. These filters show desirable features like smooth response at all times and monotonic decrease from the specified cutoff time. However, we have

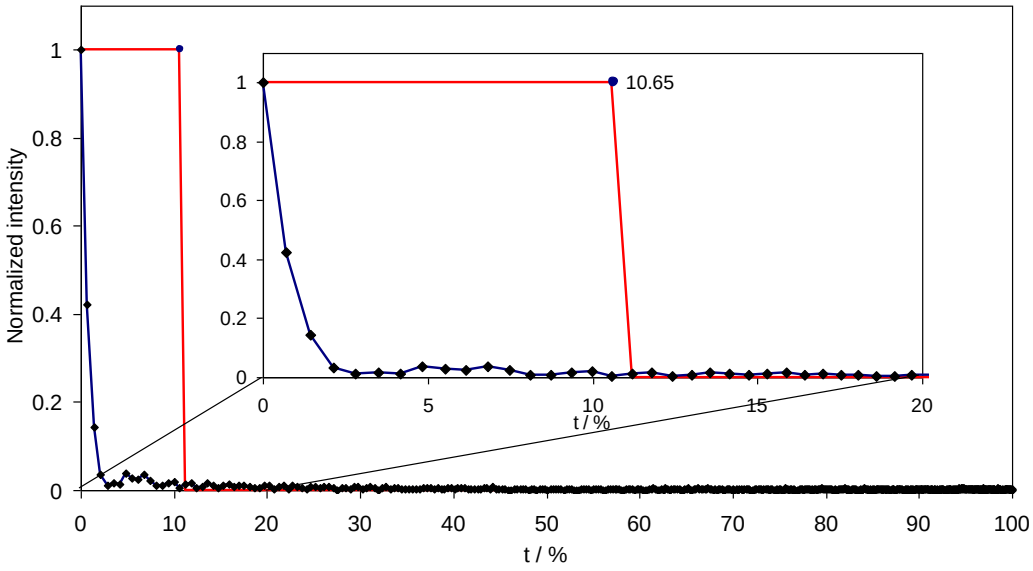

Figure 3.4. Low-pass filter in the time-domain

.

constructed a more flexible filtering function based on neural response functions (Wasserman, 1989):

$$H(n) = \frac{1+e^{-p_2 n_2}}{1+e^{p_2(n-n_2)}} - \frac{1+e^{-p_1 n_1}}{1+e^{p_1(n-n_1)}} \tag{3.4}$$

where n_1 and p_1 are the position of the inflection point and the slope of the left side, respectively, and n_2 and p_2 are the position of the inflection point and the slope of the right side, respectively, as shown in Figure 3.6.

The filter in Eqn (3.4) is typically a bandpass filter, although it can be readily turned into a lowpass filter by setting the parameters to, for instance, $n_1 = 0, p_1 = 99, n = 6,\ p_2 = 10$. Such a filter is plotted in Figure 3.7. The filter in Eqn (3.4) has shown to be the most effective one in our analysis and, unless otherwise indicated, is used for de-noising all the Raman spectra collected for this PhD.

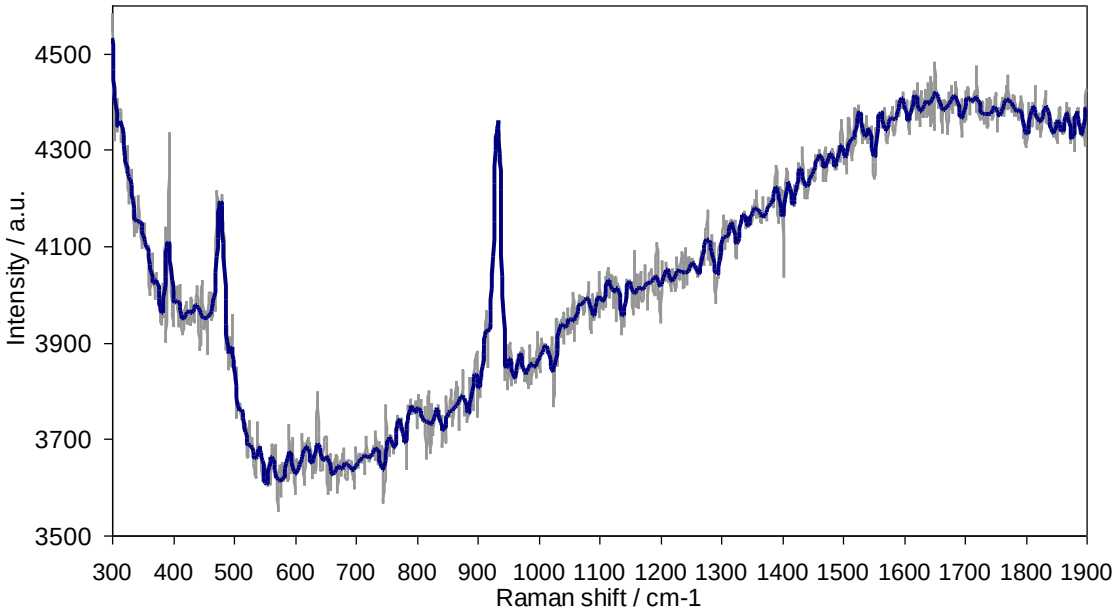

Figure 3.5. Original (gray) and filtered (blue) Raman spectra

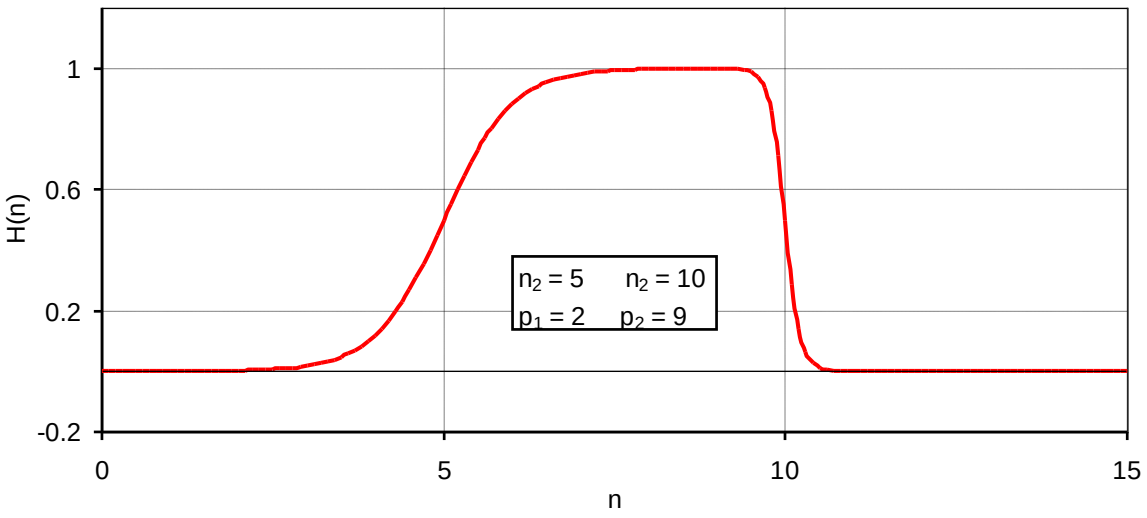

Figure 3.6. Neural response bandpass filter from Eqn (3.4)

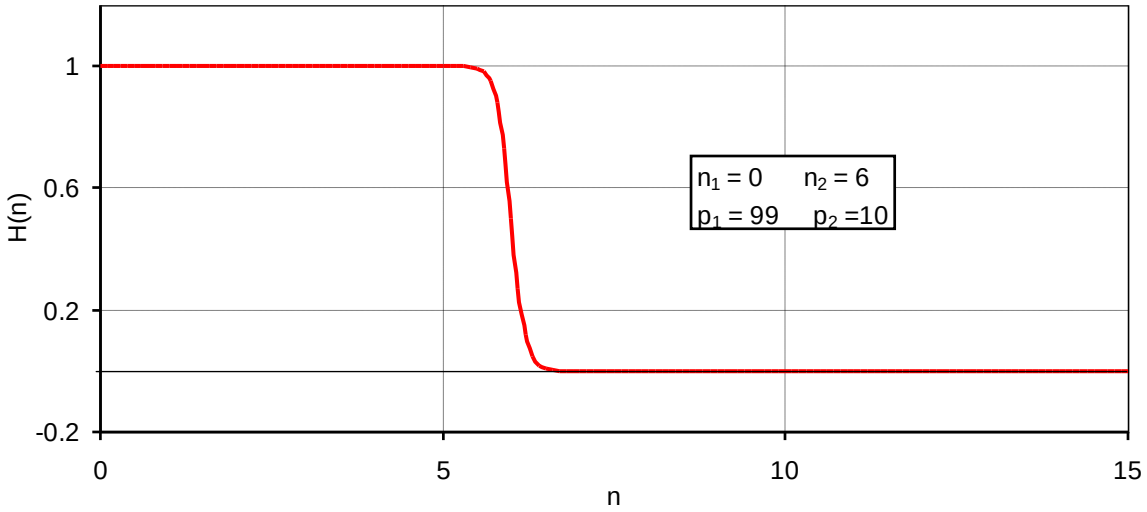

Figure 3.7. Neural response lowpass filter from Eqn (3.4)

3.3. Baseline removal

Sloping and curved baselines are common in Raman spectra, and are mainly due to fluorescence and background signals. Figure 3.8 shows a Raman spectrum displaying a curved background. Weak Raman bands may be obscured by fluorescence and background distortions. Reduction of these interferences is therefore required for further Raman data treatment. As each spectrum shows a characteristic baseline, a removal routine must be applied to every single collected spectrum.

As for the SNR enhancement, a fine characterization of the baseline is critical to avoid loss of information. Generally used baseline removal algorithms include the adapted Pearson's method (Pearson, 1987) and Fourier methods (Atakan *et al.*, 1980; Mossier-Boss and Lieberman, 2000), but again those are computationally taxing routines due their iterative nature. The baseline removal routine included in the software package generates a baseline by linear interpolation from a certain number of spectral points which is then point-by-point subtracted from the spectrum. The points used for the baseline construction are typically some of the local intensity

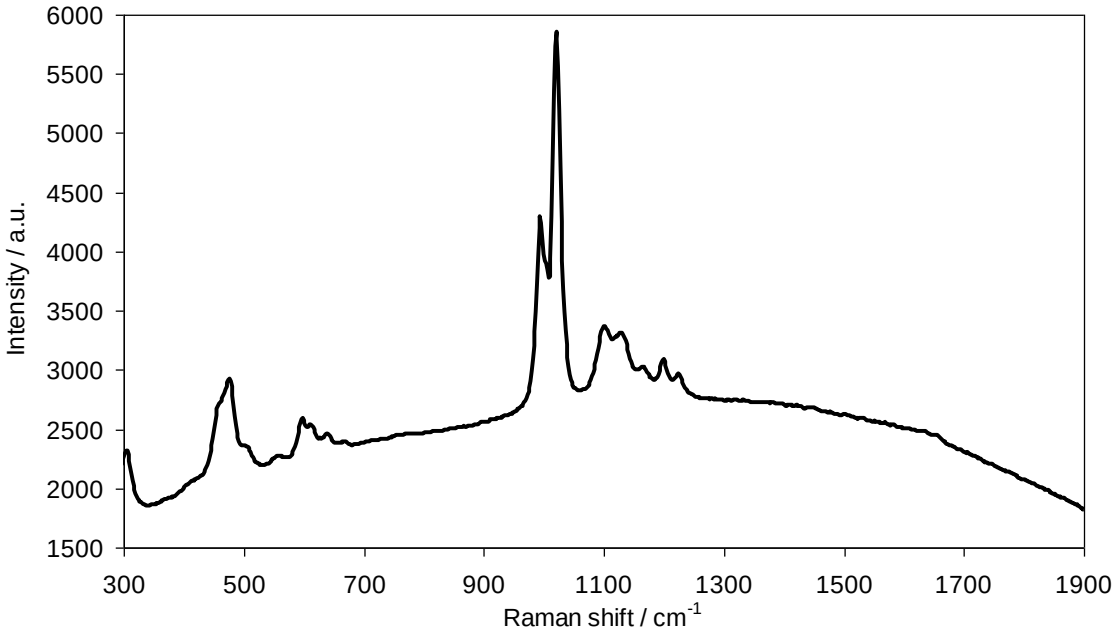

Figure 3.8. Raman spectrum with curved background

minima in the filtered Raman spectrum, and are determined from its first derivative. The general method for obtaining the first derivative spectrum is to compute the intensity difference between adjacent points. However the spectral noise is emphasized since small noise changes between points become amplified by taking derivatives. Again, the FFT proves to be very useful since it provides the derivative while applying a significant noise-reduction, as explained in the previous section. It is well known from Fourier analyses that the Fourier transform of the derivative $f'(w)$ of a function is related to the transform of the function $f(w)$ itself as follows:

$$\mathcal{F}[f'(w)] = jt\mathcal{F}[f(w)] \tag{3.5}$$

where $\mathcal{F}$ represents the FFT and $j = \sqrt{-1}$. The derivative spectrum $f'(w)$ may be obtained by simply taking the reverse FFT in both sides of Eqn (3.5),

$$f'(w) = \mathcal{F}^{-1}\{jt\mathcal{F}[f(w)]H(t)\} \tag{3.6}$$

where $\mathcal{F}^{-1}$ represents the reverse FFT. Note that the filter $H(t)$ (see Eqn (3.4)) has been applied again in order to attenuate the derivation noise.

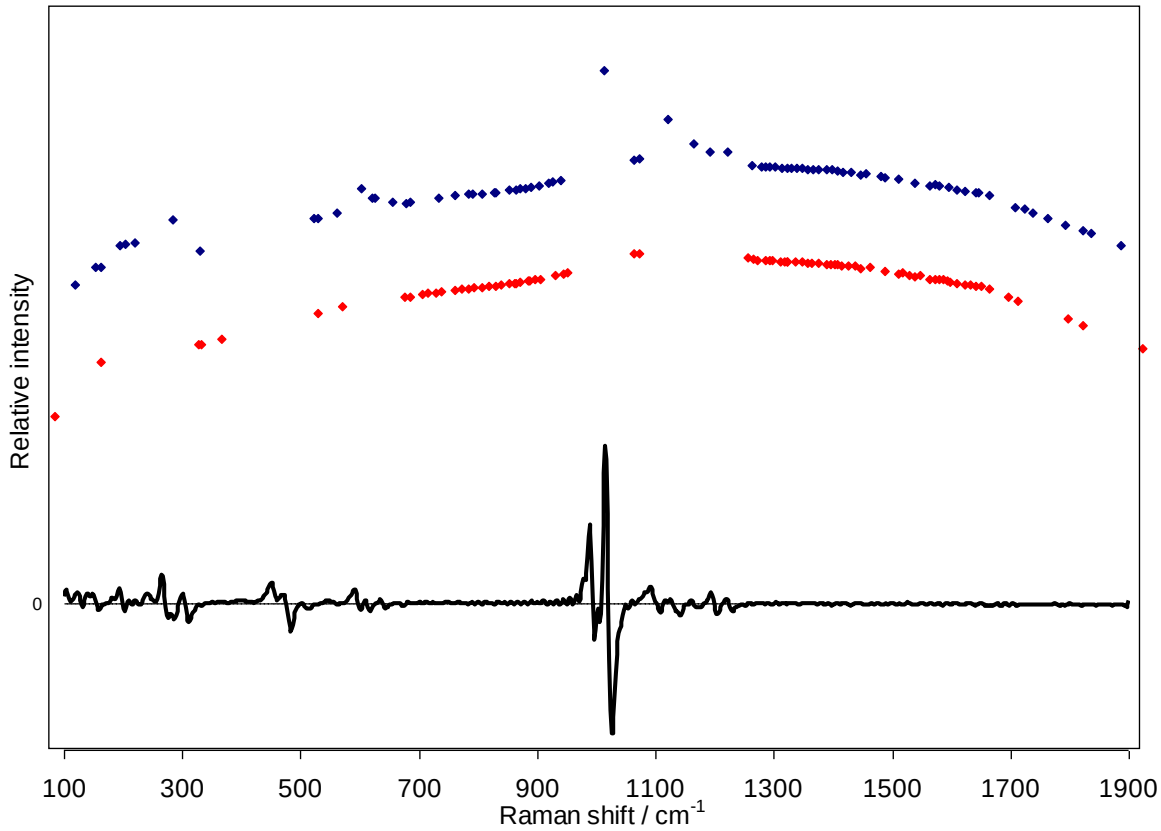

Figure 3.9. Derivative Raman spectrum (black line), local intensity minima (blue), and baseline points (red)

.

A point m is said to be a local minima of function f if $f'(m) = 0$ and the derivative changes from a negative to a positive value across m. Figure 3.9 displays the derivative spectrum (black line) along with all the local intensity minima (blue diamonds). The first set of baseline candidate points is created upon the local minima. However, not all of them are to be classified as baseline points, as for instance those located at 295, 1008 and 1113 cm^{-1}, which arise from the convolution product of Raman bands pairs. Those points are removed from the candidates set with a subroutine based on the moving average. Minima whose absolute value is a 95% greater than the local average (typically the average intensity of a ten-point subset) are no longer considered as baseline points, and hence are removed from the candidates set. The routine is applied iteratively to the set until no more candidates exceed the local average. The remaining points make up the baseline. Figure 3.9 displays the baseline points (red diamonds) of the Raman spectrum. The complete baseline is built

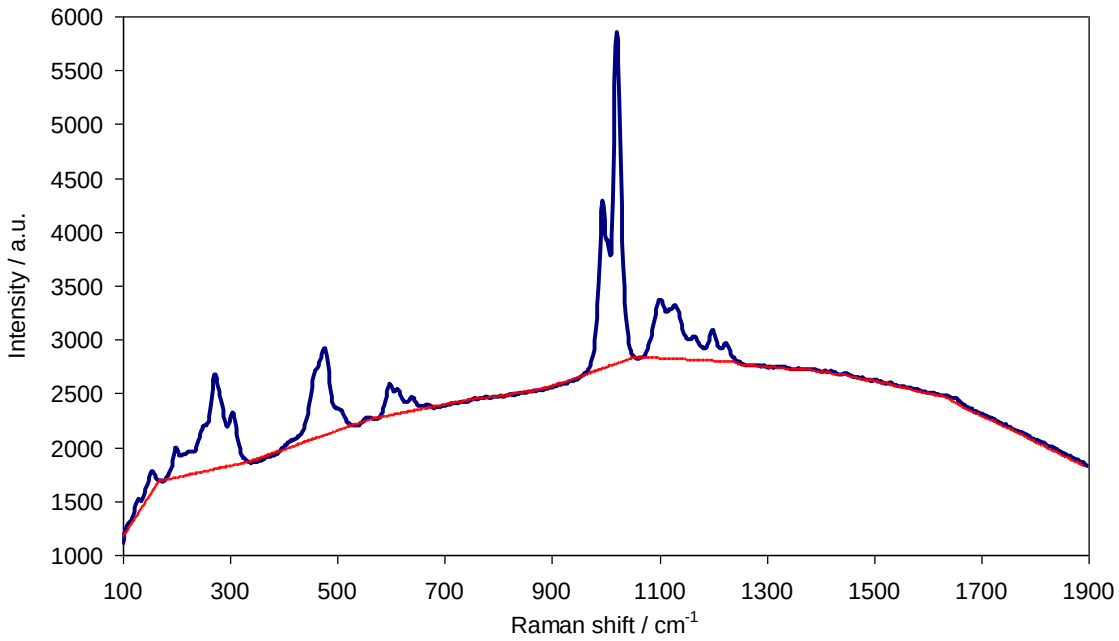

Figure 3.10. Raman spectrum (blue) and baseline (red)

up upon linear interpolation between the baseline points and is plotted in Figure 3.10 (red). The baseline-corrected Raman spectrum is plotted in Figure 3.11.

3.4. Database search-match

A database (DB) containing Raman spectral parameters from most of the minerals known (and expected) to be on the surface of Mars and sulfate analogs on Earth has been implemented, and is being continuously extended as part of the software package in order to allow for a fast automated qualitative analysis of the samples. This is also part of the schedule in the development of the Raman/LIBS spectrometer (RLS) onboard ESA ExoMars mission. The DB search-match process we present here is an early version of the flight-software to be incorporated onboard the ExoMars mission, hence there is room for improvement. Further development will be essential in order to construct more robust and accurate routines to address problems such as the likely poor signal-to-noise ratios of Raman spectra on Mars. Testing flight-like Raman spectrometers in Martian conditions (by means of Mars simulation

chambers) will be crucial in order to understand the instrument spectral response under mission-like scenarios, and will undoubtedly help shaping the software for autonomous mineral phases identification on Mars surface. While the search-match routine here presented is devoted to the RLS, it may fit well other applications that require autonomous mineral identification from Raman spectra.

Three Raman parameters are especially relevant: band position, band intensity and band width. The use of these three parameters within the search-match process is justified since many molecular vibrations give rise to characteristic and unique bands in the Raman spectra, and there is a linear relationship between the band area (computed as a function of the intensity and width of a given band) and the relative concentration of the chemical bonding giving rise to it. However, a Raman spectrum is highly influenced by the nature of the sample (weathering, crystallinity, ...) and environmental and instrumental constrains (laser power, spectral resolution, light collection geometry, …). From our experience, these factors are clearly reflected in the Raman spectra as band-shifts, variations in the relative band-intensity, and as significant band-widths changes. Nevertheless, in our opinion these are the only parameters that may allow for the implementation of a database search-match routine. Ideally, one would desire to build a database upon Raman spectra from Martian samples, collected with the final version of the flight-instrument. In practice, we are focusing all efforts on feeding the database with Raman spectra from selected natural samples collected in field work in extreme environments such as Rio Tinto and El Jaroso in Spain, Spitsbergen in Svalbard, Norway, Iron Mountain in California and Cerro Negro in Nicaragua. Those naturally weathered, often poorly crystalline samples are probably the best approach to the Martian mineralogy we can achieve on Earth. The use of a flight-instrument for recording the Raman database is out of the question, however we are expecting to use a flight-like instrument that integrates optical and electronic components equivalent to that of the flight-instrument in order to study its performance and to evaluate the response noise and eventual artifacts that may affect the Raman spectra. These interferences are to be taken into account for future improvements on the data-base search-match process.

At present, our DB is organized as a structured matrix of records which contains information regarding some seventy compounds (so far) and the intensity, width and position of the band(s) assigned to them. Fields are structured as described in Table 3.1. The search-match routine compares every band in the DB with all the Raman bands of the spectrum under analysis. The latter bands are extracted from the spectrum by finding the local intensity maxima, defined as the points across which the derivative changes from a positive to a negative value. The derivative spectrum is obtained by means of the FFT as described in section 3.3. Intensity maxima are now defined as the points where the derivative changes from a positive to a negative value and whose Raman intensity is not lesser than a predefined threshold (typically 0.05). The half width at half maximum (HWHM) is computed for every band and is stored in a bands-file (BF) along with its position and intensity for the forthcoming search-match process. As mentioned above, the search-match routine compares every band stored in the BF against each of the bands of every compound implemented in the DB. Whether or not the Raman spectrum corresponds to one, or a mixture, of the compounds in the DB is decided on the base of the so-called search-match score (SMS). The SMS is defined as follows for every compound: if a band in the acquired Raman spectrum is found in the DB for the compound *j*, *i.e.*, if the band position (the band-width parameter, although stored in the BF, is discarded as comparison criteria due to the above reasons) in the acquired spectrum equals the band-position of a band for the DB-compound i within a typical tolerance of 3 cm^{-1}, then the SMS_i , with initial value 0 for all the compounds, is increased by (a) 1 if the intensity of the DB band equals 1 (the DB bands for all of the compounds are intensity-normalized, hence the intensity of the most intense band equals 1), and increased by (b) $1/\mathrm{n}$ otherwise, where n is the number of bands of the compound i. For instance, if a band in the Raman spectrum matches the most intense band assigned to the compound k, and matches 3 more bands assigned to the same compound, then the SMS for that compound will be $\mathrm{SMS}_k = 1 + \frac{3+1}{8} = 1.5$, assuming that the total number of bands assigned to that mineral is 8. Let the same Raman spectrum show 5 bands arising from another compound l, none of which is the principal band (that of relative intensity 1).

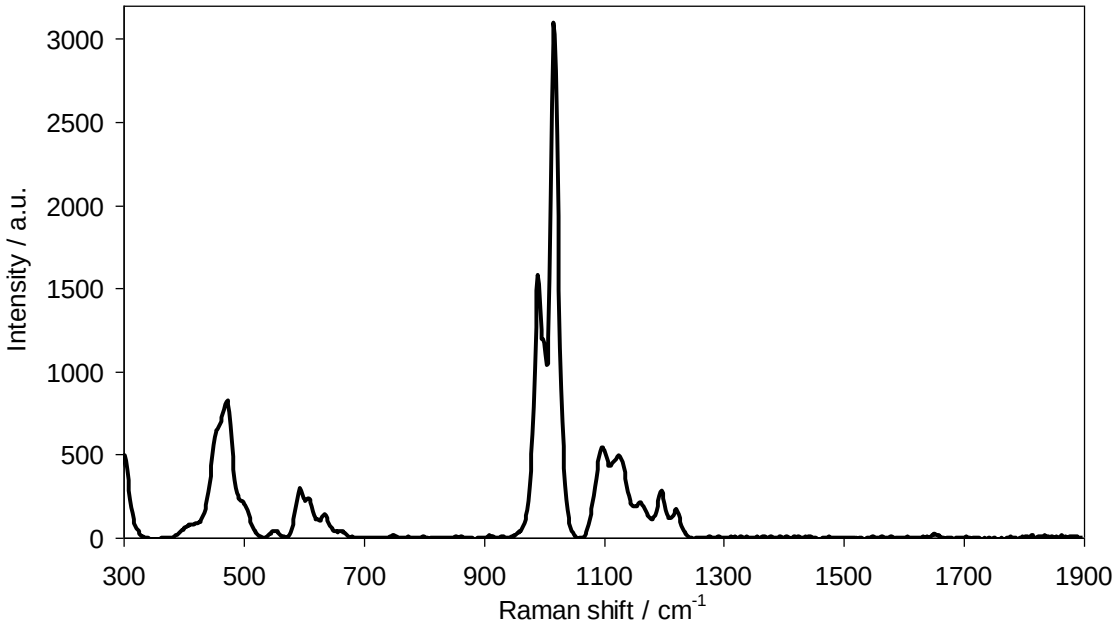

Figure 3.11. Baseline corrected Raman spectrum

.

The score for this compound will therefore be $\mathrm{SMS}_l = \frac{5}{15} = 0.33$ provided the compound *l* is assigned a total of 15 bands in the DB.

A compound is said to be present in the analyzed sample if its SMS is equal or greater than 1. If a SMS equals 1, a poor identification has been achieved since only the principal band related to that compound has been found in the Raman spectrum. It is therefore likely that this band arises from a different compound, but has been shifted from its true position probably due to crystalline/orientation defaults or low-resolution spectrum. On the other hand, a SMS value equal to 2 means an unambiguous identification since all the DB bands of a given compound are found in the Raman spectrum.

The *in-situ* analysis of Martian sulfates in the search for signs of past and/or present life on Mars will probably be one of the main objectives of the ExoMars rover. The Raman instrument will play an important role in this task. Therefore, the final version of the autonomous mineral identification software must include information on the Raman spectra of most of the sulfates and biomarkers know to occur on Earth and expected to be found on Mars. Sulfates have been extensively studied by means of

Raman spectroscopy. Especially relevant are the results of Chio *et al.* (2005), who show a systematic peak-position shift toward lower wavenumbers in the fundamental sulfate stretching vibration modes when the hydration state increases. Additionally, Raman peak shifts are also observed for the same vibration mode, and may be correlated to nature of the substitution cation in jarosites (Sasaki *et al.*, 1998), one of the key compounds associated with the likely existence of a former Martian acidic aqueous environment.

Both Raman studies were conducted on synthetic sulfates, and the reported Raman shifts are often lesser than a few wavenumbers. The Raman analysis on natural samples is notably more complex, since those can include different sulfate compounds and/or low concentrations of other ions within the same sampled spot, thus making difficult the minerals phases identification (Frost *et al.*, 2006a; Sobron *et al.* 2008b). To address this inconvenience, the Raman database must contain information on all of the known sulfates, including cation-substitution and hydration states. This sounds reasonable, though probably exceedingly time/power-taxable in the context of a rover autonomous operation mode. Most likely we will make use of the very strong synergy between the Raman and LIBS techniques (Wiens at al., 2005; Sharma *et al.*, 2007) which led the combined Raman/LIBS instrument (Courreges-Lacoste *et al.*, 2007) to be considered a fundamental tool for the analysis of the Martian surface.

Table 3.1. Structure of the Minerals Database

Min ID	Min name	Min formula	Min Location[a]	Spectrom. info[b]	Laser info[c]	Bands nr.[d]	Band1 center[e]	Band1 intensity[f]	Band1 HWHM[g]	…[h]

[a] Sampling site where mineral was collected

[b] Spectrometer make

[c] Laser wavelength and power

[d] Number of characteristic bands for the mineral

[e] Position of band maximum

[f] Normalized band intensity

[g] Half width at half maximum

[h] Band position/intensity/HWHM for each band. (Up to the number of bands)

3.5. Band Fourier self-deconvolution and band-fitting

As explained in section 3.1, Raman spectra are invariably affected by the measuring system, measuring geometry, etc. Particularly, instrumental band-broadening is common in Raman measurements involving dispersive spectrometers, as those used in this PhD. This broadening of the Raman bands may be reduced to the point that completely overlapped bands can be resolved. The Fourier self-deconvolution technique has been described by Kauppinen *et al.* (1981b), Friesen and Michaelian (1988) and Griffiths and Pariente (1986), among others. The process is called Fourier deconvolution since it involves the use of the Fourier Transform (FT).

Strictly speaking, deconvolution is the reverse operation of the convolution (the responsible of spectral distortion in the physical domain). Accordingly, any experimental Raman spectrum may be modeled as the convolution of a pure vibrational spectrum $S_0(\nu)$ with a broadening function $B(\nu)$ (Rull *et al.*, 1993):

$$S(\nu) = \int B(\nu - \nu')S_0(\nu')d\nu' = B(\nu) * S_0(\nu) = S_0(\nu) * B(\nu) \quad (3.7)$$

$S_0(\nu)$ may be derived once the functions are Fourier Transformed. The deconvolution yields:

$$S_0'(\nu) = \mathcal{F}^{-1}\{\mathcal{F}[S(\nu)]/\mathcal{F}[B(\nu)]\} \quad (3.8)$$

where $\mathcal{F}$ and $\mathcal{F}^{-1}$ denote the direct and the inverse FT, respectively. Note that, as an exact solution for the pure spectrum involves calculation of FT, a numerical (therefore approximate) solution is obtained, hence the notation $S_0'(\nu)$. Friesen and Michaelian (1985) showed that the broadening function in dispersive spectrometers is approximately Gaussian. Such a profile accounts for natural line broadening, thermal broadening and optical broadening that may affect the Raman lines' width. An additional advantage of Gaussian profiles is that they do not introduce noise. Consequently, in this PhD the line-shape of the broadening function is considered as Gaussian:

$$B(\nu) = e^{-\nu^2/2\sigma^2} \quad (3.9)$$

where σ is a real constant related with the width of the function. The FT of a Gaussian function is another Gaussian function:

$$\mathcal{F}[B(\nu)] = \tilde{B}(t) = \sigma\sqrt{2\pi}e^{-\sigma^2 t^2/2} \tag{3.10}$$

The FT of the recorded spectrum $\mathcal{F}[S(\nu)]$ is computed as shown in section 3.2. Combining Eqns (3.8), (3.9), and (3.10) yields:

$$S_0'(\nu) = \mathcal{F}^{-1}\{\tilde{S}(t)/\tilde{B}(t)\} = \mathcal{F}^{-1}\{H(t)\cdot\tilde{S}(t)\cdot Ae^{\sigma^2 t^2/2}\} \tag{3.11}$$

Note that an apodization function (Eqn (3.4)) is used in order to avoid the amplification of noise introduced by the exponentially increasing function in Eqn (3.11). This effect has been nicely illustrated by Friesen and Michaelian (1988). The reverse FT in Eqn (3.11) is computed as described in section 3.2. Figure 3.12 shows the Fourier deconvolution (red) of a Raman spectrum (blue). The narrowing of the Raman bands in the deconvoluted spectrum is clearly illustrated in this figure.

The degree to which component bands can be distinguished has been noticeably improved. One could make use of the band parameters (position, intensity, width, Gauss-Lorentz factor) for quantitative measurements on a deconvoluted Raman spectrum. However, those parameters could be not accurate enough since the broadening function $B(\nu)$ is just an approximation to the real, unknown function shapes of the physical processes that cause spectral broadening. The deconvoluted Raman spectra were used in this PhD thesis mainly for retrieving the number of fundamental bands that make up the original spectra along with their positions. A so-called convoluted spectrum is constructed upon the self-resolved bands. Bands' intensity, width and G-L factor are then iteratively adjusted until the best fit between the convoluted and original spectra is achieved. The best-fit parameters are achieved through minimizing a non-linear merit function χ^2 by means of the Marquardt method (Marquardt, 1963; Press *et al.* 1992). This method is probably the most common of the non-linear least-squares routines. The band parameters in the self-resolved Raman spectrum of Figure 3.12 have been adjusted using the Marquardt routines and the result is plotted in Figure 3.13.

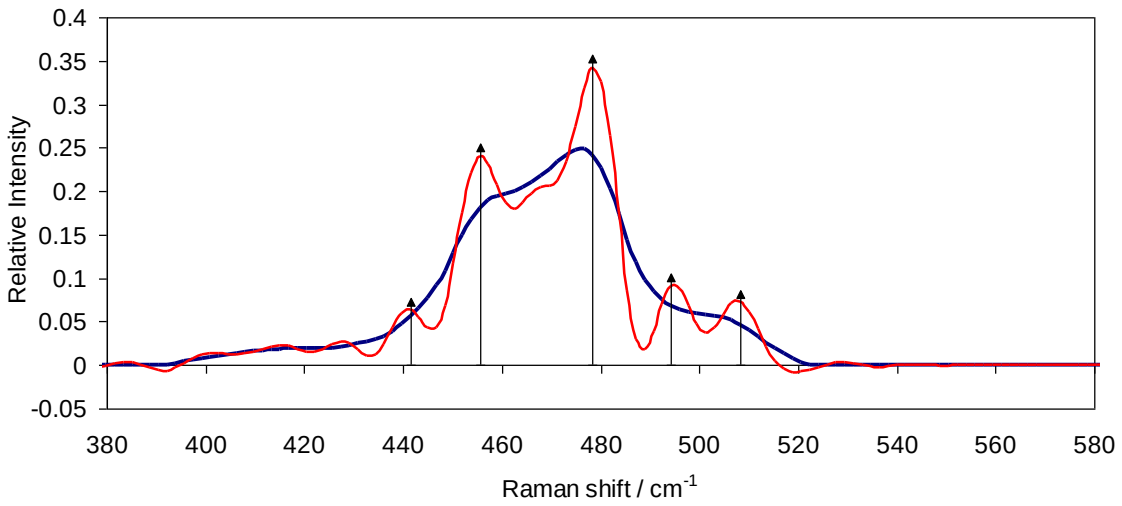

Figure 3.12. Fourier self-deconvolution (red) of Raman spectrum (blue) of a jarosite in the low wavenumbers region. Self-deconvolution shows five bands centered with improved spectral resolution

3.6. Summary

The Raman spectra collected along the present pre-doctoral work were post-processed in order to retrieve the maximum Raman information. The spectra went through a set of routines in order to remove the noise and baseline. When quantitative information was required, Fourier self-deconvolution and band-fitting routines were applied. Although the routines for processing of the Raman spectra may be automated, and actually were automated for certain applications (Sobron *et al.*, 2008a), user interaction is often required for refined data treatment. In order to integrate all the post-processing routines described in the previous section, we developed an application based on the macro programming language named VBA (Visual Basic for Applications) for Microsoft Office Excel (Clinick, 2001). This VBA programming capabilities within Excel provides as very friendly user interface which allows using input taken from the spreadsheet proper in order to set the control parameters for the routines described in sections 3.2 to 3.5. The spreadsheet thus becomes an interface to the code, enabling easy interaction with the code and what it calculates. By way of an example, Figure 3.14 displays two screenshots of the Excel-based software.

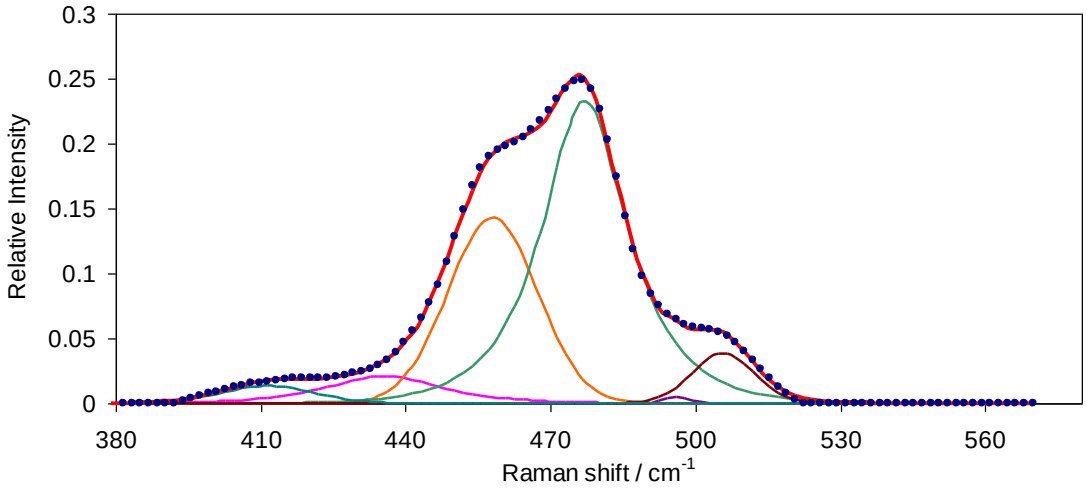

Figure 3.13. Band-fitting (colored solid lines) of the Raman spectrum (blue dots) shown in Figure 3.12. The convoluted spectrum (red line) fits the original spectrum with $\chi^2 = 0.028$

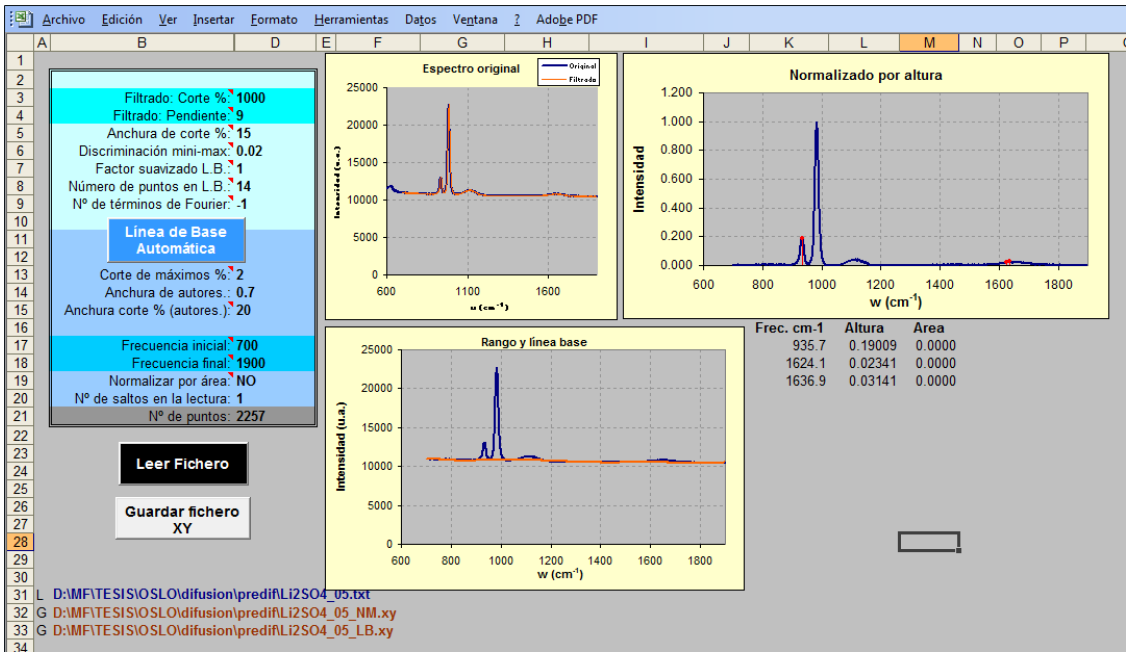

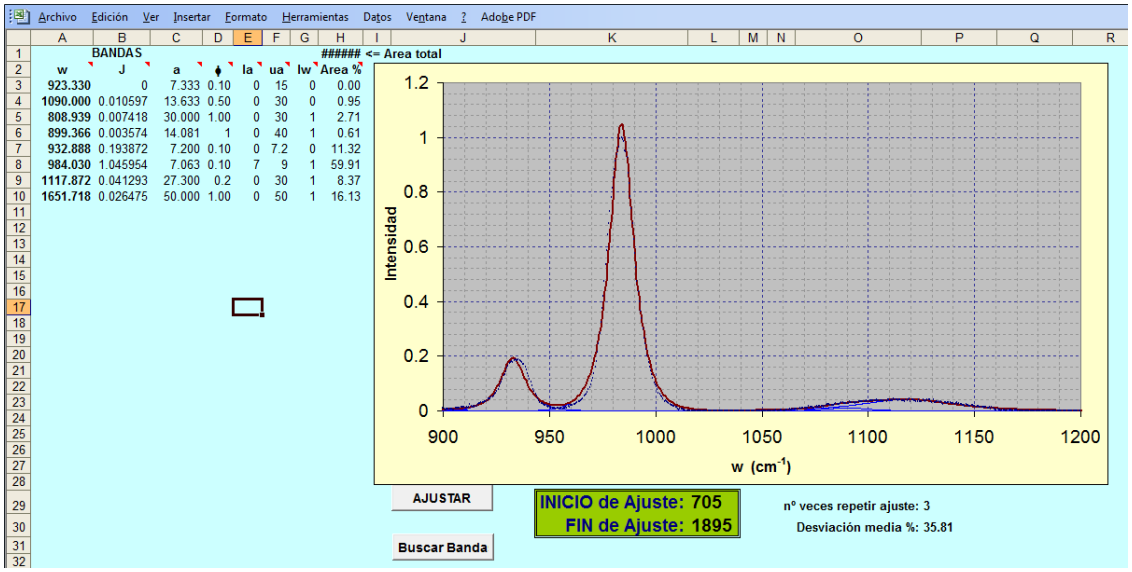

Figure 3.14. Upper: screenshot of the spreadsheet showing the original and filtered spectrum ("Espectro Original"), spectrum plus baseline ("Rango y linea base") and a baseline-corrected and normalized spectrum ("Normalizado por area"). Automatic filtering and baseline correction routines use the input given in range (B2:D21). Lower: screenshot of the spreadsheet showing a band-fitted spectrum, with band calculated parameters in range (A2:H10).

Chapter 4

acidic sulfate waters and solutions

This chapter describes the investigations on acidic aqueous systems carried out in this thesis. Natural and synthetic samples were studied. The physico-chemistry of two synthetic systems of special relevance in the acid mine drainage context, such as iron(II) sulfate-sulfuric acid-water, and iron(III)-sulfuric acid-water, was investigated. The mass transport properties of a third system, sulfuric acid-water, were studied. The Raman spectroscopy of selected stream waters from Rio Tinto was also studied.

4.1. Overview

In the following sections we report:

i. The characterization of the chemical equilibriums of the iron(II) sulfate-sulfuric acid-water synthetic system as a mimic to Rio Tinto stream water. This simplified system represents a sound first approach to river's real hydrogeochemistry as it involves two of the major species present in Rio Tinto stream water: iron(II) and sulfate. The characterization of the mentioned system is based on the identification of the main chemical species and the determination of their concentrations in their basic equilibrium states. Accuracy is needed in order to determine the nature of the ionic species in the iron(II) sulfate-sulfuric acid-water system. Raman spectroscopy is an ideal tool in studies of aqueous solutions since many molecular vibrations give rise to characteristic and unique bands in the Raman spectra. Raman spectroscopy also allows real-time identification of species and a very rapid quantification of their abundance. As Raman spectroscopy is a non-invasive and non-destructive technique, the equilibriums in the system are not affected by the measurements.

ii. The speciation of iron(III) in the system iron(III)-sulfuric acid-water by means of Raman spectroscopy. The complex interaction processes between extremophile bacteria and the river's substrate accelerate the oxidation of iron(II) into iron(III) (González-Toril *et al.*, 2003). The system iron(III)-sulfuric acid-water represents also a good approach to Rio Tinto hydrogeochemistry since iron(III) and sulfate ion are two of the major components of Rio Tinto extremely acidic water (López-Archilla *et al.*, 1993). The Raman technique provides the accuracy and repeatability critical for qualitative and quantitative analysis. Particularly, molecular vibrations of iron(III) complexes are determined by specific wavelengths in the Raman spectra. Intensity and width changes of the Raman bands corresponding to iron(III) complexes molecular vibrations can be quantified very rapidly. Solutions require no preparation prior to Raman spectra collection, which is of great importance for potential field analysis of AMD.

iii. The diffusion of dissolved chemical species in the system sulfuric acid-water. A diffusion model is proposed and validated against experimental measurements of the concentration of bisulfate and sulfate ions carried out by Raman spectroscopy. The optimization of the diffusion model yields diffusion coefficients which are linear functions of the concentrations while the thermodynamic equilibrium among species is a complex function of the concentration of sulfate ion.

iv. The Raman spectroscopy of natural selected aqueous solutions from Rio Tinto. As a noninvasive and nondestructive technique, the Raman technique allows for the aqueous samples to be readily analyzed without any preparation. Mine tailings such as the site under study contain large amounts of sulfur-rich mineral and are characterized by highly acidic waters. The relative abundance of sulfate and bisulfate ions and water, predominant species in acid mine groundwaters, has been derived from the Raman spectra of aqueous samples from Rio Tinto waters.

4.2. Thermodynamic equilibriums in the system iron(II) sulfate-sulfuric acid-water

4.2.1. Abstract

Acid mine waters containing extremely high concentrations of sulfuric acid and dissolved iron are found in the Rio Tinto area. In this study, Raman spectroscopy has been used to investigate the speciation of the system iron(II) sulfate-sulfuric acid-water as an approach to Rio Tinto's stream water. Several solutions of aqueous sulfuric acid containing iron(II) sulfate in the range 0-1.65 mol/kg were prepared and qualitative and quantitative analyses of the ions present in the solutions were carried

out using Raman spectroscopy. The intrinsic features of Raman spectroscopy allow the identification of species present in solution and to calculate species concentration through band fitting of the Raman spectra. The activity coefficients product of the system iron(II) sulfate-sulfuric acid-water as a function of salt concentration is reported. Previous findings on the formation of iron(II) hexahydrate complexes in the mentioned system have been corroborated by means of Raman spectroscopy.

4.2.2. Experimental

4.2.2.1. Sample preparation

A set of ten solutions containing iron(II) sulfate, sulfuric acid and water were prepared from solid heptahydrated iron(II) sulfate ($FeSO_4 \cdot 7H_2O$, Panreac), concentrated sulfuric acid of p.a. quality (95-97% in H_2O, Scharlau) and distilled water by using standard quantitative techniques. Distilled water was acidified with 0.086 mol/kg sulfuric acid. The composition of the solution was determined by tritation. $FeSO_4$ was added to the aqueous sulfuric acid solutions in concentrations ranging 0 to 1.65 mol/kg. (The solution containing 1.65 mol/kg of $FeSO_4$ was near-saturated). Table 4.1 shows the concentration of iron(II) sulfate in the studied samples. Lithium perchlorate was used as internal reference in the quantitative analysis of the Raman spectra of the samples; 0.26 mol $LiClO_4$ per kg solvent was added to each sample in order to provide the internal reference. All samples were kept at a constant temperature of 20 °C during preparation and analysis.

4.2.2.2. Raman experiments

Raman spectra of the solutions were collected at a constant temperature of 20 °C with a Horiba JOBIN-YVON T64000 spectrometer (*cf*. 2.3) within the spectral range 250-3900 cm^{-1}. The achieved spectral resolution was 4 cm^{-1}. The 532.4 nm line of a Spectra-Physics Millenia Pro (Nd:YVO_4 crystal diode-pumped) laser was used as excitation source.

Table 4.1. Concentration of iron(II) sulfate in the samples and results derived from the band-fitting

ID	*m*(FeSO4)	*A*(982)[a]	*A*(1037/1052)[a]	*m*(SO_4^{2-})[b]	*m*(HSO_4^-)[b]	*m*(H^+)[c]	a[d]	K_m[e]	K_g[f]
H00	0.00	0.09	0.12	0.04	0.05	0.12	0.45	0.1008	0.1191
H01	0.23	0.61	0.17	0.25	0.07	0.10	0.79	0.3940	0.0305
H02	0.44	1.12	0.18	0.46	0.07	0.10	0.87	0.6885	0.0174
H03	0.64	1.60	0.19	0.65	0.07	0.10	0.90	0.8848	0.0136
H04	0.83	2.05	0.21	0.83	0.08	0.09	0.91	0.9240	0.0130
H05	1.01	2.53	0.17	1.03	0.06	0.11	0.94	1.7109	0.0070
H06	1.19	2.98	0.16	1.21	0.06	0.11	0.95	2.0542	0.0058
H07	1.35	3.37	0.16	1.37	0.06	0.11	0.96	2.3503	0.0051
H08	1.51	3.76	0.17	1.53	0.06	0.11	0.96	2.5787	0.0047
H09	1.65	4.11	0.16	1.67	0.06	0.11	0.96	2.8608	0.0042

[a] Band area relative to the area of 935 cm^{-1} perchlorate band
[b] Species concentration derived from Eqn (4.1)
[c] Hydrogen concentration derived from Eqn (4.5)
[d] Second degree of dissociation derived from Eqn (4.4)
[e] Concentration product derived from Eqn (4.6)
[f] Activity coefficients product derived from Eqn (4.7)

4.2.3. Results and discussion

Processing of the original Raman spectra was performed with software described in chapter 3. The spectra were first filtered, smoothed and baseline corrected using improved FFT algorithms in order to remove both the sample fluorescence and the noise. These operations are required to perform further spectral analysis like band fitting. The mean standard deviation for all of the band-fittings in this study was below 6%. The optimization yields the so-called best-fit parameters which provide the quantitative information of the Raman spectra. Figure 4.1 shows the band fitted spectrum of solution H04 (for chemical composition, see Table 4.1) in the region 850-1200 cm^{-1}. Band assignment is as described in section 2.2.

One of the basic assumptions in the analysis of Raman spectra is the existence of a linear relationship between the intensity of the peaks and the concentration of the

chemical components in the sample. In a Raman experiment, the scattered light from a volume of the sample is collected. For a single exposure, the collected intensity depends, among others, on the stimulating power and the scattering volume of the sample. These variables are difficult to reproduce from one experiment to the next and for that reason there is a need for an internal reference in order to quantify the scattered intensity. A low concentration of $LiClO_4$ (0.26 mol/kg) was added to each solution for that purpose. The molal scattering coefficient of the v_1 sulfate band relative to that of the v_1 perchlorate band, k_s is measured as 0.641 ± 0.013 on the basis of six independent measurements. The band area of the double band of the bisulfate at 1037/1052 cm^{-1} relative to the v_1 perchlorate band is used to obtain the molal scattering coefficient of the bisulfate, k_b measured as 0.666 ± 0.010. The derived values of k_s and k_b are in good agreement with those reported by Dawson *et al.* (1986) (0.637 and 0.655, respectively) and Myhre *et al.* (2003) (0.639 and 0.676, respectively). With k_s and k_b available the molalities of sulfate, $m(SO_4^{2-})$ and bisulfate, $m(HSO_4^-)$ can be obtained from the relative band area of the 982 and 1037/1052 cm^{-1} bands, A(982) and A(1037/1052) respectively, from the equations:

$$k_s = \frac{A(982)/A(935)}{m(SO_4^{2-})/m(ClO_4^-)} \quad ; \quad k_b = \frac{A(1037/1052)/A(935)}{m(HSO_4^-)/m(ClO_4^-)} \tag{4.1}$$

Sulfate and bisulfate ions result from the dissociation of sulfuric acid, which occurs in two steps:

$$H_2SO_4 + H_2O \leftrightarrow HSO_4^- + H_3O^+ \tag{4.2}$$

$$HSO_4^- + H_2O \leftrightarrow SO_4^{2-} + H_3O^+ \tag{4.3}$$

The degrees of dissociation are denoted by α_1 and α_2 for the equilibriums in Eqns (4.1) and (4.2), respectively. The first degree of dissociation is known to be very close to 1 in almost all relevant concentration ranges (Young *et al.*, 1959). The second degree of dissociation can be expressed in terms of the ion concentrations as:

$$\alpha_2 = \frac{m(SO_4^{2-})}{m(SO_4^{2-}) + m(HSO_4^-)} \tag{4.4}$$

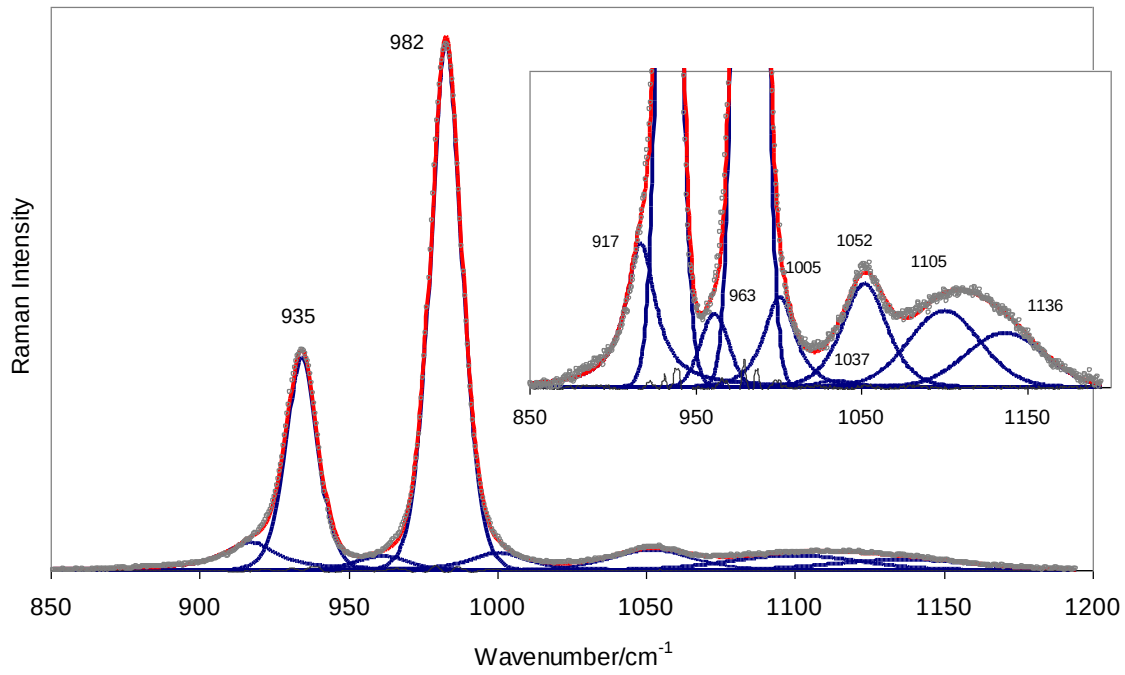

Figure 4.1. Band fitted spectrum in the region 850-1200 cm^{-1} of the sample H04. Grey circles represent the original Raman spectrum, blue lines the fitted bands, red line the convolution spectra and black line the residual. Fitted region is enlarged into the upper right corner for better inspection of band decomposition

where *m*(*i*) denotes molality of species *i*. Myhre *et al.* (2003) compared experimental results with model predictions of the degree of dissociation α_2 in different aqueous sulfuric acid solutions as a function of acid concentration. They reviewed as well some of the numerous works reporting data of the second degree of dissociation α_2 determined by Raman spectroscopy. Knopf *et al.* (2005) present the latest summary on Raman spectroscopic and model prediction data on the dissociation of bisulfate.

Raman spectra of the iron(II) sulfate-sulfuric acid-water solutions in the region 850-1200 cm^{-1} are plotted in Figure 4.2. For each solution, ten Raman spectra were collected; no significant differences were observed within each set. The spectra are normalized to the intensity of the v_1 perchlorate band at 935 cm^{-1} for comparison purpose. It can be seen that the intensity of the sulfate band at 982 cm^{-1} rises as salt concentration is increased. The concentrations of the sulfate and bisulfate ions in each solution are, as previously described, derived from the relative area of the bands at 982 and 1037/1052 cm^{-1} and their values are collected in Table 4.1. Whereas the

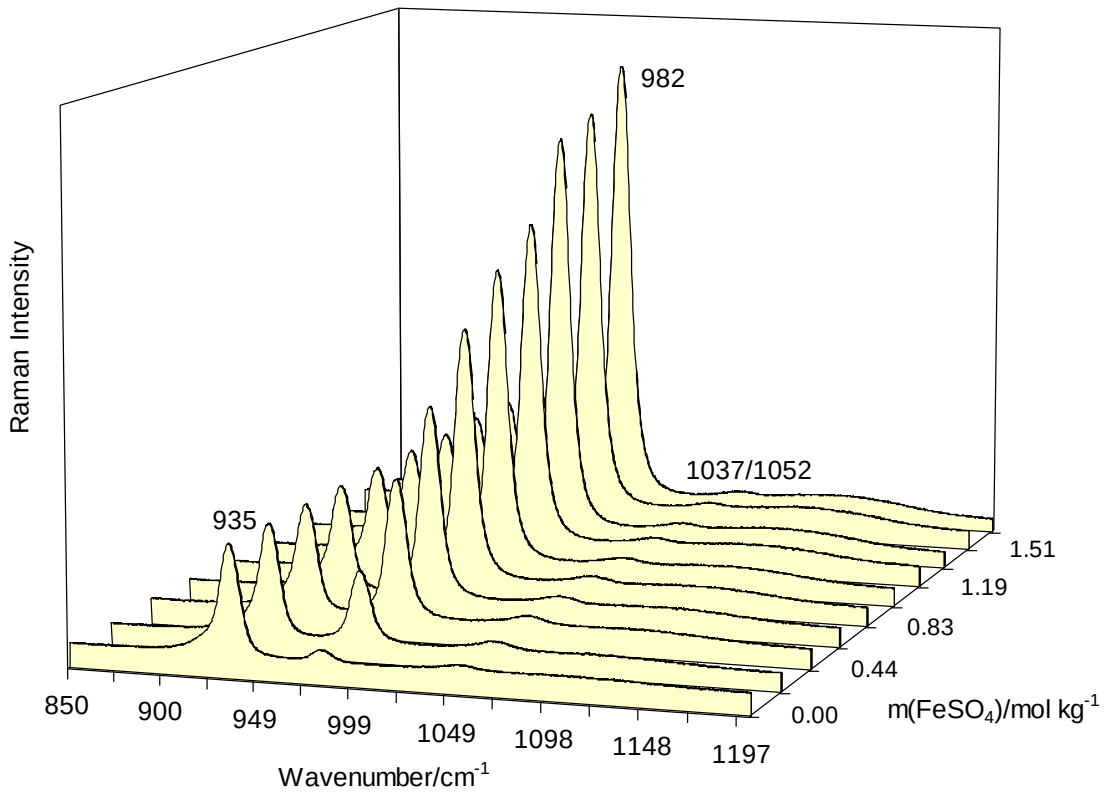

Figure 4.2. Raman spectra of the solutions H00 to H09 in the region 850-1200 cm^{-1}. The spectra are normalized to the intensity of the perchlorate band at 935 cm^{-1}

sulfate ion concentration increases monotonously as a function of the salt concentration, the bisulfate ion concentration never exceeds 0.08 mol/kg. The bisulfate band at 1037/1052 cm^{-1} is weak and the S/N ratio is relatively poor, so the band area is sensitive to variations in the band-fitting parameters. On the other hand, the 1105 cm^{-1} sulfate band and the 1037/1050 cm^{-1} bisulfate double band overlap (Figure 4.1). This overlap is considerable and not easily resolvable owing to the low intensity and proximity of the bands. The estimation of accurate band parameters for each component is therefore rather difficult and the values of the bisulfate concentration reported in Table 4.1 must be regarded cautiously.

The derived values of α_2 from Eqn (4.4) are included in Table 4.1. The sulfate concentration is much higher than bisulfate concentration in the samples H01 to H09, and it is clear from Eqn (4.4) that the second degree of dissociation approaches 1. The bands corresponding to both sulfate and bisulfate ions in the Raman spectrum of the

sample H00 are very weak in the region 850-1200 cm^{-1}; thus there is a considerable uncertainty not only in the derived bisulfate concentration, as was previously discussed, but in the accuracy of sulfate concentration. This affects to a large extent the derivation of the value of α_2 in this sample. This may be the reason why there are no references in the literature to the determination of α_2 in such diluted aqueous solutions of sulfuric acid from Raman spectroscopic measurements. Model-predicted values of the second degree of dissociation for very diluted aqueous solutions of sulfuric acid were reported by Knopf *et al.* (2003). They report α_2 = 0.3 for a sulfuric acid concentration similar to the sample H00 at 290 K.

Iron(II) forms a very stable hexahydrate complex $[Fe(H_2O)_6]^{2+}$ with pK_a = 9.5 (Baes and Mesner, 1986), and will therefore not contribute to the acidity of the solution. The concentration of hydrogen ions can therefore be calculated from the expression:

$$m(H^+) = 2 \times m(H_2SO_4) - m(HSO_4^-) \quad (4.5)$$

The values of the proton concentration in each sample are shown in Table 4.1.

Raman spectra of the samples were also analyzed in the region 325-750 cm^{-1} and are plotted in Figure 4.3. The spectra have been normalized to the 935 cm^{-1} perchlorate band. Four bands, centered at 375, 450, 608, and 625 cm^{-1}, were used to decompose the Raman spectra in the low-wavenumbers region. Figure 4.4 shows the result from fitting the spectrum of solution H09 in the region 325-750 cm^{-1}. The band at 375 cm^{-1} is attributed to a vibration of the $[Fe(H_2O)_6]^{2+}$ complex (Majzlan and Myneni, 2005), and the band at 450 cm^{-1} and the doublet at 608/625 cm^{-1} originate from the v_2 and v_4 degenerate vibration modes of SO_4^{2-}, respectively (*cf*. 2.2). From an inspection of Figure 4.3 it is clear that the four bands increase with the $FeSO_4$ concentration. Majzlan and Myneni (2005) concluded from their IR studies of aqueous iron(II) sulfate that once $FeSO_4$ dissolves, sulfate and iron(II) either reassociate in outer-sphere complexes or do not associate at all. An inclusion of oxygens from sulfate ions into the $[Fe(H_2O)_6]^{2+}$ octahedra would lead to a charge delocalization and a

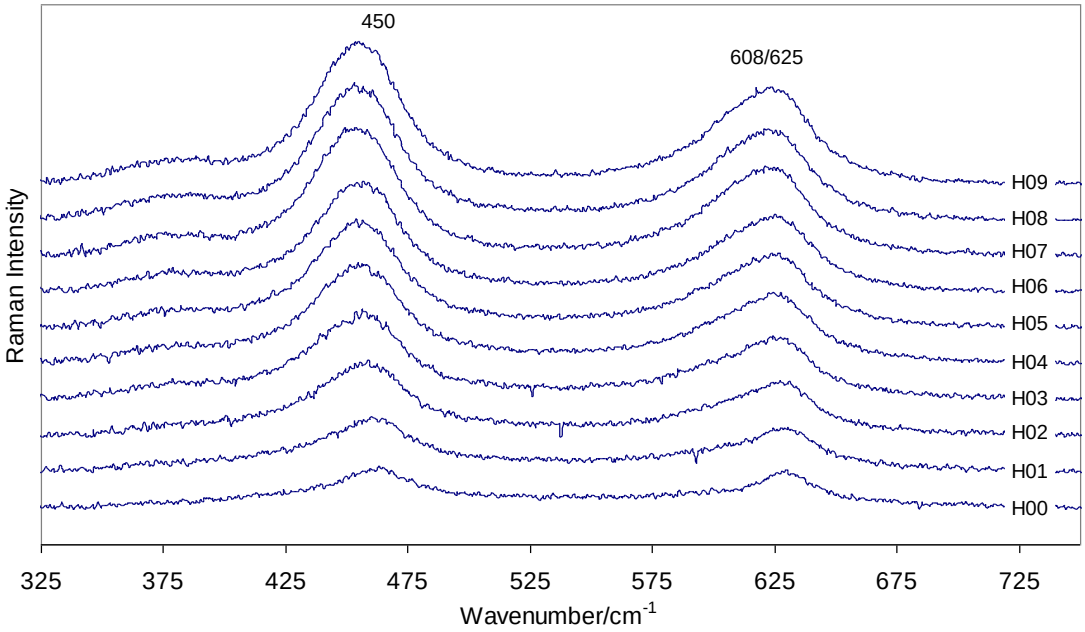

Figure 4.3. Raman spectra of the solutions H00 to H09 in the region 325-750 cm^{-1}. The spectra are normalized to the intensity of the perchlorate band at 935 cm^{-1}, and are intensity-shifted

symmetry breakdown in the SO_4^{2-} tetrahedral structures through formation of monodentate and bidentate ligands. Formation of the latter would cause a split of the v_2 sulfate bending band at 450 cm^{-1} into two components. Such split has not been observed in our Raman spectra, in which the v_2 sulfate bending mode is characterized by a single band exactly at 450 cm^{-1} in all samples. Besides, the shape of this band does not change with iron(II) sulfate concentration. Additionally, such ion-paired structures would be characterized by a shoulder at 1005 cm^{-1} (Tepavitcharova *et al.*, 2005). The self-deconvolution process yields such a shoulder, along with a band at 963 cm^{-1}. The low intensity of both bands makes us think that maybe we have incurred in over-fitting, by selecting too much a Gaussian profile for the 982 cm^{-1} sulfate band. In any case, the interaction between the iron(II) hydration shell and sulfate could also have been facilitated by hydrogen bonds, and would be reflected in the Raman spectra by an increase of the area of the band at 1037 cm^{-1} as the salt concentration is raised (Nakamoto 1997). As previously discussed, the area of that band is independent of $FeSO_4$ concentration. From all the above, we may conclude that there is no or negligible interaction between iron(II) and sulfate at the level of inner-shell, which confirms the infrared spectroscopic results of Majzlan and Myneni (2005).

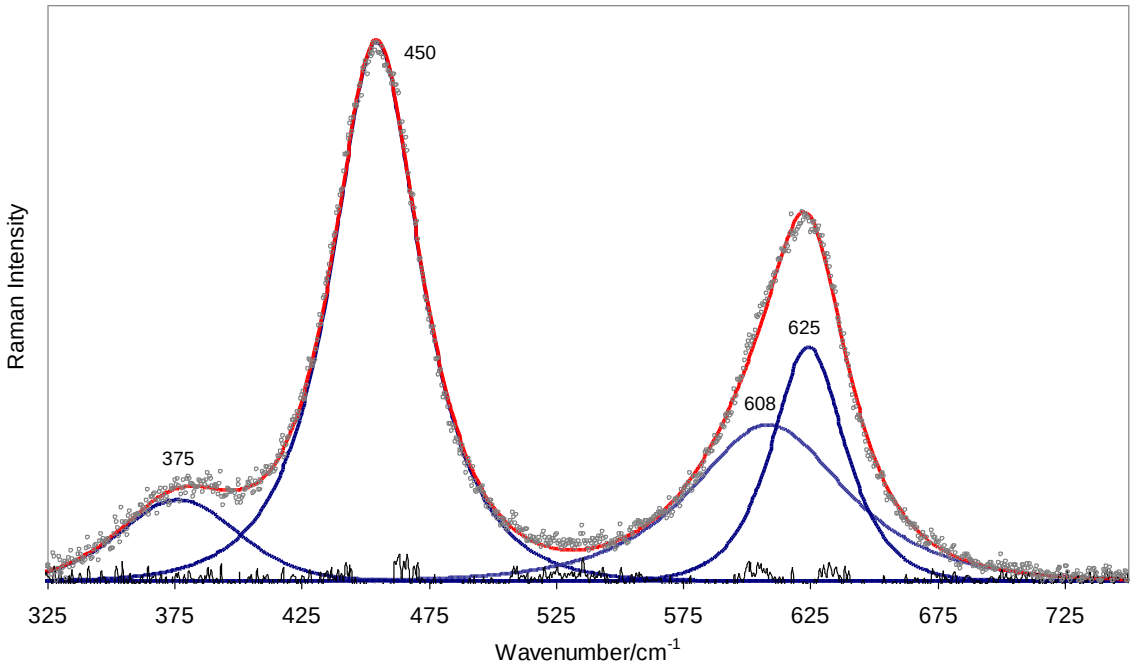

Figure 4.4. Band fitted spectrum in the region 325-750 cm^{-1} of the sample H09. Grey circles represent the original Raman spectrum, blue lines the fitted bands, red line the convolution spectra and black line the residual

The thermodynamic dissociation constant K_2 of the second step in sulfuric acid dissociation in presence of additional $FeSO_4$ is given by (Irish and Chen, 1970):

$$K_2(T) = K_m K_\gamma = \frac{m(SO_4^{2-})m(H^+)}{m(HSO_4^-)} K_\gamma \quad (4.6)$$

where K_m is the concentration product (concentrations in mol/kg) and K_γ is the activity coefficients product. Reardon and Beckie (1987) have derived a set of activity coefficients for the iron(II) sulfate-sulfuric acid-water system in terms of the Pitzer model formulation to calculate the solubility of $FeSO_4 \cdot 7H_2O$ and $FeSO_4 \cdot H_2O$. In this work we have derived the activity coefficients product K_γ for the bisulfate-sulfate equilibrium as a function of iron(II) sulfate concentration from experiments. Following Dawson *et al.* (1986) we accept the literature value of K_2 at 20 °C and then derive K_γ from Eqn (4.6):

$$K_\gamma = K_2 K_m^{-1} \quad (4.7)$$

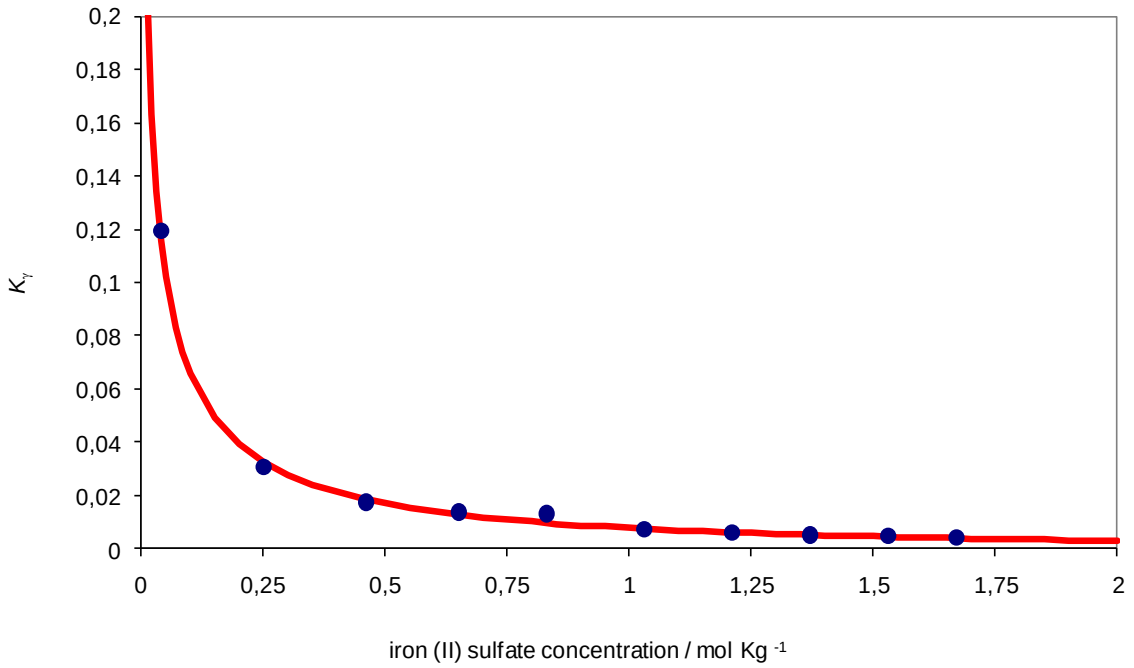

Figure 4.5. Activity coefficients product, K_γ plotted against iron(II) sulfate concentration. Blue dots, experimental; red line, empirical function (Eqn (4.8))

The value of K_2 = 0.0120 was obtained from the parameterization of Lietzke *et al.* (1961) of K_2. The values of K_γ are included in Table 4.1, and plotted versus salt concentration in Figure 4.5. From a physico-chemical point of view the activity coefficients product is introduced into equilibrium in order to describe its non-idealities. Thus the variation within two orders of magnitude of the values of K_γ shows that the system iron(II) sulfate-sulfuric acid-water is highly non-ideal. The following function has been found to best correlate K_γ and the molality of iron(II) sulfate*:*

$$\ln(K_\gamma) = -4.8434 m(\mathrm{FeSO_4})^{0.25} + 0.0111 \qquad (4.8)$$

4.3. Speciation of the system iron(III)-sulfuric acid-water

4.3.1. Abstract

Acid mine drainage is formed when pyrite (FeS_2) is exposed and reacts with air and water to form sulfuric acid and dissolved iron. Rio Tinto is an example of this phenomenon. In this study, Raman spectroscopy has been used to investigate the speciation of the system iron(III)-sulfuric acid-water as an approach to Rio Tinto aqueous solutions. The molalities of sulfuric acid (0.09 mol/kg) and iron(III) (0.01 to 1.5 mol/kg) were chosen to mimic the concentration of the species in Rio Tinto waters. Raman spectra of the solutions reveal a strong iron(III)-sulfate inner-sphere interaction through the v_1 sulfate band at 981 cm^{-1} and its shoulder at 1005 cm^{-1}. Iron(III)-sulfate interaction may also be facilitated by hydrogen bonds and monitored in the Raman spectra through the symmetric stretching band of bisulfate at 1052 cm^{-1} and a shoulder at 1040 cm^{-1}. Other bands in the low-frequency region of the Raman spectra are attributed to the hydrogen-bonded complexes formation as well.

4.3.2. Experimental

4.3.2.1. Sample preparation

A set of eight solutions containing iron(III) chloride, sulfuric acid, and water were examined. Solid hexahydrated iron(III) chloride ($FeCl_3 \cdot 6H_2O$, Panreac), concentrated sulfuric acid of p.a. quality (95-97% in H_2O, Scharlau) and distilled water were used to prepare the samples. Distilled water was acidified with 0.090 mol/kg sulfuric acid in order to obtain the set of aqueous sulfuric acid solutions with pH = 1, measured with a glass electrode calibrated with pH 7.00 and 4.01 buffer solutions. $FeCl_3$ was added to the aqueous sulfuric acid solutions in concentrations ranging 0.01 to 1.5 mol/kg. Table 4.2 shows the composition of the studied samples. All samples were kept at a constant temperature of 23 °C during preparation and analysis.

Table 4.2. Composition of the iron(III)-sulfuric acid-water mixtures

Sample ID	$m(Fe^{3+})$	$m(H_2SO_4)$
P11	0.01	0.09
P12	0.02	0.09
P13	0.05	0.09
P14	0.1	0.09
P15	0.2	0.09
P16	0.5	0.09
P17	1	0.09

4.3.2.2. Raman experiments

Raman spectra of the solutions of iron(III)-sulfuric acid-water were collected at constant temperature of 23 °C with a JOBIN–YVON T64000 spectrometer (*cf*. 2.3) within the spectral range 250-3800 cm^{-1}. The achieved spectral resolution was 4 cm^{-1}. The 532.4 nm line of a Sirah Nd:YVO_4 laser was used as the excitation source. Raman spectra were obtained under rigorously constant conditions of excitation intensity and sample positioning relative to the laser beam. The spectra are thus comparable.

4.3.3. Results and discussion

Processing of the original Raman spectra was performed with software described in chapter 3. The spectra were first filtered, smoothed and baseline corrected using improved FFT algorithms in order to remove both sample's fluorescence emissions and noise introduced by the apparatus. These operations are required for further spectral analysis, *e.g.*, band-fitting. The optimization of fitted bands yields the so-called best-fit parameters that provide the quantitative information of the Raman spectra. Figure 4.6 shows the band-fitted spectrum of solution P17 in three regions: low wavenumbers (240-600 cm^{-1}), mid wavenumbers (900-1200 cm^{-1}) and OH stretching region (2700-3800 cm^{-1}).

Raman spectra of the samples P10 to P17 are shown in Figure 4.7 and the results of the spectral analysis collected in Table 4.3. As seen in Figure 4.6 the Raman spectrum in the low wavenumbers region comprises three bands centered at 315, 420,

and 480 cm^{-1}. However, only one broad band is observed in the Raman spectra of the samples P10 to P12, centered at 450 cm^{-1}. It belongs to the v_2 vibrational mode of sulfate (*cf*. 3.2) and is the only observable band at low iron(III) concentration. The intensity of the bands is very weak, though, and the convergence of the band-fitting is not good in this case. The derived values shown in Table 4.3 for samples P10 to P12 must be regarded with caution. When the iron concentration exceeds 0.1 mol/kg (samples P13 to P17) the sulfate band at 450 cm^{-1} turns into an envelope composed of two bands at 420 and 480 cm^{-1}, whereas the band at 315 cm^{-1} become intense enough to be quantified. Formation of $Fe(H_2O)_{6-n}(O)_n$ octahedra, with *n* oxygens from sulfate groups entering in the inner Fe^{3+} shell has been previously reported (Magini, 1979). The large increase of the intensity of the band at 315 cm^{-1} as a function of iron(III) may be attributed to the Fe-O stretching vibration. However, independent measurements showed that the Raman spectra of supersaturated solutions of aqueous $FeCl_3$ present a band at approximately 320 cm^{-1}. Hence the assignation of the 315 to the Fe-O vibrations is not unambiguous. Speciation of iron(III) and sulfate in sulfuric acid solutions has been characterized by infrared spectroscopy (Majzlan and Myneni, 2005; Lazaroff *et al.*, 1982) and molecular bonds are assigned to certain bands in the infrared spectra. Regarding Raman spectroscopy, there are many Raman spectroscopic studies of the jarosite mineral group and other iron and sulfate rich minerals (Frost *et al.* 2000, 2005, 2006a, 2006b; Chio *et al.*, 2005; Sharma *et al.* 2006). Jarosites are based upon the formula $M_n(Fe^{3+})_6(SO_4)_4(OH)_{12}$ where M can be a monovalent or divalent cation with n = 1 or 2 respectively. Sulfate minerals like jarosites precipitate in solutions containing iron(III), sulfate, and water.

As stated by Frost *et al.* (2000), the inclusion of oxygens from sulfate units in the Fe^{3+} octahedra leads to charge delocalization or loss of symmetry in the SO_4^{2-} tetrahedral structures through formation of monodentate and bidentate ligands. Formation of the latter leads to a splitting of the v_2 sulfate bending band at 450 cm^{-1} into two components. This is also consistent with the attribution of this envelope of bands around 450 cm^{-1} to the bisulfate ion (Table 2.1), as its concentration is significant. The intensities of the bands at 420 and 480 cm^{-1} increase strongly as

iron(III) concentration increases. Such an increase in these two Raman bands must be associated with a strong interaction between sulfate and iron(III), probably through hydrogen bonds. A representation of the most likely hydrogen-bonded complexes can be found elsewhere (Majzlan and Myneni, 2005).

Other sulfate bands are found in the mid wavenumbers region centered at 981 cm^{-1} and 1105 cm^{-1}. They belong to the v_1 and v_3 symmetric stretching modes of sulfate, respectively (*cf*. 2.2). Due to the low concentration of sulfate in the samples the band at 1105 cm^{-1} is barely detectable. The v_1 band is intense enough to be quantified although the spectra are quite noisy. The band at 1052 cm^{-1} shows a shoulder at 1040 cm^{-1}. Both peaks belong to S-O-H symmetric stretching of bisulfate. The Raman spectra of the prepared solutions in the 900-1200 cm^{-1} region (Figure 4.7) show another shoulder at 1005 cm^{-1}. Shoulders at 1005 cm^{-1} and 1040 cm^{-1} are, as was previously described, associated with a distortion of sulfate and bisulfate ions by hydrogen bonding and Fe^{3+} direct complexation. The increase of iron(III) concentration, and therefore the increase of sulfate linkages with Fe^{3+} octahedra, is reflected in the Raman spectra of Figure 4.7 by an increase of the intensity of the bands at 1005 and 1040 cm^{-1}. The values of the intensity of the bands at 1005 and 1040 cm^{-1} for samples P16 and P17 in Table 4.3 were expected to follow the upward trend of samples P10-P16. However, this is not the case. The Raman spectra of samples P16 and P17 show a poor signal-to-noise ratio and band parameters are in this case extremely sensitive to small variations in experimental and band-fitting processing. Again, the values given in Table 4.3 for the band parameters of the bands at 1005 and 1040 cm^{-1} should be observed cautiously.

The region from 2700 to 3800 cm^{-1} relates to the OH stretching modes of liquid water and the bisulfate ion. The Raman OH stretching contour obtained in this wavenumbers range may be deconvoluted into three bands centered at 3235, 3445 and 3610 cm^{-1}. The Raman OH stretching bands arise from various amounts of hydrogen bonding, and their intensities thus change as the hydrogen-bonded structure of water is modified by addition of iron(III). The intensity of the three Raman bands, in

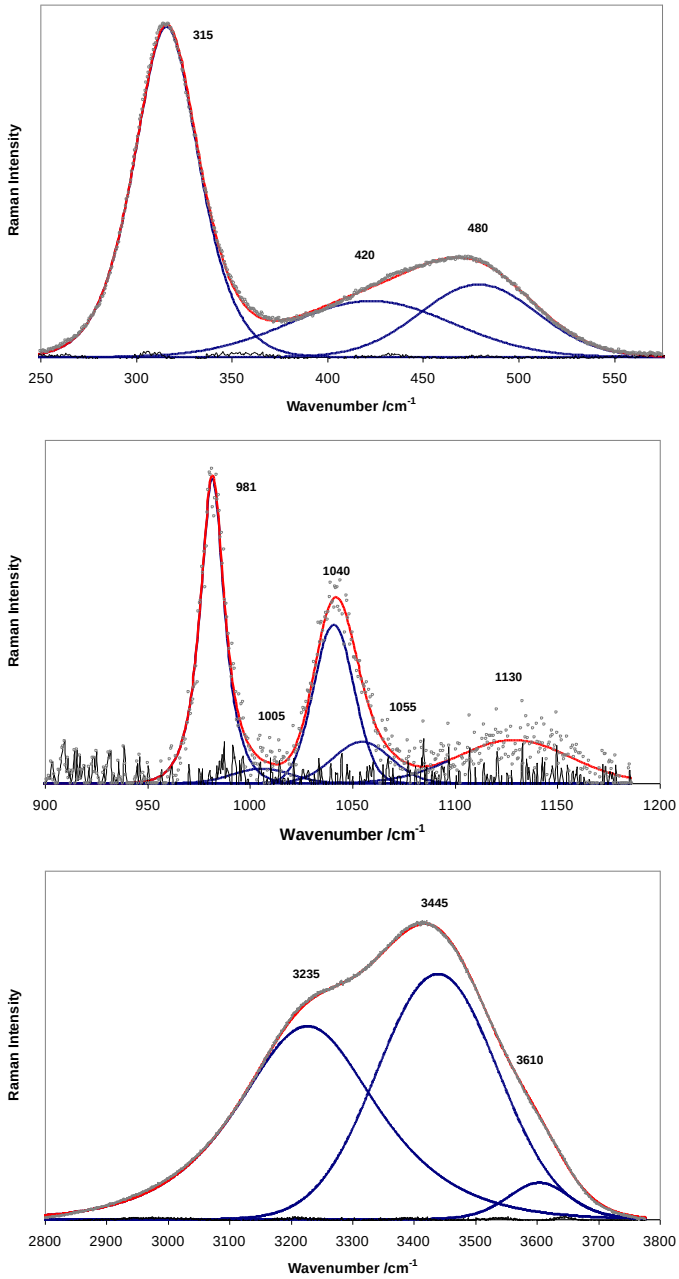

Figure 4.6 Raman spectra and band fitting of sample P17 in the 250-600 cm^{-1}, 900-1200 cm^{-1}, and 2800-3800 cm^{-1} regions. Grey circles represent the original Raman spectra, blue lines the fitted bands, red line the convolution spectra and black line the residual.

particular that centered around 3200 cm^{-1}, in the 2700-3800 cm^{-1} region tends to decrease as iron(III) concentration increases, as depicted in Table 4.3. This lowering of the intensity of the 3200 cm^{-1} OH stretching bands (Dubessy *et al.*, 2002), *i.e.*, this distortion of the H-bonded water network, is consistent with the progressive formation of Fe^{3+}-$(H_2O)_6$ octahedra plus other associated species as iron(III) concentration is increased.

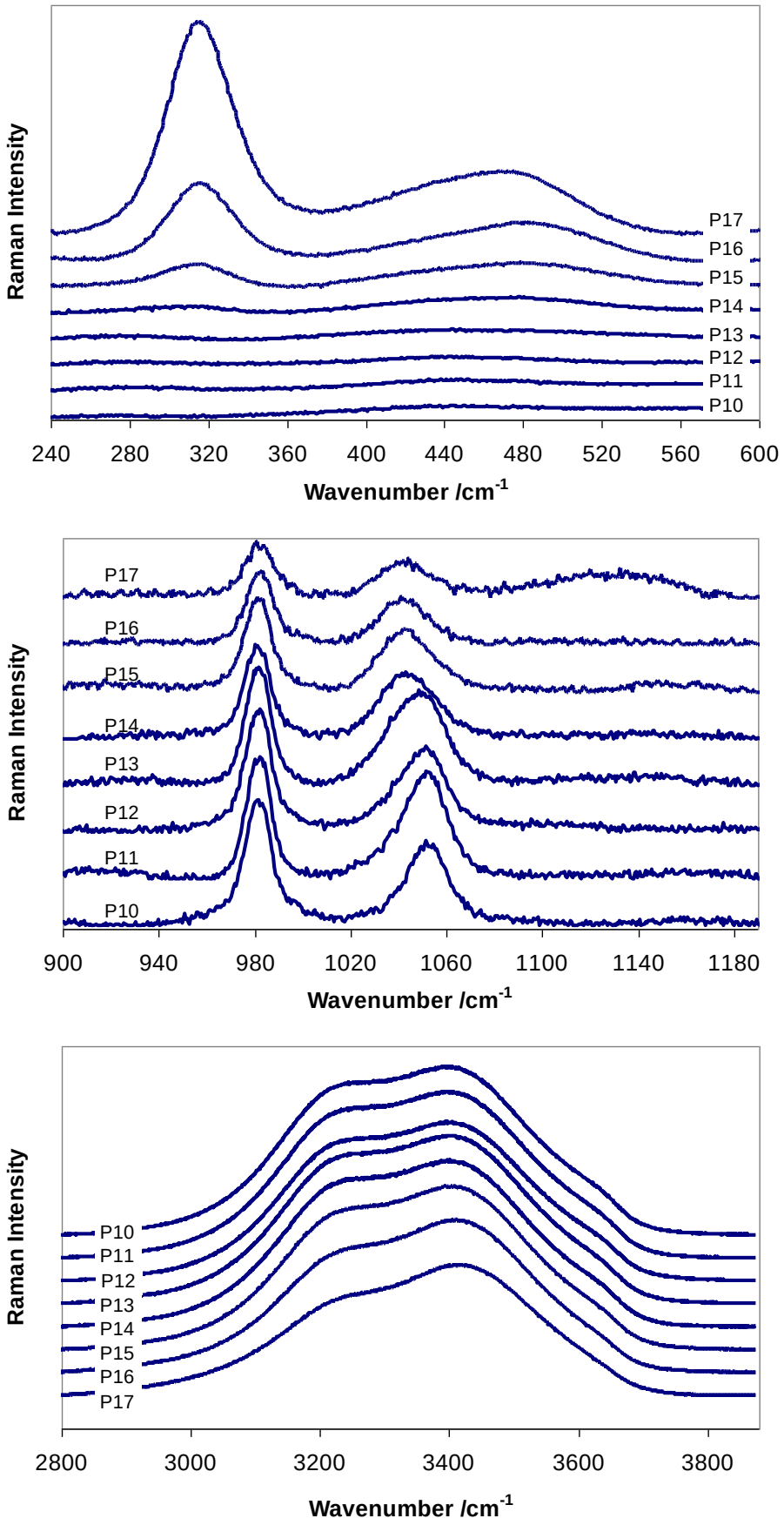

Figure 4.7. Raman spectra of the solutions P10 to P17 in the low, mid, and high-wavenumbers regions. Spectra are intensity shifted to avoid overlapping

Table 4.3. Results of the Raman spectra of the samples

P10				P11			
Position	Intensity	Width	GL factor	Position	Intensity	Width	GL factor
448.0	869.7	80.0	1.0	448.0	839.0	80.0	1.0
-				-			
981.5	1720.5	6.1	0.2	981.7	1670.4	6.7	0.2
1006.5	5.6	10.0	1.0	1006.5	36.2	10.0	1.0
1043.4	418.4	22.3	1.0	1043.0	533.0	23.8	1.0
1052.6	845.4	10.1	1.0	1052.3	1096.8	11.0	1.0
1124.0	39.4	49.0	1.0	1124.0	109.5	50.0	1.0
3211.4	9686.8	117.4	0.2	3211.4	9410.5	117.0	0.2
3420.9	11560.4	150.0	1.0	3420.9	11480.3	157.1	1.0
3606.6	2001.0	71.4	0.5	3606.6	1690.9	64.3	0.5

P12				P13			
Position	Intensity	Width	GL factor	Position	Intensity	Width	GL factor
448.0	826.3	80.0	1.0	282.8	494.5	15.0	0.3
-				429.4	353.9	43.2	1.0
981.6	1640.4	6.8	0.2	486.5	653.8	83.9	0.9
1006.5	92.5	11.6	1.0	981.6	1552.5	6.8	0.2
1042.7	600.3	20.4	1.0	1006.5	120.7	11.6	1.0
1052.2	738.0	11.1	1.0	1042.7	732.5	20.4	1.0
1124.0	78.1	50.0	1.0	1052.2	569.3	11.1	1.0
3211.4	9220.0	118.7	0.2	1124.0	93.0	50.0	1.0
3420.9	11440.2	158.8	1.0	3211.4	9080.4	120.6	0.2
3606.6	1560.8	64.8	0.5	3420.9	11395.0	160.0	1.0
				3606.6	1480.2	59.3	0.5

P14				P15			
Position	Intensity	Width	GL factor	Position	Intensity	Width	GL factor
302.4	695.5	15.9	0.3	312.4	2355.7	17.7	0.3
430.9	307.0	32.9	1.0	420.6	471.3	34.1	1.0
479.0	1166.8	62.5	0.9	485.0	1887.2	60.0	0.9
981.1	1430.4	6.5	0.2	981.7	1358.5	6.9	0.2
1006.0	194.4	20.0	1.0	1006.0	222.6	15.0	1.0
1040.0	872.8	15.5	1.0	1042.0	904.1	17.0	1.0
1054.2	334.7	17.0	1.0	1054.5	67.2	20.0	1.0
1142.0	109.5	50.0	1.0	1142.0	92.1	50.0	1.0
3211.4	8868.8	118.8	0.2	3211.4	8379.0	120.8	0.2
3420.9	11288.0	157.8	1.0	3420.9	11154.7	157.8	1.0
3606.6	1402.6	60.7	0.5	3606.6	1357.1	64.1	0.5

Table 4.3. (cont.)

P16				P17			
Position	Intensity	Width	GL factor	Position	Intensity	Width	GL factor
307.7	6983.5	19.3	0.3	315.7	17727.2	21.9	0.3
411.3	1024.7	41.5	1.0	427.4	2914.0	72.1	1.0
474.2	2851.1	49.0	0.9	476.3	3432.3	44.5	0.9
974.0	1051.4	7.2	0.2	981.9	770.0	8.0	0.2
998.0	132.6	15.0	1.0	1006.0	81.2	15.0	1.0
1034.0	982.0	19.0	1.0	1042.0	820.0	16.7	1.0
-				-			
1134.0	136.4	50.0	1.0	1142.0	34.6	33.9	1.0
3202.7	7388.9	127.7	0.2	3214.3	6152.9	139.5	0.2
3420.4	10463.4	158.6	1.0	3436.4	8769.5	153.1	1.0
3602.1	945.6	53.8	0.5	3610.5	824.0	56.4	0.5

4.4. Diffusion of chemical species in the system sulfuric acid-water

4.4.1. Introduction

The process of mass diffusion or mass transfer in fluids involves the transport of molecules as a response to a concentration gradient within a physical system. This process plays an important role in many fields of chemistry and physics. The discharge and subsequent diffusion of acid and metals into aquatic systems is a matter of special relevance in environmental sciences. A very sound example of stream and groundwater contamination by acid sulfate waters is the acid rock drainage (ARD). Acid is generated when metal sulfide minerals are oxidized and sufficient water is present

to mobilize dissolved ions. The process of ARD is often explained in terms of pyrite oxidation (Nordstrom, 1982; Nordstrom and Alpers, 1999a; Nordstrom, 2000) and may be grossly simplified in the following reaction (Bigham and Nordstrom, 2000):

$$FeS_{2(aq)} + 3.75O_{2(g)} + 3.5\ H_2O_{(l)} \leftrightarrows Fe(OH)_{3(s)} + 2H_2SO_{4(aq)} \quad (4.9)$$

Although the ARD is a natural process, human activities such as mining dramatically accelerate these geochemical reactions rates by providing greater exposure of minerals to air and water through mine workings, waste rock and tailings. ARD is also commonly known as acid mine drainage AMD when found in mine-related areas. In the last decades, AMD has become a big and expensive concern (U.S. Environmental Protection Agency, 1994).

Final products in Eqn (4.9) include aqueous sulfuric acid which rapidly dissociates in bisulfate and sulfate as explained in section 4.2 and is the direct cause of acidification of streams. This acidification happens when the aqueous solutions rich in SO_4^{2-}, H^+, Fe^{2+} diffuses into stream waters (Nordstrom and Alpers, 1999b). The dissolved contaminants migrate to ground and surface waters through diffusive phenomena. It would be highly desirable to model these processes in order to predict the properties of the drainage based, for instance, on the rate of acid formation. Such models should take into account all of the major and trace dissolved ions and the association/dissociation processes among them. These systems are non-ideal multicomponent liquid mixtures whose structure is not known, mainly because there is large uncertainty in the available data for the activity coefficients in multicomponent systems.

In this work we focus on the study of the diffusion properties of the simplest aqueous system approaching the AMD, sulfuric acid-water, as the natural starting point for modeling the physico-chemistry of diffusion in AMD. We propose a model for the diffusion of aqueous sulfuric acid into water that (1) is based on the diffusion of the individual molecular species present in the system, (2) takes account of the association-dissociation phenomena among these species and (3) uses a non-constant effective diffusion coefficient. Strictly speaking, the diffusion of species is explained in

terms of gradients of chemical potential (Bird *et al.*, 2002). The expressions are however extremely complex, and one can deal with them only if a model that describe the non-ideality of the system is available. Several models for the system sulfuric acid-water have been reported (*e.g.* Clegg *et al.*, 1994; Clegg and Brimblecombe, 1995; Knopf *et al.*, 2003), however large discrepancies are found among them when comparing the values for the model parameters. In order to overcome this difficulty, and in the absence of a definitive model involving the chemical potential of the species, it is assumed that the diffusion coefficient is a complex function of the concentration of the chemical species. In this work we have approximated the diffusion coefficient to a linear function of the concentration. This is the common approach when describing physical processes. In fact, we have corroborated this linear dependence experimentally. The diffusion coefficient is called effective here since it is no longer a physical property but a model parameter related to the diffusion of a single species *i* into a medium composed by all the species (water, sulfate, bisulfate and protons).

The effective diffusion coefficient is set as an adjustable model parameter which is optimized to reduce the deviation between the model and experimental data for the values of the species concentrations measured as a function of time and space. Experimental concentrations have been monitored as time-profiles by means of Raman spectroscopy. Previous findings on the Raman measurements of the diffusion properties of liquid mixtures have been reported elsewhere (*e.g.*, Rodriguez *et al.*, 1995). The laser Raman technique allows for a fast and direct measurement of the absolute concentration of the species within the system, and since it is non-invasive it does not affect the equilibriums among species. Furthermore, the Raman technique does not suffer from the severe constrains of interferometric techniques, traditionally used for diffusion studies (Gabellman-Gray and Fenichel, 1979), regarding optical alignment, and from the relative ambiguity in the connection of species' concentrations with the scalar variables (*e.g.*, refractive index) this methods often make use of.

4.4.2. Diffusion model

4.4.2.1. Model development

The diffusion model is formulated in order to estimate the concentrations of bisulfate, sulfate, protons and water as a function of time and distance. The simplest (and therefore likely the best) way to approach this problem may be to consider a mathematical system involving four equations which relate four dependent variables, the concentrations of the four species, and two independent variables, time and height. According to the physico-chemical constrains that rule the diffusion mechanisms in the system under study (Figure 4.8), the four equations may be expressed as follows:

Chemical equilibrium:

It is assumed that the chemical equilibriums among molecular species are achieved instantly. As described in section 4.2, sulfuric acid dissociates in two steps. Let c_1, c_2 and c_3 be the concentrations of bisulfate, sulfate and protons, respectively expressed in concentration units, mol L^{-1}. Then we may write:

$$\underset{c_1}{HSO_4^-} \rightleftarrows \underset{c_2}{SO_4^{2-}} + \underset{c_3}{H^+} \longrightarrow K = \frac{c_2 c_3}{c_1} K_\gamma \qquad (4.10)$$

where K is the thermodynamic dissociation constant and K_γ is the activity coefficients product for concentrations expressed in mol L^{-1}. As we deal with highly non-ideal solutions, we must include the activity coefficients product into the expression of the thermodynamic dissociation constant, K. The value of the thermodynamic dissociation constant remains equal to 0.01 since it is a function of the temperature only, and this is kept stable at 20 °C along the experiment. As a consequence, the equilibrium, or the relationship among electrolytes concentration, is ruled by the activity coefficients product alone. Figure 4.9 shows the experimentally derived values of K_γ for this

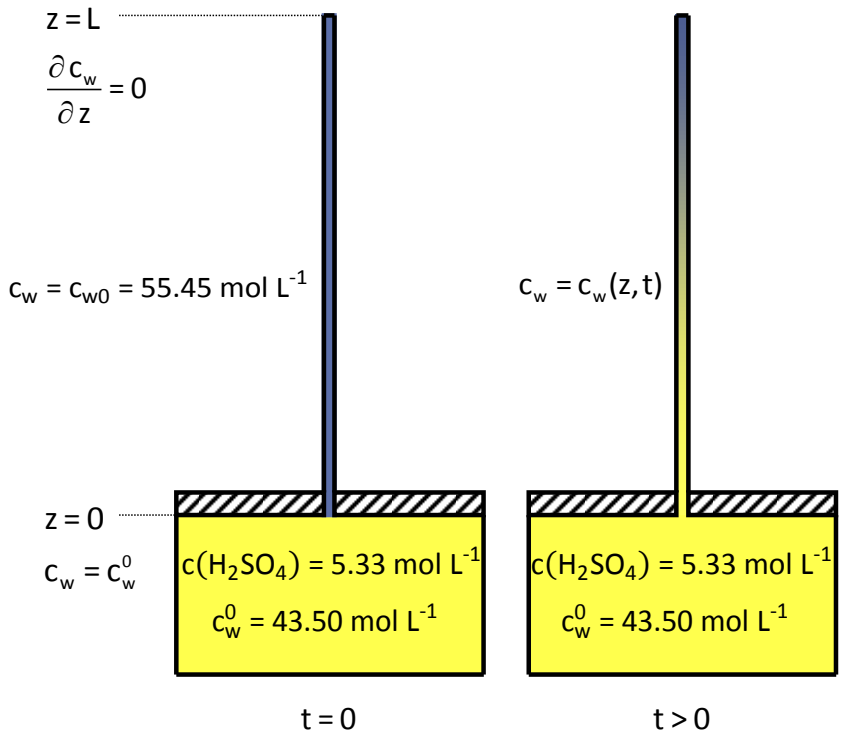

Figure 4.8. Diagram of the experimental setup. To ensure that the volume is constant along the experiment, a sealed vessel has been completely filled with an aqueous solution of sulfuric acid. A glass tube filled up with pure water is placed vertically in contact with the sulfuric solution, thus facilitating the diffusion of sulfuric acid along the tube. The pure water diffuses into the aqueous sulfuric acid as well. However the model doesn't take this diffusion process into account since the volume of pure water in the tube can be neglected with regard to that of aqueous sulfuric acid in the vessel. The initial condition indicates that before diffusion starts, the water concentration within the tube is 55.35 mol L^{-1}. The boundary conditions state that there is no diffusive flux through the upper part of the tube (*i.e.*, the tube is closed) and that the water concentration at the bottom part of the tube equals the water concentration in the vessel, 39.43 mol L^{-1}. The tube dimensions are chosen in such a way that diffusion occurs on the Z axis only. In our setup *L* (length of the tube) and *d* (inner diameter) equal 31 and 0.5 mm, respectively. With this dimensions, the radial diffusion measures less than 1% of the axial diffusion and is no considered in the model. A very little amount of lithium perchlorate (0.24 mol kg^{-1}) was added to both the aqueous sulfuric acid in the vessel and the pure water in the tube in order to provide an internal reference for the quantitative analysis of the Raman spectra. This tiny amount of internal reference doesn't affect the equilibriums and the diffusion of chemical species.

experiment. The trend of K_γ can be modeled as a function of c_2 with the following function:

$$\ln(K_\gamma) = \ln(1 + c_2) - Ac_2^{0.25} - Bc_2 \qquad (4.11)$$

where *A* and *B* are two parameters to be optimized. This function was also found to fit well the experimental values for the activity coefficients product derived in section 4.2.

Chemical stoichiometry:

Chemical stoichiometry leads to the electric charge conservation law, *i.e.*, the total electric charge remains constant at all times. Then,

$$0 = c_3 - 2c_2 - c_1 \tag{4.12}$$

Equation of state:

One possible equation of state for this system may be to assume that the density of the system is a linear function of the concentration of sulfuric acid (Perry and Green, 1997), *i.e.*:

$$\rho = \rho_0 + \rho_1(c_1 + c_2) = c_t\overline{M} = c_w M_w + c_1 M_1 + c_2 M_2 + c_3 M_3 \tag{4.13}$$

where ρ_0 and ρ_1 are the coefficients of the expansion terms of ρ with values 998.2 (density of water at 20 °C in g L^{-1}) and 57.624, respectively, $\overline{M}$ is the mean molecular mass, c_t is the total concentration of the system, c_w is the concentration of water, and M_i is the molecular mass of species *i*.

Balance of matter:

The fourth equation is a mass balance for one of the dissolved molecular species. As water is the major species in the current system, the concentration of water has been chosen for defining the mass balance, which obeys Fick's law of diffusion (Bird *et al.*, 2002):

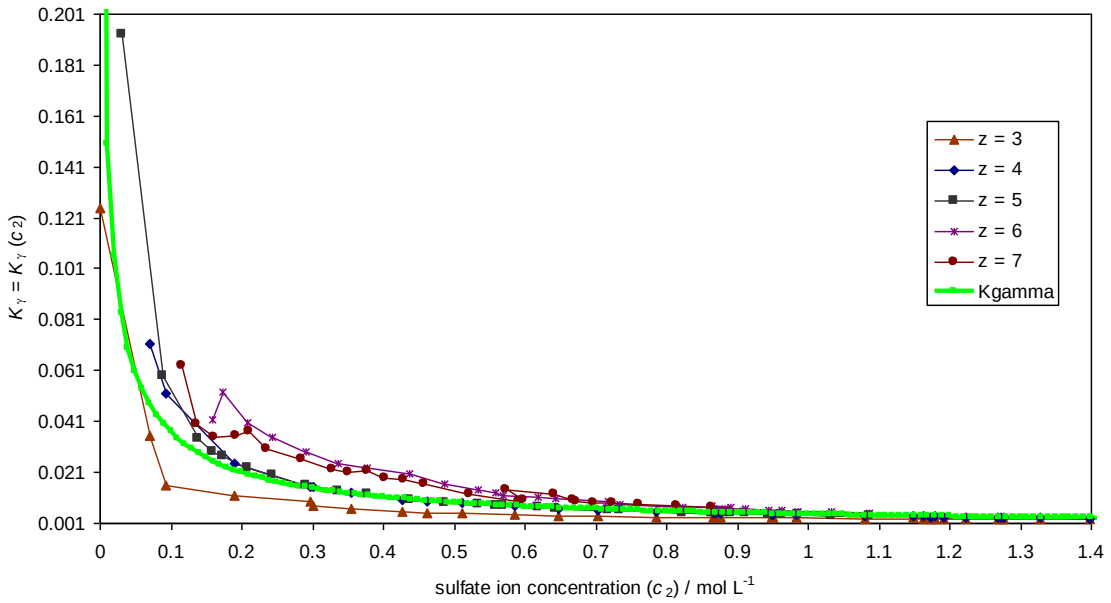

Figure 4.9. Experimentally derived activity coefficients product for different heights (thin lines) and the adjusted function K_γ in Eqn (4.11) with A = 6.02433 and B = 0.09050 (thick green line) plotted against sulfate concentration. The values of the parameters A and B have been optimized in order to fit the experimentally derived values of K_γ

$$\frac{\partial c_w}{\partial t} = -\frac{\partial J_w}{\partial z} = \frac{\partial}{\partial z}\left(D_w^{(c)}\frac{\partial c_w}{\partial z}\right) \tag{4.14}$$

where J_w is the density of diffusive flux for water, z is the height, t is the time, and $D_w^{(c)}$ is the water effective diffusion coefficient. The superscript in D_w indicates that this parameter is concentration-dependent, mainly due to the highly non-ideal system we are dealing with. This diffusion equation meets the initial and boundary conditions described in Figure 4.8. In fact, the Fick's law of diffusion is established in terms of gradients of the molar fractions. However, if we assume the total concentration in the system to be approximately constant, the Fick's law may be rewritten for the species concentration for the same definition of $D_w^{(c)}$.

The balance of matter in Eqn (4.14) includes no convective term. In liquid mixtures the convective phenomena are due to changes in the density as a consequence of temperature and concentration variations. Temperature doesn't play a role in the convective properties in our systems since the system itself is isothermal.

The only convective motion would be caused by variations of the density of the system with the concentration, but only if the concentration was higher in the upper part of the tube of the diffusion tube. This is not the case for our experimental setup, hence the convective phenomena generate no molecular motion, and all the molecular motion is due to diffusion phenomena alone.

Equations (4.10) to (4.14) can be rearranged into the following system of algebraic-differential equations, which make up the body of the diffusion model under the current experimental conditions:

$$K = \frac{c_2 c_3}{c_1} K_\gamma = \frac{c_2 c_3}{c_1}(1 + c_2) e^{-A c_2^{0.25} - B c_2} = 0.01$$

$$c_3 = 2c_2 + c_1$$

$$c_1 = \frac{\rho_0 - (M_2 + 2M_3 - \rho_1)c_2 - M_w c_w}{M_1 + 2M_3 - \rho_1} \qquad (4.15)$$

$$\frac{\partial c_w}{\partial t} = -\frac{\partial J_w}{\partial z} = \frac{\partial}{\partial z}\left(D_w^{(c)} \frac{\partial c_w}{\partial z}\right) \begin{cases} \forall z, t = 0 \Rightarrow c_w = c_{w0} \\ \forall t, z = 0 \Rightarrow c_w = c_w^0 \\ \forall t, t = L \Rightarrow \dfrac{\partial c_w}{\partial z} = 0 \end{cases}$$

4.4.2.2. Model solution

Equation (4.15) describes a non-linear diffusion model, thus no analytical solution can be obtained for it. Numerical methods are required in order to solve the model, whose solution is therefore approximate. The partial differential equation (PDE) can be solved numerically by transforming the continuous domain of the independent variable *t* by a mesh of discrete points, thus converting the PDE into a set of ordinary differential equations (ODEs). This methodology is commonly known as the finite difference method (Morton and Mayers, 2005). We have developed a routine based on the Runge-Kutta fifth-order algorithm (Press *et al.*, 1992) for the resolution of the system of ODEs.

The algebraic equations relate the concentrations of the species, expressed as a function of c_w. Figure 4.10 shows the concentrations of water, sulfate, bisulfate and protons as functions of time and height upon solving the diffusion model in Eqn (4.15) for:

$$D_w^{(c)} = \alpha + \beta \times H(c_w) \tag{4.16}$$

where the function $H(c_w)$ is expressed as follows:

$$H(c_w) = \frac{1}{1 + e^{-p\left(\frac{c_w - 55.45}{m - 55.45}\right)}} \tag{4.17}$$

where *α*, *β*, *m* and *p* are parameters.

4.4.3. Experimental derivation of species concentrations

Raman spectra were collected at constant temperature of 20 °C with a Horiba Jobin-Yvon T64000 spectrometer (*cf*. 2.3) within the spectral range 250-1900 cm^{-1}. The achieved spectral resolution was of 4 cm^{-1}. The 532.4 nm line of a Spectra-Physics Millenia Pro (Nd:YVO_4 crystal diode-pumped) laser was used as excitation source. A Raman probe (Raman Superhead Horiba Jobin-Yvon) connected to the base analyzer by fiber optic cables was used for Raman analysis measurements. The probe was mounted on a custom-made vertical positioning system to allow for vertical motion along the tube in 1 cm-height steps. A total of 432 Raman spectra were recorded at 16 heights along the course of nearly 350 hours. Figure 4.11 shows ten Raman spectra collected at t = 213 h and variable height. The spectra have been normalized to the intensity of the perchlorate band at 935 cm^{-1} for the sulfate and bisulfate band intensities to be compared. As expected, these intensities, and therefore the ions concentration, decrease as height increases for a fixed time, 213 h in this case.

The filtering, baseline correction, band self-deconvolution and band-fitting routines described in chapter 3 were applied to the spectra. Figure 4.12 shows the

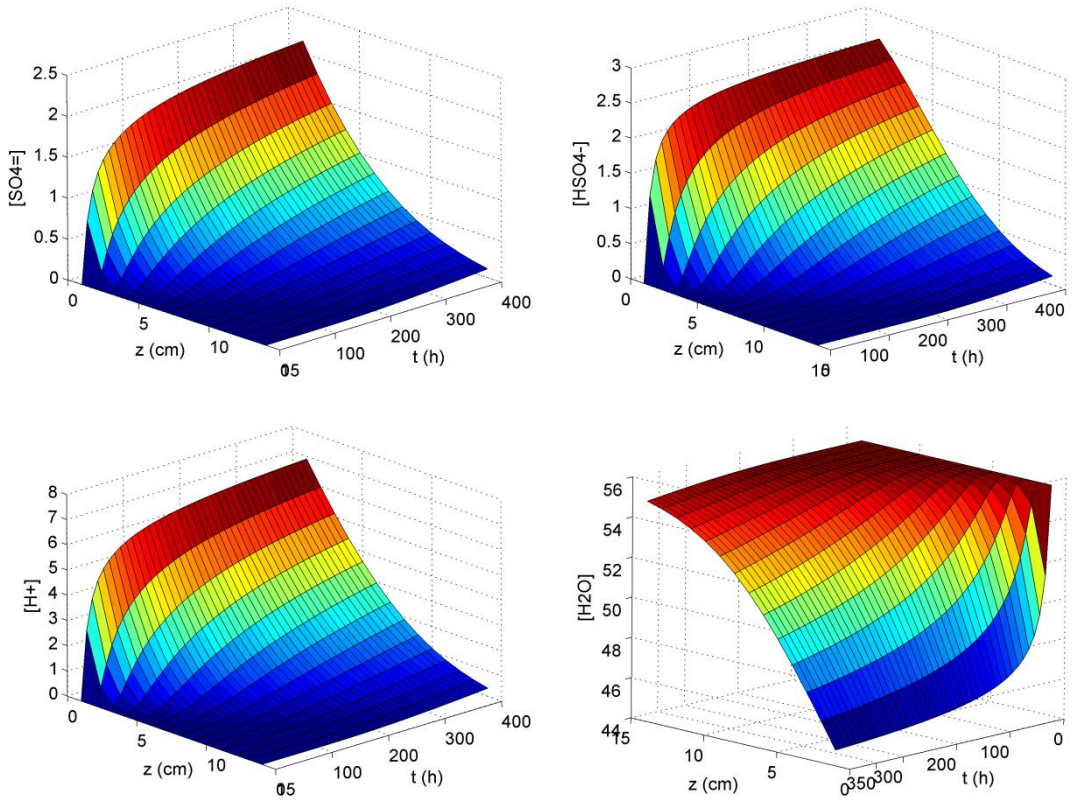

Figure 4.10. Concentrations of sulfate, bisulfate, protons and water as calculated from the diffusion model in Eqn (4.15). Concentrations are in mol L^{-1} and are plotted as function of time and height. The values of the optimizing parameters are as shown in Table 4.4.

Raman spectrum collected at z = 3 cm and t = 213 h in the 700-1300 cm^{-1} range. Following the band assignment discussed in section 2.2, the bands centered at 982 cm^{-1} and 1052 cm^{-1} are attributed to the sulfate and bisulfate symmetric stretching vibrations, respectively. The symmetric stretching vibration of the perchlorate ion gives rise to an intense band at 935 cm^{-1} (Nakamoto, 1997). It is widely accepted that there is a linear relationship between the intensity of a Raman band and the concentration of the molecule associated to it. Applied to our case, this means that the intensities of the 982 and 1052 cm^{-1} bands are proportional to the concentration of sulfate and bisulfate, respectively.

The internal reference allows for obtaining absolute values for the concentrations through the so-called molal scattering coefficients. The molal scattering coefficient of sulfate and bisulfate relative to perchlorate are computed, on the basis of six independent measurements, as:

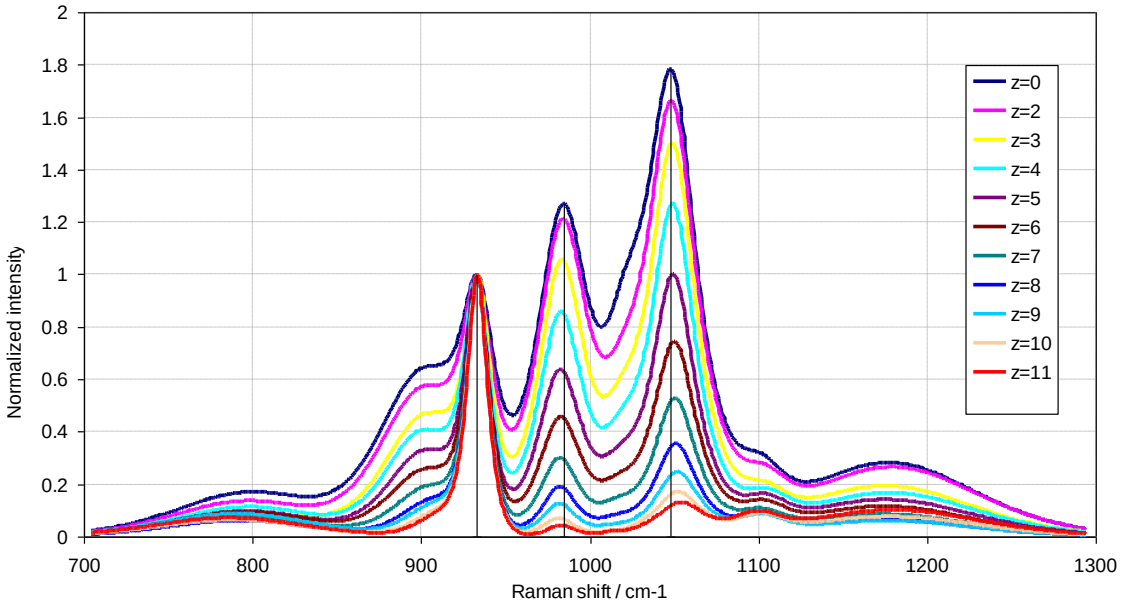

Figure 4.11. Raman spectra recorded at *t* = 213 h and variable heights. The spectra have been normalized to the intensity of 935 cm^{-1} band

$$k_s = \frac{J(982)/J(935)}{m(SO_4^{2-})} = 0.8802$$
$$k_b = \frac{J(1052)/J(935)}{m(HSO_4^{-})} = 0.9096 \qquad (4.18)$$

Thus the concentration of sulfate and bisulfate may be readily derived from a Raman spectrum by computing the relative intensities of the 982/935 and 1052/935 cm^{-1} band pairs, respectively. Table 4.7 shows the derived intensities of the 935, 982 and 1052 bands. The concentrations of sulfate, bisulfate and protons as function of time and height from are plotted in Figure 4.13.

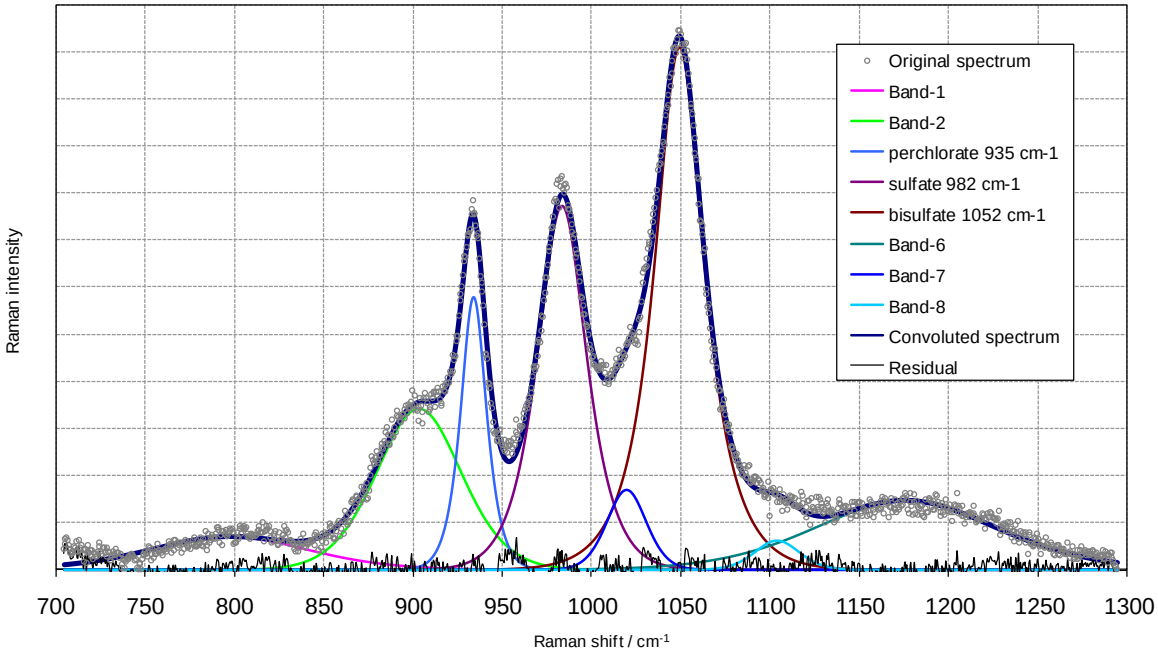

Figure 4.12. Raman spectrum at t = 213 h and z = 3 cm and band self-deconvolution

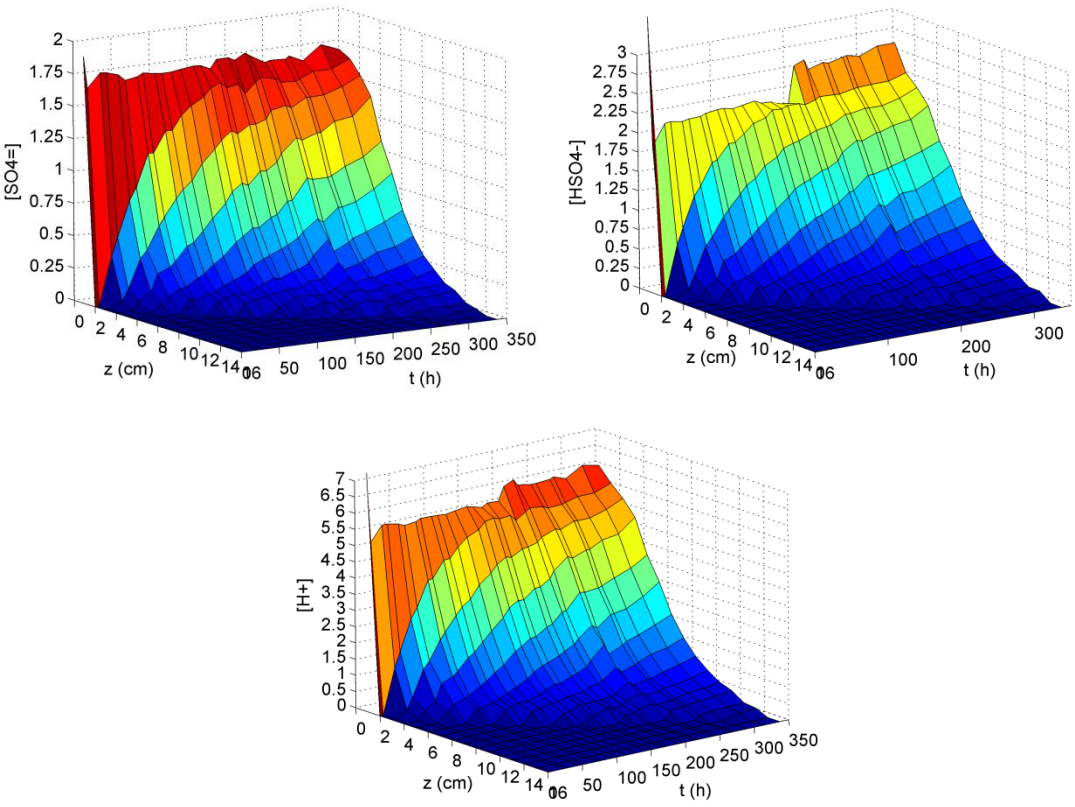

Figure 4.13. Concentrations of sulfate, bisulfate and proton as derived from the Raman spectral analysis plotted as a function of time and height. The concentration of protons has been derived from Eqn (4.12). Concentrations are in mol L^{-1}

4.4.4. Model optimization and discussion

Direct or indirect methods may be used to optimize the model shown in Eqn (4.15). Direct methods are preferred in this case as diffusion model includes a PDE. Indirect methods such as the Mean Least Squares imply the calculation of derivatives. This task becomes very complicated in models whose solution is obtained via numerical methods. In fact, the indirect methods could not even converge. We have therefore considered an optimization strategy based on the SIMPLEX direct method (Press *et al.* 1992) in order to solve our model. The method consists in creating a hyperspace with the parameters to optimize and the objective. The model is optimized trough geometric transformations within this space: reflections, contractions and extensions. The optimization of the model yields the values for the six adjusted parameters shown in Table 4.4 and the concentrations of the species that best fit those measured experimentally. Both calculated and measured sets of concentrations are plotted in Figure 4.14.

Table 4.4. Optimized parameters of the diffusion model

Parameter	Optimized Value
A	6.0243
B	0.0905
a	3.56E-05
b	1.09E-03
m	43.51
p	-0.412

The optimized values for the parameters *m* and *p* imply a linear behavior value of the function $H(c_w)$ in Eqn (4.17) as shown in Figure 4.15. In this circumstances, $D_w^{(c)}$ is also linear in c_w, and we can consider the parameters *m* and *p* to be rearranged within α and β. As a consequence, the diffusion model is optimized with four parameters instead of six. It is therefore likely that using six adjustable parameters in this particular diffusion model incurs in overfitting the model. Nonetheless, function shapes like $H(c_w)$ in Eqn (4.17) should not be discarded in the expression of $D_w^{(c)}$ because multicomponent mixtures containing more electrolytes may require the use of more

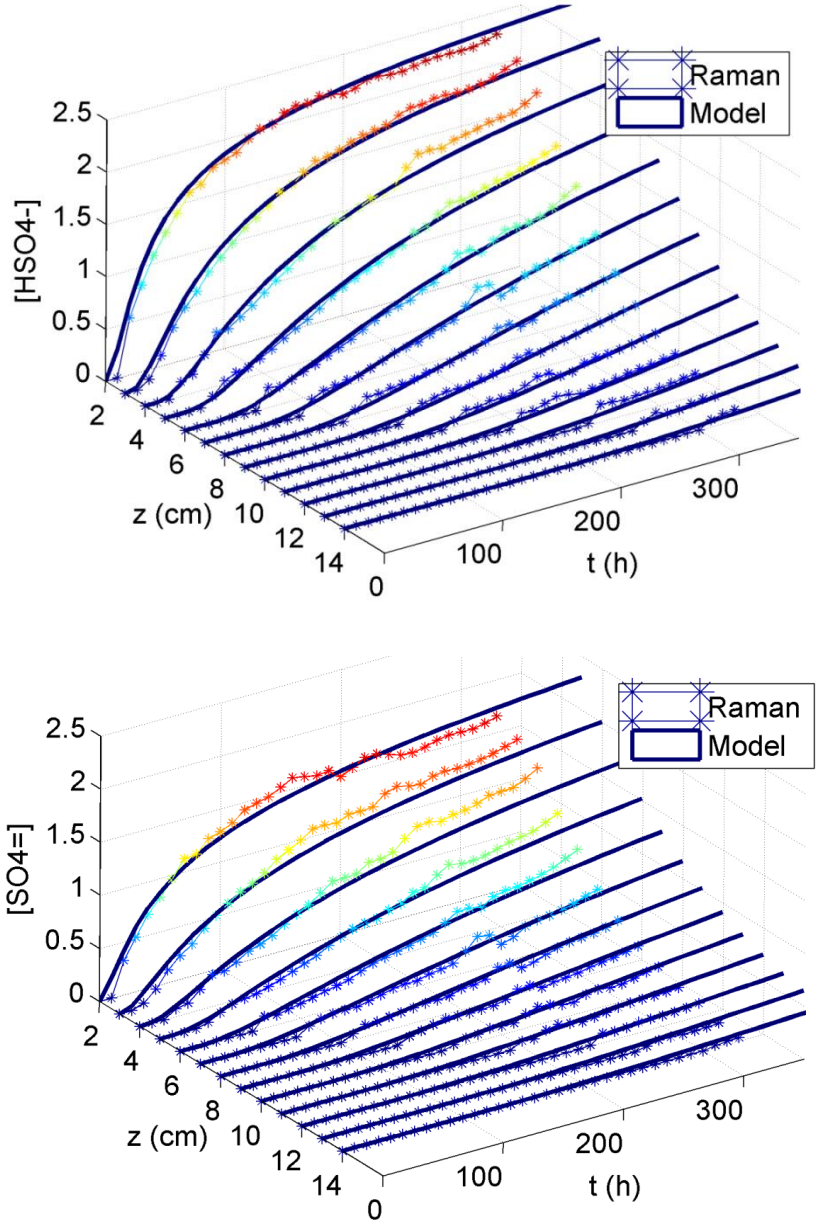

Figure 4.14. Experimentally and model-based derived concentrations of sulfate and bisulfate ions concentrations as functions of time and height. The optimized values for the parameters of the model are reported in Table 4.4

complex dependence of the diffusion coefficient with the concentration. We have proposed the function $H(c_w)$ because the performance of the diffusion coefficient may be derived from the Gibbs' formulation applied to processes in which the break of a finite potential barrier is involved (Lifshitz and Landau, 1980), as for instance the motion of molecules in liquids. Additionally, the function $H(c_w)$, in general terms, reproduces natural performances such as the neural response to stimulus (Wasserman, 1989), autocatalytic kinetics, etc.

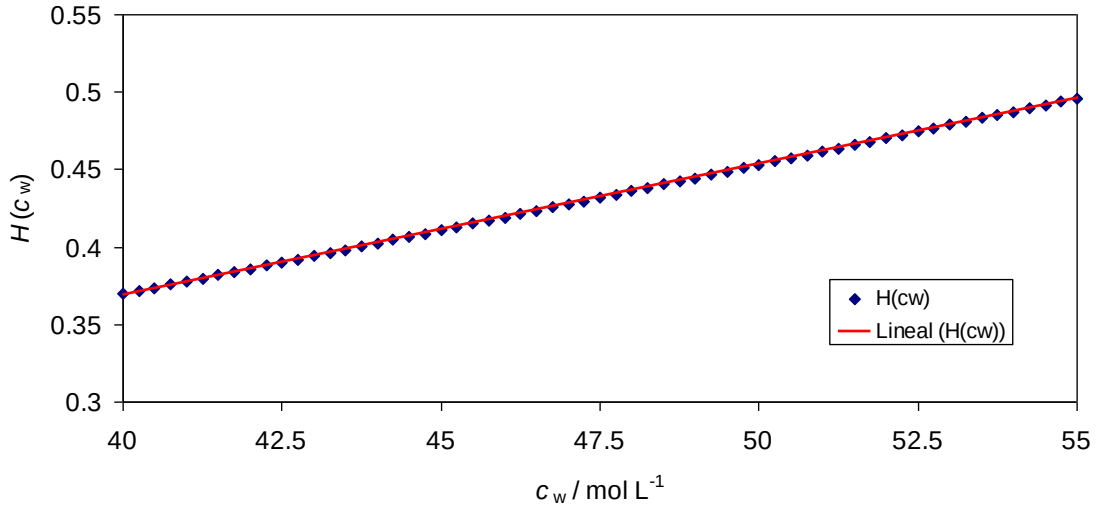

Figure 4.15. Values of the function $H(c_w)$ for the model parameters *m* and *p* reported in Table 4.4

The optimization of the parameters is performed simultaneously for the equilibrium relationship and the mass balance equations, yielding the set of parameters that best fits these equations to the experimental values. Occasionally, the simultaneous optimization could lead to unreal solutions, in part due again to the overfitting of the model. However, the optimized parameters derived for our model are consistent with previous independent investigations on the equilibriums of similar aqueous systems (*cf*. 4.2 and Sobron *et al.*, 2007b), and on the diffusion properties of the sulfuric acid-water system (Sobron, 2003; Sobron *et al.*, 2006).

Figure 4.16 shows the total concentration c_t as a function of time and height. As can be observed, the values are approximately constant for all times and heights, thus validating the hypothesis formulated in Eqn (4.14). This suggests that the diffusion coefficient in this equation gets close to its real value as a physical property. Starting here we could explain the physical/chemical meaning of the adjustable parameters in the proposed diffusion model in the context of a consistent thermodynamic model. This is not however a straightforward task and fall beyond the scope of this thesis.

The quality of the model optimization depends dramatically on the quality and reliability of the experimental data. Although the Raman technique provides the

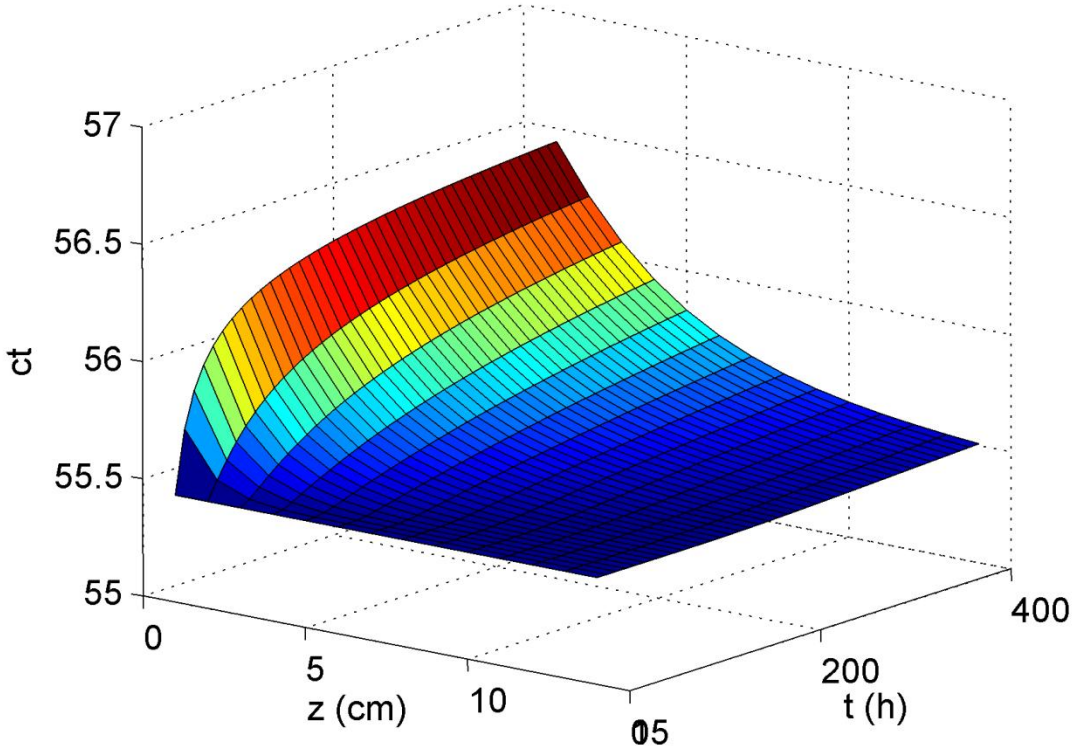

Figure 4.16. Total concentration as computed from the calculated values for the concentration of the electrolytes in solution

means to derive accurate concentrations of chemical species in solution, the characterization of the main bands in terms of intensity, width and shape is highly affected by the band overlapping as can be observed in Figure 4.12. A great overlapping of bands is unavoidable in the analysis of complex multicomponent systems such the one under study, and is the main source of errors in the development of physico-chemical models based on spectroscopic techniques.

Table 4.5. Intensity of the bands associated to the diffusing species measured as a function of time (h) and height (cm). Perchlorate, green; sulfate, blue; bisulfate, brown

time (h)	height (cm)													
	0	2	3	4	5	6	7	8	9	10	11	12	13	14
0	0.3010													
	0.5054													
	0.9700													
5	0.5249	0.8885	1.0351											
	0.7653	0.0000	0.0000											
	0.8916	0.0000	0.0000											
22	0.4991	0.9306	1.0101	0.9766										
	0.7749	0.3056	0.0470	0.0000										
	0.9673	0.5261	0.0922	0.0000										
30	0.4889	0.9545	1.0466	1.0443										
	0.7568	0.4295	0.1276	0.0639										
	0.9530	0.7162	0.2523	0.1295										
46	0.5065	0.8896	0.9481	1.0303	0.9884									
	0.7712	0.6147	0.3015	0.1183	0.0550									
	0.9756	0.9752	0.5300	0.2188	0.1397									

Table 4.5. (cont)

	0.5011	0.7769	1.0092	0.9535	0.9993			
55	0.7415	0.6018	0.3754	0.2219	0.1042			
	0.9726	0.9359	0.6595	0.3969	0.2130			
	0.4949	0.6643	0.9482	0.9776	1.0119	1.0179		
71	0.7396	0.6614	0.4977	0.2598	0.1426	0.1005		
	0.9629	0.9640	0.8243	0.4638	0.2506	0.1807		
	0.4924	0.6575	0.9657	0.9910	1.0264	1.0101		
78	0.7459	0.6523	0.5602	0.2960	0.1531	0.0840		
	0.9701	0.9684	0.9047	0.5239	0.2834	0.1600		
	0.4887	0.5856	0.8791	1.0079	1.0201	1.0298	1.0062	
94	0.7332	0.6622	0.6122	0.3960	0.2007	0.1160	0.0863	
	0.9722	0.9577	0.9611	0.6515	0.3760	0.2097	0.1526	
	0.4925	0.5654	0.7951	0.9881	1.0302	1.0249	1.0245	
103	0.7365	0.6403	0.5977	0.4096	0.2309	0.1266	0.1041	
	0.9800	0.9272	0.9405	0.7156	0.4391	0.2387	0.1724	
	0.4948	0.5287	0.7706	0.9846	1.0305	1.0358	1.0378	1.0054
115	0.7404	0.6476	0.6191	0.4751	0.2863	0.1629	0.1217	0.0820
	0.9731	0.9108	0.9599	0.7996	0.5039	0.2935	0.2056	0.1383

Table 4.5. (cont)

	0.4890	0.5245	0.7099	0.9590	0.9957	1.0382	1.0412	1.0053		
128	0.7368	0.6725	0.6452	0.5371	0.3208	0.1896	0.1159	0.0948		
	0.9717	0.9555	0.9731	0.8745	0.5626	0.3521	0.2168	0.1612		
	0.4846	0.5080	0.6667	0.9414	0.9735	1.0309	1.0264	0.9997	1.0335	
145	0.7357	0.6761	0.6643	0.6132	0.3990	0.2318	0.1518	0.1121	0.0629	
	0.9744	0.9459	0.9661	0.9677	0.6730	0.4297	0.2744	0.1901	0.1162	
	0.4931	0.4901	0.6230	0.8546	0.9692	0.9322	1.0317	1.0218	1.0323	1.0000
154	0.7469	0.6801	0.6556	0.6194	0.4293	0.2512	0.1712	0.1200	0.0719	0.0000
	0.9723	0.9495	0.9583	0.9480	0.7027	0.4366	0.3089	0.1959	0.1345	0.0000
	0.4955	0.4890	0.6001	0.8321	0.9758	1.0161	1.0152	1.0257	0.9855	1.0188
167	0.7354	0.6904	0.6646	0.6441	0.4800	0.3070	0.1992	0.1382	0.1091	0.0538
	0.9736	0.9441	0.9464	0.9678	0.7773	0.5395	0.3506	0.2318	0.1653	0.1156
	0.4975	0.4234	0.5915	0.7968	0.9835	1.0330	1.0326	1.0195	1.0201	1.0210
175	0.7677	0.5808	0.6394	0.6000	0.4803	0.3318	0.1926	0.1408	0.1123	0.0501
	0.9631	0.8290	0.9412	0.9458	0.8056	0.5768	0.3601	0.2388	0.1758	0.1130
	0.5138	0.4783	0.5672	0.7571	0.9840	1.0257	1.0294	1.0249	1.0075	1.0153
191	0.7933	0.6624	0.6431	0.6356	0.5381	0.3645	0.2291	0.1463	0.1045	0.0819
	0.9831	0.9349	0.9365	0.9582	0.8789	0.6136	0.4186	0.2708	0.1781	0.1438

Table 4.5. (cont.)

199	0.3995	0.4817	0.5709	0.7589	0.9954	1.0067	1.0426	1.0338	1.0282	1.0358	1.0298	
	0.6080	0.6333	0.6457	0.6345	0.5588	0.3777	0.2418	0.1774	0.1096	0.0730	0.0488	
	0.9342	0.9299	0.9574	0.9708	0.9233	0.6529	0.4516	0.3000	0.2032	0.1413	0.1061	
213	0.3924	0.4850	0.5555	0.7112	0.9116	0.9931	1.0081	1.0222	1.0110	1.0237	1.0330	
	0.6127	0.6714	0.6424	0.6308	0.5861	0.4128	0.2690	0.1811	0.1115	0.0781	0.0432	
	0.9365	0.9536	0.9433	0.9557	0.9373	0.6981	0.4882	0.3281	0.2192	0.1623	0.1085	
219	0.4091	0.4700	0.5495	0.6485	0.9047	0.9631	0.9395	1.0104	1.0073	1.0094	1.0146	
	0.6299	0.6647	0.6654	0.6108	0.5828	0.4350	0.2956	0.1930	0.1278	0.1126	0.0802	
	0.9275	0.9371	0.9383	0.9294	0.9349	0.7324	0.5121	0.3588	0.2342	0.1839	0.1363	
239	0.4065	0.4781	0.5199	0.5973	0.7261	0.9047	0.8800	0.9423	0.9902	0.9487	0.9460	
	0.6014	0.6652	0.6408	0.6187	0.5686	0.4795	0.3627	0.2632	0.1968	0.1332	0.0839	
	0.9417	0.9494	0.9373	0.9225	0.8596	0.8088	0.6177	0.4329	0.3096	0.2300	0.1552	
246	0.4053	0.4719	0.5090	0.5954	0.7805	0.9719	1.0008	1.0429	0.5300	1.0299	1.0354	1.0315
	0.6042	0.6434	0.6165	0.6032	0.6002	0.4859	0.3236	0.2337	0.0834	0.1210	0.0766	0.0640
	0.9307	0.9349	0.9165	0.9081	0.9231	0.8196	0.5952	0.4298	0.1536	0.2082	0.1464	0.1183
266	0.4055	0.4744	0.5146	0.5938	0.7814	0.9164	0.9912	1.0069	1.0283	1.0250	1.0560	0.9943
	0.6022	0.6429	0.6541	0.6233	0.6016	0.5412	0.3708	0.2532	0.1821	0.1227	0.0930	0.0620
	0.9475	0.9558	0.9426	0.9445	0.9543	0.8766	0.6532	0.4724	0.3383	0.2274	0.1756	0.1297

Table 4.5. (cont.)

	0.4007	0.4720	0.5071	0.5924	0.7590	0.8851	0.9681	1.0254	0.9676	1.0456	1.0475	1.0264	1.0274	
271	0.6023	0.6460	0.6430	0.6215	0.5905	0.5199	0.3832	0.2733	0.1697	0.1510	0.0968	0.0768	0.0250	
	0.9405	0.9538	0.9268	0.9429	0.9401	0.8609	0.6731	0.5079	0.3265	0.2570	0.1795	0.1371	0.0709	
	0.4002	0.4668	0.5144	0.5835	0.7460	0.9370	0.9814	0.9972	1.0156	1.0346	1.0496	1.0170	1.0285	
289	0.5839	0.6576	0.6536	0.6494	0.6184	0.5730	0.4207	0.3101	0.2091	0.1466	0.1249	0.0904	0.0406	
	0.9252	0.9463	0.9387	0.9574	0.9569	0.9170	0.7216	0.5439	0.3826	0.2735	0.2112	0.1490	0.0729	
	0.3975	0.4620	0.4992	0.5697	0.6893	0.8650	0.9897	0.9924	0.9957	1.0230	1.0094	1.0337	1.0134	1.0052
313	0.6172	0.6506	0.6550	0.6448	0.6050	0.5897	0.4762	0.3312	0.2357	0.1736	0.1219	0.0952	0.0382	0.0221
	0.9513	0.9371	0.9369	0.9541	0.9322	0.9291	0.7974	0.5796	0.4253	0.3061	0.2297	0.1750	0.1044	0.0698
	0.3866	0.4482	0.4678	0.5163	0.6639	0.7926	0.9686	0.9861	1.0144	1.0166	1.0259	1.0332	1.0379	1.0444
337	0.5816	0.6562	0.6417	0.6452	0.6434	0.6127	0.5265	0.3833	0.2817	0.2095	0.1402	0.1112	0.0494	0.0287
	0.9254	0.9368	0.9184	0.9283	0.9519	0.9475	0.8477	0.6434	0.4783	0.3401	0.2665	0.2009	0.1004	0.1003

4.5. Raman spectroscopy of Rio Tinto stream waters

4.5.1. Abstract

Acidic waters and sulfate-rich precipitates are found in mine tailings such as Rio Tinto. In this work we have characterized the chemical constituents of stream water by means of Raman spectroscopy. Variable amounts of sulfate and bisulfate are found in the aqueous samples, suggesting changes in the acidity of the solutions. An estimation of the sulfate/water relative abundance is also given. These results are consistent with previous works reporting the water composition of acid mine drainage related sites, and proves the importance of Raman spectroscopy as a tool for accurate and noninvasive analyses of acid waters.

4.5.2. Experimental

4.5.2.1. Sampling

Surface and stream water samples from acid mine effluents were collected from several spots in Rio Tinto area. A map illustrating all collection sites is presented in Figure 4.17. Water samples and its associate efflorescences and precipitates were collected close to Peña de Hierro, from one of the branches considered as one of the river's true sources.

4.5.2.2. Raman spectroscopy

Raman spectra of the aqueous samples were collected at a constant temperature of 20 °C with a confocal Raman microscope (WiTec alpha300 R (*cf*. 2.3.)) in the spectral range 75-3900 cm^{-1}. The spectral resolution was 1 cm^{-1}. The 532.4 nm line of a frequency doubled Nd:YAG laser was used as the excitation source.

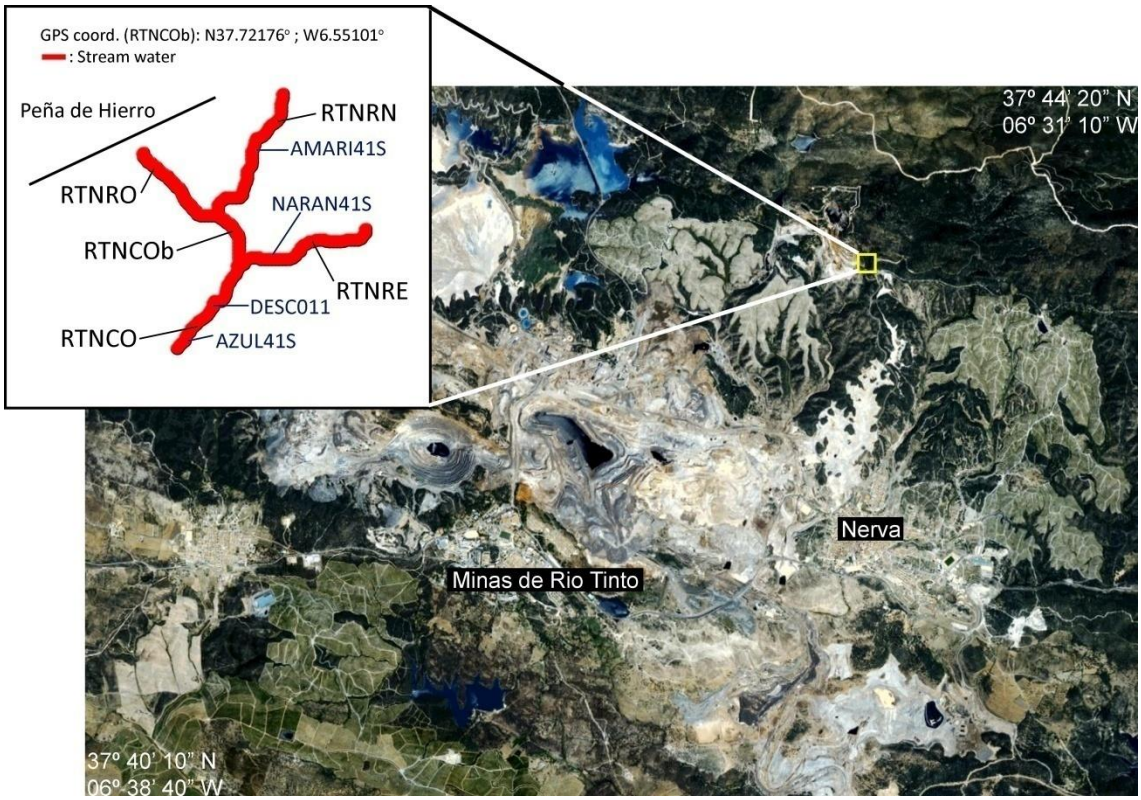

Figure 4.17. Map of the Rio Tinto mining area with enlarged sketch of the sampling spots

4.5.3. Results and discussion

The Raman spectra of five selected aqueous samples in the region 800-1900 cm^{-1} are displayed in Figure 4.18 and the results of the Raman spectral analysis are reported in Table 4.8. This wavenumbers region is of particular interest for the study of sulfates in aqueous solutions since both sulfate/bisulfate stretching bands and water bending modes are observed simultaneously. Bands at 981 and 1105 cm^{-1} are ascribed to v_1 and v_3 symmetric stretching of sulfate, respectively. The bands around 1250 and 1140 cm^{-1} are related to the sulfate and bisulfate asymmetric stretching modes, respectively (*cf*. 2.2). The symmetric stretching of bisulfate gives rise to a band at 105 cm^{-1} with a shoulder at 1040 cm^{-1}. Shoulders at 1005 and 1040 cm^{-1} are associated with distortions in the sulfate and bisulfate structural units by iron(III) direct complexation. Water bending modes display a band around 1640 cm^{-1}.

For the RTNCOb_001 sample six bands are observed at 982, 1006, 1045, 1140, 1212, and 1640 cm^{-1}. It is evident that the sample contains sulfate and bisulfate units

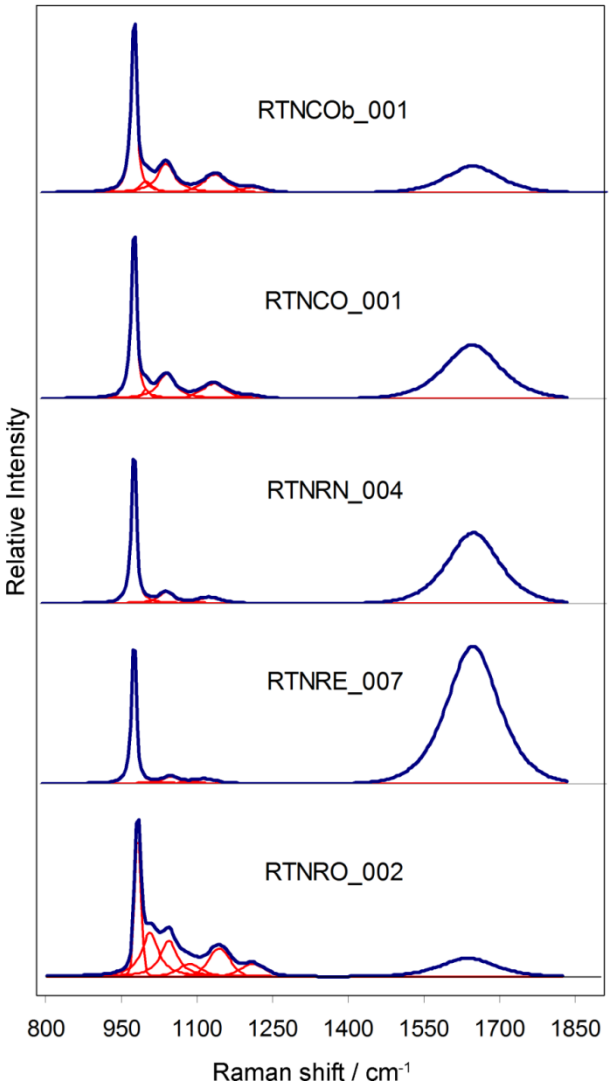

Figure 4.18. Raman spectra of samples RTNRO_002, RTNRE_007, RTNRN_004, RTNCO_001 and RTNCOb_001 in the region 800-1900 cm^{-1}

in equilibrium with water. The intensity of a band in the Raman spectrum is a function of the concentration of its associated species. The relative intensities of sulfate, bisulfate and water are reported in Table 4.9. The relative intensities of the sulfate (982 cm^{-1}), bisulfate (1044 cm^{-1}) and water (1640 cm^{-1}) main bands are 6.25:1.13:1. For the RTNCO_001 sample the six bands are found at 982, 1006, 1046, 1138, 1206 and 1639 with relative intensities 2.94:0.44:1 for the main bands.

The relative concentration of water is greater for the RTNCO_001 sample. This is consistent with the difference in color and transparency between both samples (Figure 4.19). Four bands are observed for the RTNRN_004 at 982, 1046, 1129 and 1641 cm^{-1}.

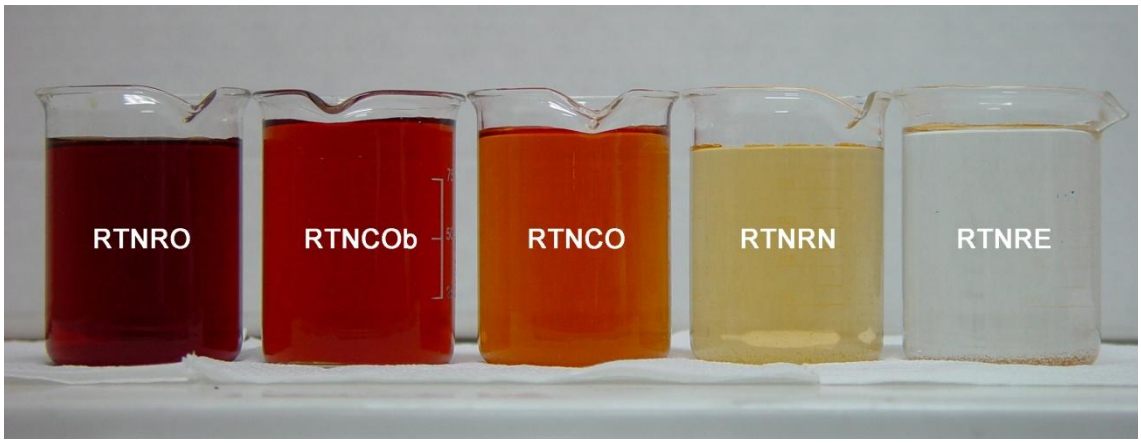

Figure 4.19. Pictures of the samples displaying different colors as compositions varies

The intensities of the 982 and 1046 cm^{-1} bands relative to that of water at 1641 cm^{-1} are 2.04:0.16:1. The bands at 1006 and 1206 cm^{-1} are hidden by broader bands and the relative intensity of the water increases in comparison to the previous samples. The same effect is observed for the RTNRE_007 sample, with bands at 982, 1054, 1120 and 1640 cm^{-1} and relative intensities 0.97:0.05:1. In this case the relative abundance of water is slightly greater than that of sulfate ion. The RTNRO_002 shows a spectrum with seven bands at 982, 1007, 1044, 1086, 1144, 1210 and 1636 cm^{-1}. The relative intensities are in this case 11.11:3:1. The small value of the intensity in the water band indicates a more concentrated solution, which is consistent with the dark-red color of the sample, likely due to the presence of iron in solution.

Table 4.6. Results of the Raman spectra of the stream water samples from Rio Tinto

RTNCOb_001			RTNCO_001			RNTRN_004			RTNRE_007			RTNRO_002		
Position	Intensity[a]	HWHM[b]	Position	Intensity	HWHM	Position	Intensity	HWHM	Position	Intensity	HWHM	Position	Intensity	HWHM
982.5	1	5.80568	982.436	1	5.49105	982.306	1	5.04513	982.32	0.96671	4.78615	982.358	1	7.04028
1006.44	0.07186	12.9616	1006.17	0.05547	8.06058	1006.17	0	8.06058	1011.17	0	30	1006.81	0.32888	20.0011
1044.74	0.1789	20	1045.56	0.15282	20	1045.71	0.07812	17.6123	1053.64	0.05269	20	1044.18	0.26957	20
1140.05	0.11116	30	1137.96	0.09483	30	1128.96	0.04039	30	1120.04	0.03309	29.1916	1085.57	0.0948	30
1211.64	0.03277	30	1206.32	0.02171	27.0915	1206.32	0	27.0915	1194.32	0	30	1144.28	0.20819	30
1640.35	0.16375	66.1542	1639.29	0.33957	69.0865	1641.44	0.4937	64.1127	1640.44	1	64.4467	1210.34	0.0982	30
												1636.44	0.13806	70

[a] Normalized band intensities

[b] Half width at half maximum

Table 4.7. Relative intensities of sulfate, bisulfate and water bands measured from the Raman spectra of the stream waters from Rio Tinto

	Band relative intensity		
Sample	982 cm^{-1}	1044 cm^{-1}	1640 cm^{-1}
RTNCOb	6.25	1.13	1.00
RTNCO	2.94	0.44	1.00
RTNRN	2.04	0.16	1.00
RTNRE	0.97	0.05	1.00
RTNRO	11.11	3	1.00

Chapter 5

mineralogy associated to acidic sulfate waters

This chapter deals with the investigations of natural sulfate samples. The Raman spectroscopy of sulfate precipitates and efflorescent sulfate salts from Rio Tinto and from the Richmond Mine in Iron Mountain, California, another AMD related site, is presented. Additionally, we report a combined Raman/Reflectance/X-ray Diffraction study on Rio Tinto samples.

5.1. Overview

In the following sections we present:

i. The Raman microspectroscopy of natural sulfate efflorescences from the Richmond Mine at Iron Mountain, California. Gypsum, ferricopiapite, copiapite, melanterite, coquimbite, and voltaite were found in the samples.

ii. The Raman microspectroscopy of sulfate precipitates and efflorescences of Rio Tinto. Mine tailings such as the site under study contain large amounts of sulfur-rich mineral and are characterized by highly acidic waters. As such, spectral fingerprints from various forms of iron sulfates were found in those minerals and used for their identification.

iii. A characterization of some evaporitic salts from Rio Tinto by means of Raman spectroscopy, VNIR reflectance spectroscopy and X-ray diffraction (XRD). The combination of these techniques proves to be extremely useful for the detection of the different minerals phases present in the samples.

5.2. Raman spectroscopy of efflorescent sulfate salts from Iron Mountain Superfund Site, California.

5.2.1. Introduction to the Iron Mountain Mine

Iron Mountain, California is the host of massive sulfide deposits that were mined for copper, zinc, gold, silver, and pyrite (for sulfuric acid) between the early 1860s and the early 1960s. The mines at Iron Mountain represent the largest within the West Shasta mining district of northern California (Kinkel *et al.*, 1956). The sulfide deposits at Iron Mountain occur as tabular masses with >95% sulfide. The deposits are pyrite-rich, with copper and zinc occurring primarily as chalcopyrite and sphalerite, respectively. The host rocks in the Iron Mountain area include the Balaklala rhyolite, a felsic volcanic rock that has been hydrothermally altered to contain the minerals illite (sericite), chlorite, and albite as well as residual quartz, and the Copley Greenstone, a meta-andesite.

The Richmond Mine at Iron Mountain was actively mined for copper and zinc by underground methods between the 1920s and 1950s. The Richmond Mine is notorious for having extremely acidic mine drainage: the water leaving the Richmond Adit has a pH around 0.5 and extremely elevated concentrations of sulfate, iron, and other metals (Alpers *et al.*, 2003). As part of its Superfund remediation program, the U.S. Environmental Protection Agency renovated a portion of the underground workings of the Richmond Mine during 1988-1990, which allowed access for sampling of water and efflorescent sulfate minerals. This reconnaissance sampling resulted in characterization of the extremely acidic mine waters (pH values from -3.6 to +0.5) and a variety of iron-sulfate efflorescent salts (Nordstrom and Alpers, 1999b; Nordstrom *et al.*, 2000).

The study of sulfate-rich efflorescences is important for understanding the liquid-solid phase-equilibriums in sites contaminated by acid mine drainage; such understanding may lead to the development of remediation strategies and may allow for an early detection of acid mine drainage contamination. In this work we report the

Raman spectra of efflorescent sulfate salts from the Richmond Mine at Iron Mountain, California. Coquimbite, melanterite, gypsum, copiapite and voltaite have been identified within the samples.

5.2.2. Experimental

5.2.2.1. Sampling

Mineral samples analyzed in this study were collected from the Richmond mine at Iron Mountain during 1990-92. Specific sites of sample collection were in the B and C drifts on the 2600 level, in the B'stope on the 2650 level, and in the E mainway, which connects the 2600 and 2650 levels along the C drift (Figure 5.1). Ambient temperatures in the mine workings were 35 to 47 °C. Mineral samples were preserved in acid-washed glass jars with Teflon-lined lids. Parafilm was used to provide additional sealing of the lids. The samples were stored in a warehouse in Sacramento, California where temperature fluctuated between about 15 and 35 °C.

5.2.2.2. Raman spectroscopy

The samples were placed on the 3D-motion stage of a confocal Raman microscope (WiTec alpha300 R (*cf*. 2.3)). Raman spectra were collected at a constant temperature of 293 K in the spectral range 100-3900 cm^{-1}. The spectral resolution was 4 cm^{-1}. The 532.4 nm line of a frequency doubled Nd:YAG laser was used as the excitation source. The Raman spectra were filtered and baseline corrected using improved FFT algorithms. Routines based on the Marquardt method are used to analyze the spectra in terms of band position, intensity, width and Gaussian-Lorentzian (G-L) factor (see chapter 3).

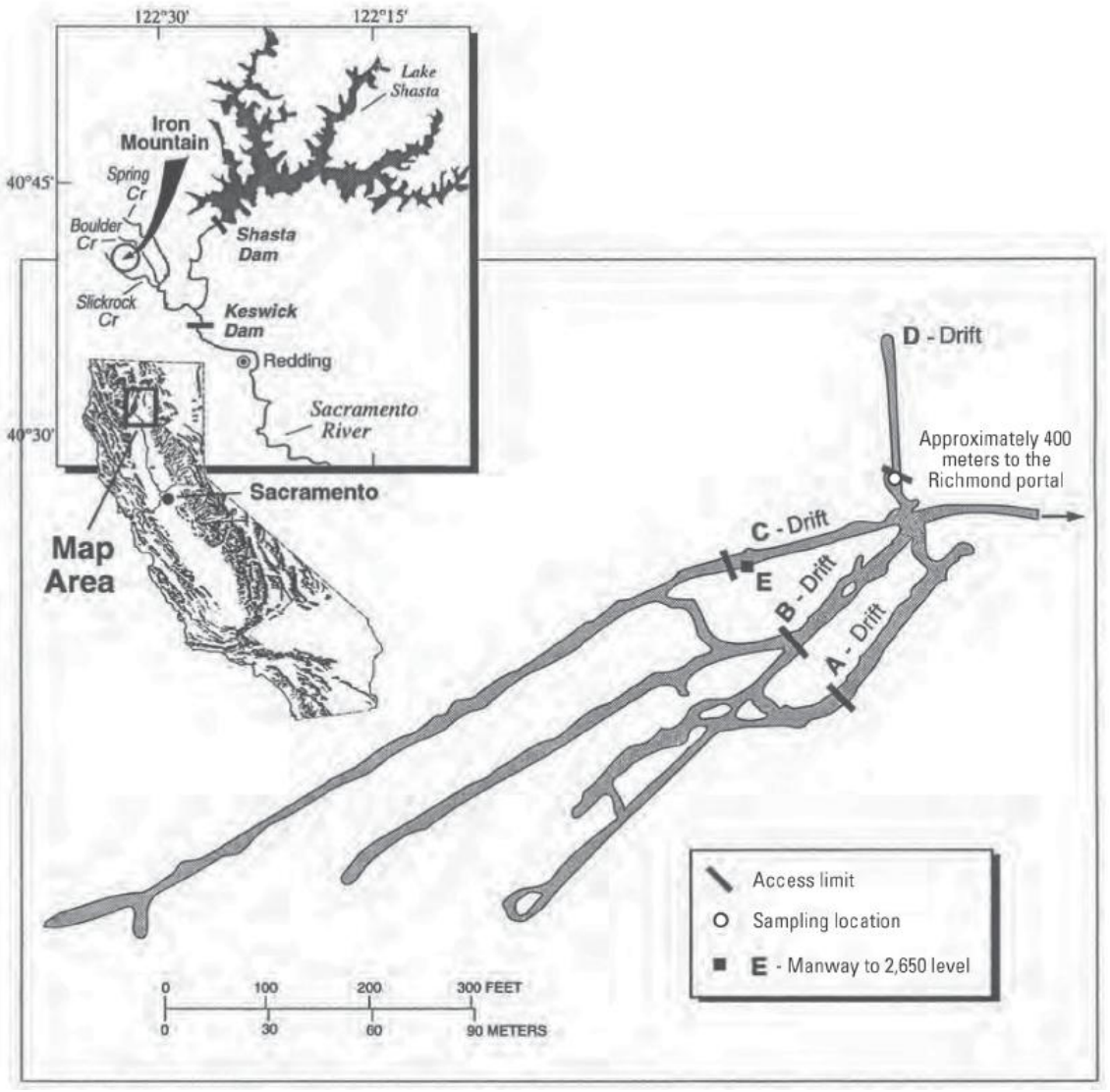

Figure 5.1. Location and plan map of the underground workings, 2,600 level, Richmond mine, Iron Mountain, California. (Figure from Jamieson *et al.*, 2005)

5.2.3. Results and discussion

Raman spectra of sulfate-bearing minerals are mainly populated with bands arising from sulfate molecular vibrations. In their work about synthetic jarosites, Sasaki *et al.* (1998) assigned the band at 434 cm^{-1} to the Fe-O stretching vibration. However, this assignment was rebated by Frost *et al.* (2005), who attributed the band to the v_2 mode of sulfate. Previous findings by the authors (section 4.3 and Sobron *et al.* 2007a) are in good agreement with that of Frost *et al.* (2005), and state that the Fe-O stretching vibrations characteristic of iron(III) hydroxides give rise to a set of bands around 300 cm^{-1}. Such band assignment is considered in this work.

A split of the sulfate vibrational modes into separate bands is observed in the crystal structures, and is due to symmetry breakdown (*cf*. 2.2). Figure 5.2 shows the Raman spectra of the samples in the low-wavenumbers region (100-750 cm^{-1}) and the results of the Raman spectral analysis are reported in Table 5.1. All the spectra show two sets of bands centered around 450 and 600 cm^{-1}, arising from the v_2 and v_4 vibrational modes of the sulfate tetrahedral oxyanions, respectively. Three sharp bands are observed for: 91RS201Bb at 400, 440 and 467 cm^{-1}; 91RS204DriftA_Cb at 412, 458 and 480 cm^{-1}. Four bands are observed for: 91RS204A2 at 400, 434, 460 and 487 cm^{-1}. The fact that multiple bands are observed in the v_2 region of these sulfates indicates certain symmetry breakdown of sulfate tetrahedra, probably through the presence of different sulfates in the structures. On the other hand, two intense bands are observed for: 91RS201Ba at 429 and 475 cm^{-1}; 91RS204D3 at 457 and 471 cm^{-1}; 91RS204DriftA_Ca at 417 and 496 cm^{-1}. It is apparent that the site symmetry is better preserved in these samples. Finally, a single sharp band is observed for: 91RS118 at 451 cm^{-1}; 91RS201Bc at 508 cm^{-1}. The sulfate group in these two samples could have higher site symmetry in comparison to the other samples, thus suggesting the present of a unique M-SO_4 group in the structure, where M denotes a cation. The shoulder near 380 cm^{-1} observed in samples 91RS118 and 91RS201Bb is attributed to a vibration of the $[Fe(H_2O)_6]^{2+}$ complex (section 4.2; Hester and Plane, 1964; Sobron *et al.* 2007b). Samples 91RS201Bc, 91RS204A2 and 91RS204DriftA_Cb show intense bands at around 310 cm^{-1}. As discussed above they are attributed to Fe-O stretching vibrations associated to iron(III). Particularly, this band may arise from Fe-hydroxyl group interactions. Weak bands are observed at around 350 cm^{-1} for samples 91RS201Bb, 91RS201Bc, and 91RS202D3. Those may be assigned to Fe-O stretching modes as well.

Likewise, the v_4 vibrational modes of sulfate give rise to multiple bands in the Raman spectra centered upon 600 cm^{-1}, which can be explained, as for the v_2 region, in terms of lowering of symmetry in the sulfate structures. And intense band is observed at between 207 and 221 cm^{-1} in the Raman spectra of those samples showing bands at around 310 cm^{-1}. Those bands are also believed to be originated from Fe-O vibration modes. A complex set of bands at between 160 and 290 cm^{-1} visible in all the spectra may be assigned to M-O stretching vibrations.

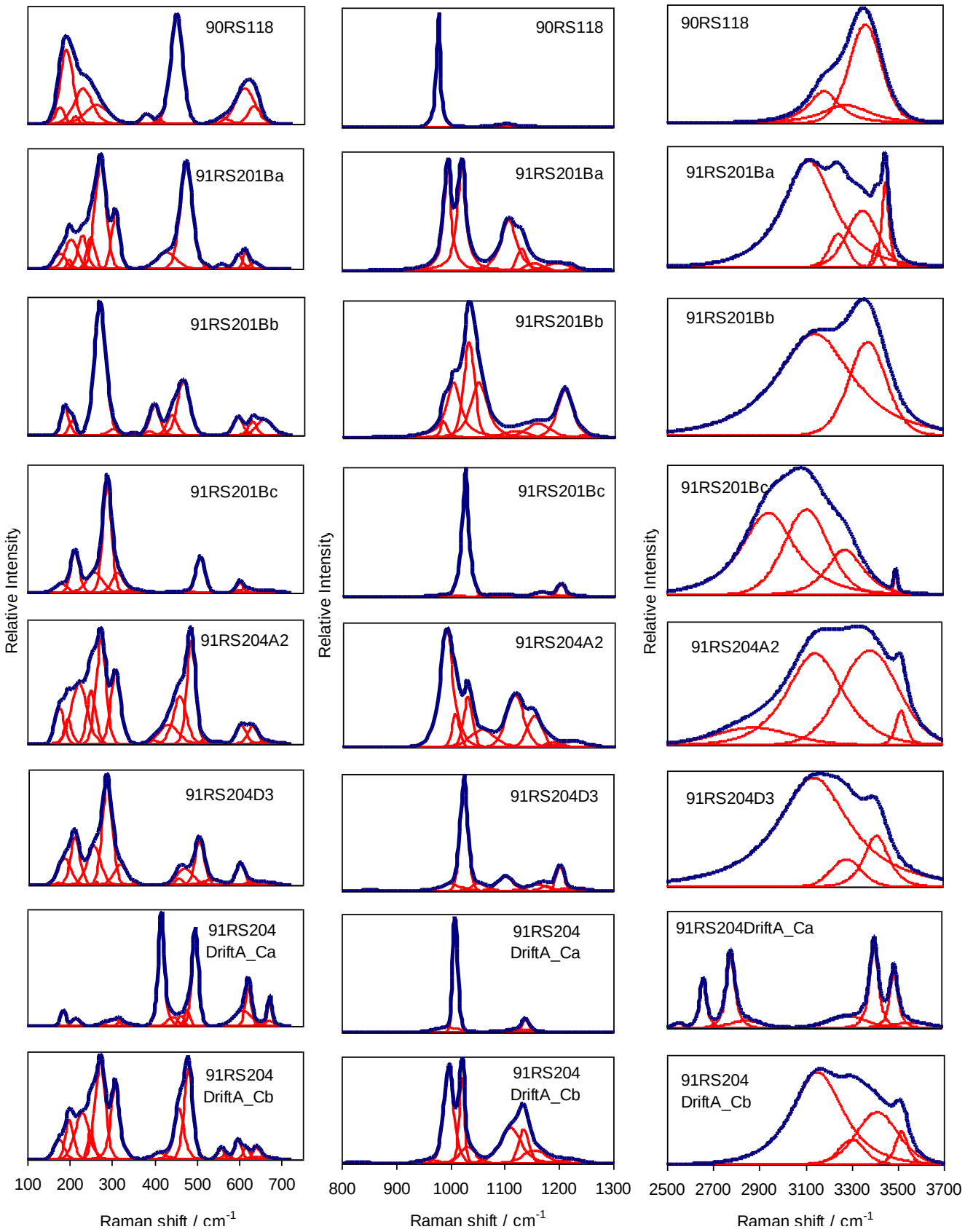

Figure 5.2. Raman spectra of the selected samples from the Iron Mountain Mine in the three regions of interest

Band splitting of the sulfate v_1 and v_3 vibrational modes is observed in the region 800-1300 cm^{-1} for all the Raman spectra. The two sets of bands between 978 and 1076 cm^{-1} and between 1100 and 1250 cm^{-1} are assigned to the v_1 and v_3 sulfate modes, respectively. The Raman shift of the v_1 sulfate stretching mode depends on the ionic radius of the cation bonded to the sulfate ion (Sasaki *et al.* 1998; Chio *et al.*, 2005; Frost *et al.* 2005). The spectra of samples 90RS118, 91RS201Bc, 91RS204D3 and 91RS204DriftA_Ca show a single intense band for the v_1 sulfate mode at 978, 1026, 1026 and 1010 cm^{-1}, respectively. In accordance with Ross (1974) the low-intensity shoulders found around 850 cm^{-1} are assigned to water librational modes. Other shoulders in both sides of the most intense band and the series of low-intensity bands in the v_3 sulfate region in the spectra of samples 91RS201Bc and 91RS204D3 may be likely associated with distortions of the sulfate ion by hydrogen bonding and iron(III) direct complexation (section 4.3. and Sobron *et al.*, 2007a). Chio *et al.* (2005) observed an upshift (977 to 1018 cm^{-1}) of the sulfate v_1 band position in the Raman spectra of various hydrated iron(II) sulfates as hydration, and therefore site symmetry, decreases. The larger band position-shift (982 to 1026 cm^{-1}) we observe for samples 91RS201Bc and 91RS204D3 may be explained if iron(III) is attached to the sulfate groups. The inclusion of oxygens from sulfate units in iron(III) octahedra leads to a strong charge delocalization, hence a loss of symmetry in the sulfate tetrahedral structures. The loss of symmetry is reflected in the Raman spectrum by a shift in the position of the S-O symmetric stretching band towards higher wavenumbers. A typical hydrated iron(III) sulfate found in AMD related sites is coquimbite, $(Fe^{3+})_2(SO_4)_3 \cdot 9H_2O$, which often exhibits purple crystals. The purple color of both 91RS201Bc and 91RS204D3 suggests the presence of coquimbite. However, sample 91RS201Bc shows not just purple crystals but white/yellowish incrustations in the spotted area. This may be the reason why, even though the spectra look similar in the low and mid wavenumbers region, differences in the relative intensities of some of the bands in both regions are observed. Other possible explanation to the intensities difference may be attributed to differences in crystal orientation.

The band position of the v_1 (single line) and v_3 (doublet) stretching modes for sample 90RS118 is in excellent agreement with the Raman spectrum of melanterite

($FeSO_4 \cdot 7H_20$) reported by Chio *et al.* (2005). Further, the blue color of the sample is consistent with the presence of melanterite. The Raman spectra of sample 91RS204DriftA_Ca resembles that of gypsum ($CaSO_4 \cdot 2H_20$) reported by Dickinson and Dillon (1929). Also the color and texture of the sample (white) is consistent with its identification as gypsum.

The observation of multiple bands in the ν_1 and ν_3 sulfate vibration region confirms the previous suggestion of the presence of different cations associated to sulfate groups in the samples 91RS201Ba, 91RS201Bb, 91RS204A2, and 91RS204DriftA_Cb. Samples 91RS204A2, 91RS201Ba, and 91RS204DriftA_Cb show a similar envelope. Two pairs of intense bands are observed for sample 91RS201Ba at 995/1108 cm^{-1} and 1021/1132 cm^{-1}. Sample 91RS204DriftA_Cb shows the same pairs at 998/1113 cm^{-1} and 1021/1126 cm^{-1}. They arise from two different types of sulfates in the structure of the samples. The band positions suggest that the first pairs arise from the presence of iron(II) sulfate (Chio *et al.*, 2005), whereas the second pairs are due to the presence of iron(III) sulfate (see above discussion) in the samples. The existence of iron(II)/iron(III) sulfates is likely in an environment such as the one under study since iron(II) may be easily oxidized into iron(III) in presence of water and oxygen (López-Archilla *et al.*, 2001).

However, two broad bands, centered at 961 and 1035 cm^{-1}, are needed in the band analysis of sample 91RS204DriftA_Cb. They are due likely to hydrogen bonding among iron(III) octahedra. The relative intensity of the two bands at 1113 and 1136 cm^{-1} is 1.1:1 for this sample. The relative intensity for the equivalent bands (1108 and 1126 cm^{-1}) in sample 91RS201Ba is twice as much, 2.2:1. We suggest that these two differences in the Raman spectra of samples 91RS201Ba and 91RS204DriftA_Cb are due to distinct relative abundance of iron(II)/iron(III) sulfate. Both sample display yellow color. It is likely that copiapite, $Fe^{2+}(Fe^{3+})_4(SO_4)_6(OH)_2 \cdot 20H_2O$, is present in sample 91RS201Ba, whereas ferricopiapite, $(Fe^{3+})_{2/3}(Fe^{3+})_4(SO_4)_6(OH)_2 \cdot 20H_2O$ is the main mineral phase in sample 91RS204DriftA_Cb. The presence of iron(III) in two different symmetry sites may explain the split of the ν_1 and ν_3 vibrational modes of sulfate in two pairs in the Raman spectrum of this sample.

The Raman spectrum of sample 91RS201Bb displays a complex set of bands around 1020 and 1200 cm^{-1}. The difficulty of performing accurate band analysis of closely overlapped bands is exemplified by this spectrum. It is evident the presence of various sulfates in the sample. The analyzed spots showed black/dark blue prismatic crystals, which are consistent with voltaite, $K_2(Fe^{2+})_5(Fe^{3+})_3Al(SO_4)_{12}\cdot 18H_2O$. The presence of four different cations is also consistent with the series of overlapping bands in the v_1 sulfate region.

Figure 5.2 shows the Raman spectra in the region 2500-3700 cm^{-1} as well. OH stretching bands of the water units are found in this region. They generally overlap those arising from the hydroxyl stretching vibrations of the OH group. Particularly, the sharp band centered between 3525 and 3576 cm^{-1} in the Raman spectra of samples 91RS201Ba, 91RS204A2, and 91RS204DriftA_Cb is attributed to M-OH stretching vibrations of the hydroxyl units. This is consistent with the identification of the samples as copiapite, copiapite, and ferricopiapite, respectively. These minerals contain both water and OH units. A sharp but low-intensity band is observed at 3581 cm^{-1} for sample 91RS201Bc. This band is also attributable to M-OH vibrations, although no hydroxyl groups are present in coquimbite. The broad and complex series of bands around 3200 cm^{-1} is characteristic of water, and as can be readily observed, it shows a different envelope than that of sample 91RS204D3 (more clearly identified as coquimbite). This deformation of the spectra in the water region may be caused by the presence of different hydrated spheres associated to different cations as well as iron(III). It is suggested that the sample 91RS201Bc contains coquimbite along with a small amount of some iron hydroxides, most likely copiapite, since both compounds are usually found in association in metal-sulfide mineral deposits (Nordstrom and Alpers, 1999a). Hydrated iron sulfates such as melanterite in sample 90RS118 and voltaite in sample 91RS201Bb display the characteristic set of broad water bands. The shape of the broad continuum is mainly determined by the hydration number, which defines the number of bridging water molecules (Chio *et al.*, 2005).

The mineral composition of the samples is summarized in Table 5.

Table 5.1. Results of the Raman spectral analysis of the natural sulfates from Iron Mountain Mine

90RS118			91RS201Ba			91RS201Bb			91RS201Bc			91RS204A2		
Position	Intensity[a]	HWHM[b]	Position	Intensity	HWHM	Position	Intensity	HWHM	Position	Intensity	HWHM	Position	Intensity	HWHM
177.0	1.171	13.8	177.1	1.017	18.0	188.6	2.512	12.2	180.2	1.193	18.9	176.2	1.897	14.5
192.6	5.102	20.2	199.9	0.673	8.0	206.6	1.365	10.8	213.0	5.163	13.2	196.5	1.345	11.6
213.3	0.560	9.0	203.8	1.968	20.0	271.0	11.652	17.9	258.4	2.570	25.2	222.4	3.172	24.7
231.6	2.408	28.7	230.4	2232	15.0	302.0	0.536	16.0	288.5	13.696	13.9	251.6	2.839	13.5
249.0	0.049	20.2	250.5	2.088	12.4	349.7	0.225	10.4	314.0	2.477	19.2	274.2	5.606	15.5
263.5	1.311	36.1	273.0	7452	17.1	386.6	0.334	14.2	355.9	0.379	30.0	309.3	3.762	16.0
380.6	0.713	16.0	308.9	3.750	12.9	399.7	2.613	16.1	463.0	0.223	30.0	400.4	0.185	13.9
395.1	0.106	2.3	428.5	1105	30.0	439.7	1.825	15.2	508.2	4.537	14.2	433.5	1.010	30.0
410.5	0.363	8.9	475.2	7.074	19.3	466.8	4.755	19.5	602.3	1.279	10.8	459.7	2.497	20.8
450.9	7.521	18.8	523.2	0.251	7.9	595.0	1.587	15.6	621.5	0.446	27.4	486.5	5.466	13.7
558.8	0.409	22.1	559.2	0.371	13.0	628.8	1.178	13.1	674.6	0.249	28.9	518.0	0.284	10.5
610.6	2.457	30.0	599.0	0.937	12.0	656.7	1.394	25.3				546.1	0.145	14.5
633.3	1.238	20.0	616.3	1.145	8.9							604.9	0.998	15.7
			636.4	0.452	14.0							632.0	0.923	16.1
												668.1	0.136	30.0
978.0	73.484	4.3	995.0	10.267	8.0	986.3	1.433	6.3	879.0	0.086	38.3	991.1	9.854	14.3
1020.0	0.381	7.5	1021.0	10502	9.0	1004.0	4.607	15.1	987.0	0.600	30.0	1008.0	2.785	9.1
1068.0	0.346	26.4	1101.0	0.198	3.0	1032.5	7.873	13.9	1025.8	37.732	7.6	1030.2	4.326	11.1
1102.8	1.949	18.7		5127	17.8	1050.8	4.539	18.8	1090.5	0.835	30.0	1057.2	1.502	30.0
1141.3	0.527	21.1	1131.8	2.313	12.1	1085.3	0.151	15.3	1116.7	0.068	18.1	1117.1	4.463	21.4
1206.5	0.125	30.0	1154.4	0.761	21.5	1119.3	0.560	30.0	1167.5	1.380	21.9	1153.1	2.699	18.0

Table 5.1. (cont.)

1593.2	0.083	33.6	1198.0	0.792	30.0	1160.0	1.175	30.0	1202.4	3.738	8.9	1176.9	0.363	7.8
1647.6	0.243	33.8	1227.0	0.285	10.4	1209.3	3.923	17.8	1221.0	0.530	25.3	1189.6	0.406	17.2
			1276.0	0.086	30.0	1244.9	0.171	30.0	1315.1	0.098	50.0	1226.5	0.501	30.0
			1634.0	0.447	30.0	1640.1	0.104	30.0	1641.1	0.175	50.0	1622.7	0.293	50.0
			1654.0	0.511	16.8				1702.0	0.044	30.3	1658.1	0.468	18.5
3241.7	0.830	85.8	3169.1	1.583	147.0	3196.7	1.178	218.9	2979.0	1.135	154.3	2876.0	0.213	220.0
3436.6	2.563	103.8	3309.0	0.495	56.3	3448.0	1.084	119.0	3158.5	1.178	140.3	3148.3	1.109	154.9
3344.9	0.465	137.3	3423.4	0.832	100.0				3340.3	0.617	108.8	3386.7	1.148	174.4
			3490.4	0.336	21.4				3580.6	0.297	11.5	3525.1	0.420	28.9
			3531.6	1.263	20.0									

91RS202D3			91RS204DriftA_Ca			91RS204DriftA_Cb		
Position	Intensity	HWHM	Position	Intensity	HWHM	Position	Intensity	HWHM
170.7	0.247	5.3	184.9	2.059	8.6	175.8	1.315	15.6
186.0	2.351	19.5	214.4	0.976	11.9	199.8	2.559	12.9
211.1	4.154	15.0	278.2	0.276	9.0	229.6	3.063	22.2
254.9	3.383	21.7	309.8	0.763	30.0	250.6	1.957	9.6
262.1	114.555	0.1	316.4	0.438	7.6	272.4	6.445	15.9
286.8	8.847	15.4	417.0	14229	7.8	307.9	5.134	11.8
318.0	1.794	20.7	442.7	1.116	15.0	412.0	0.446	21.1
354.8	0.230	9.0	462.0	1215	9.5	458.0	3.365	14.0
457.4	0.630	10.4	477.1	1.931	8.2	479.9	6.078	12.7
471.3	1.428	25.5	495.9	11876	9.7	556.4	0.666	10.9
506.2	3.826	14.4	607.6	1.862	27.8	569.0	0.294	13.3

Table 5.1. (cont.)

536.0	0.444	30.0	621.7	4.527	9.4	598.0	1.361	10.3
602.3	1.962	13.3	670.1	0.644	20.4	617.0	0.781	9.7
629.1	0.287	13.0	672.5	3.366	6.5	641.4	0.793	10.8
656.5	0.285	30.0				657.0	0.186	30.0
852.1	0.160	30.0	995.0	2064	30.0	830.7	0.112	30.0
1000.0	1.729	19.0	1009.7	48.844	5.2	960.6	0.386	26.0
1025.5	24.185	9.4	1126.0	1222	30.0	997.9	11.225	11.2
1053.0	1.687	18.5	1138.6	5.524	7.1	1021.4	10.032	6.6
1101.2	3.099	19.4	1452.6	3086	6.6	1034.5	1.745	16.0
1202.5	5.180	9.4				1157.1	1.446	30.0
1225.0	0.658	27.1				1196.3	0.594	1.5
1640.0	0.174	60.0				1221.2	0.399	30.0
						1639.9	0.565	30.0
3138.8	1.503	190.0	2550.4	0.210	30.0	3152.9	1.685	137.5
3281.1	0.378	89.9	2658.4	2.150	16.9	3301.9	0.454	75.7
3412.7	0.700	67.0	2778.5	3192	21.7	3411.8	0.948	122.9
			2846.8	0.311	96.1	3517.8	0.598	34.6
			3290.0	0.510	112.2			
			3406.4	3.645	22.1			
			3493.6	2501	20.2			
			3572.0	0.245	109.4			

[a] Relative intensity ($\times 10^{-3}$)

[b] Half width at half maximum

Table 5.2. Composition of the samples from Iron Mountain Mine

SAMPLE	COMPOSITION
90RS118	**Melanterite**
91RS201Ba	**Copiapite**
91RS201Bb	**Voltaite**
91RS201Bc	**Coquimbite + copiapite**
91RS204A2	**Copiapite**
91RS204D3	**Coquimbite**
91RS204DriftA_Ca	**Gypsum**
91RS204DriftA_Cb	**Ferricopiapite**

5.3. Raman spectroscopy of efflorescent sulfate salts from Rio Tinto

5.3.1. Abstract

Sulfate-rich precipitates are found in mine tailings such as Rio Tinto. In this work we have identified some efflorescent salts and precipitates by means of Raman spectroscopy. Solid samples have been identified as gypsum and as mixtures of hydrated iron(II)/iron(III) oxides belonging to the copiapite-group.

5.3.2. Experimental

5.3.2.1. Sampling

Efflorescent and precipitate minerals were collected from several spots in Rio Tinto area. A map illustrating all collection sites is presented in Figure 5.3. The collection site is close to Peña de Hierro, within one of the branches considered as one of the river's true sources.

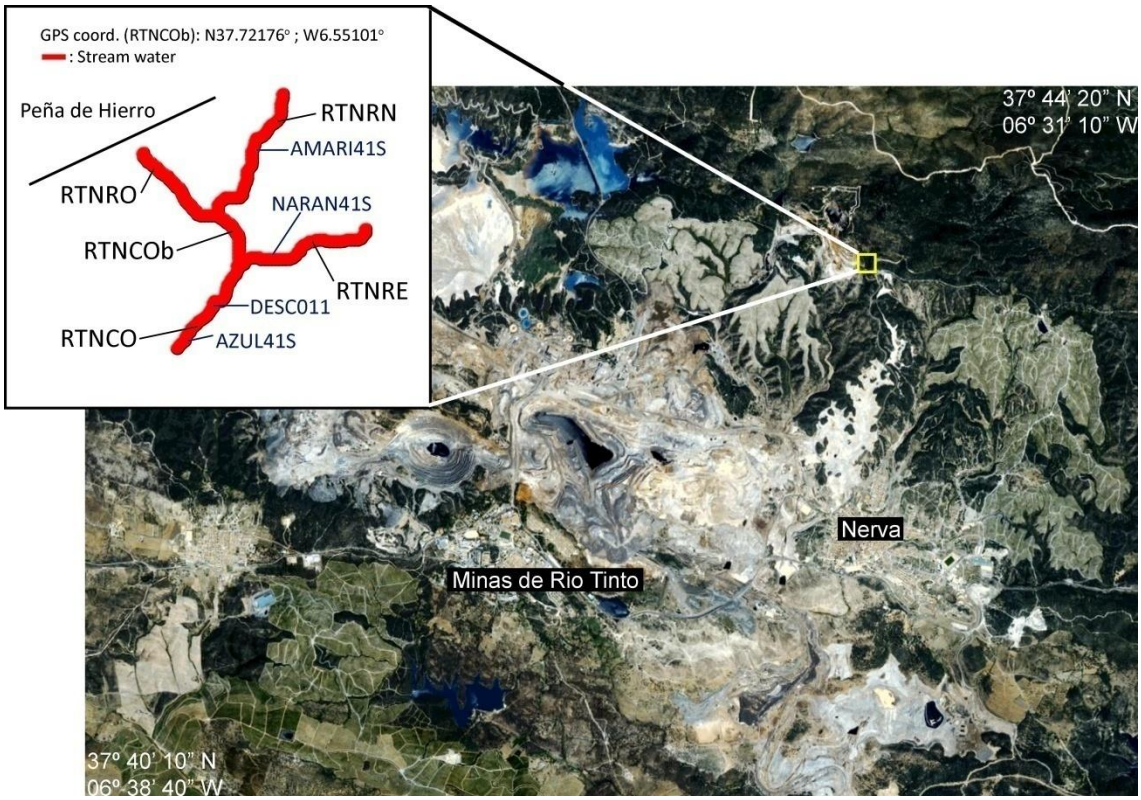

Figure 5.3. Map of the Rio Tinto mining with enlarged sketch of the sampling sites

5.3.2.2. Raman spectroscopy

The samples were placed on a 3D-motion stage of a Nikon Eclipse microscope, equipped with 5×, 20× and 50× objective lenses. The microscope is connected to a Kaiser HoloSpec f/1.8i spectrograph. An Andor iDus DV420A-OE-130 coupled charge device (CCD) attached to the spectrograph was used to collect the Raman spectra. The 632.8 nm line from a Research Electro-Optics LSRP-3501 He-Ne laser was used as excitation source. The spectra were recorded within the region 200-3800 cm^{-1} with a spectral resolution of 4 cm^{-1}.

5.3.3. Results and discussion

Figure 5.4 shows the Raman spectra of the samples labeled as AMARI41S (Am), AZUL41S (Az), DESC010 (Ds) and NARAN41S (Nr) in the low-wavenumbers region. The result of the Raman spectral analysis is reported in Table 5.3. Raman spectra of sulfate-

bearing minerals are based on the combination of the spectra of the sulfate and water. The v_2 and v_4 degenerate vibration modes of sulfate give raise to bands at 450 cm^{-1} and 625 cm^{-1}, respectively (*cf*. 2.2). Reduction in symmetry in the crystal structure of sulfate rich minerals cause the splitting of these vibrational modes into two or more separate bands. This effect is clearly observed in the Ds sample. The 410 and 490 cm^{-1} doublet and the 614 and 667 cm^{-1} doublet are believed to originate from the degenerate v_2 and v_4 vibrational modes, respectively. The spectrum indicates the possibility that the Ds is composed of gypsum (Dickinson and Dillon, 1929). The Raman spectra of the Am, Az and Ds samples show two sets of bands centered around 450 and 600 cm^{-1}. Five bands are observed at 408, 422, 459, 479 and 507 cm^{-1} for Am sample and are attributed to v_2 sulfate bending modes. For Az sample three bands are observed at 425, 445 and 463 cm^{-1}, also ascribed to the v_2 sulfate bending modes. For Nr sample three bands are found at 400, 453 and 481 cm^{-1}. The second set of bands found around 600 cm^{-1} is characteristic of v_4 sulfate bending modes. For Am sample five bands are found at 557, 596, 613, 639 and 666 cm^{-1}. Two bands are observed at 605 and 623 cm^{-1} for Az sample. Nr sample shows four bands at 552, 607, 636 and 664 cm^{-1}. A set of bands around 300 cm^{-1} is observed in Am and Nr samples but is not found in Az and Ds samples. It is characteristic of iron(III) hydroxides and may be ascribed to Fe-O stretching vibrations (section 4.3 and Sobron *et al.*, 2007a). The presence of this set of bands, along with the sulfate bending bands in Am and Nr samples suggest the presence of hydrated iron(III) sulfates.

The Raman spectra of the samples in the 800-1300 cm^{-1} region are shown in Figure 5.5. The bands centered at 982 cm^{-1} and 1105 cm^{-1} belong to the v_1 and v_3 symmetric and asymmetric stretching modes of sulfate, respectively, when in aqueous solution (*cf*. 2.2). Due to the symmetry breakdown of the sulfate tetrahedral structures in a crystal lattice a split in the v_1 and v_3 symmetric and asymmetric stretching bands is expected in sulfate-bearing minerals. The Nr sample is characterized by seven bands at 991, 1005, 1021, 1053, 1105, 1123 and 1147 cm^{-1}. The Am sample shows six bands at 993, 1002, 1020, 1101, 1129 and 1166 cm^{-1}. Band positions and relative intensities are very close in both sets. This suggest the presence of the same chemical bonding in both samples, however bands are broader in Nr sample. The sharper sulfate bands for

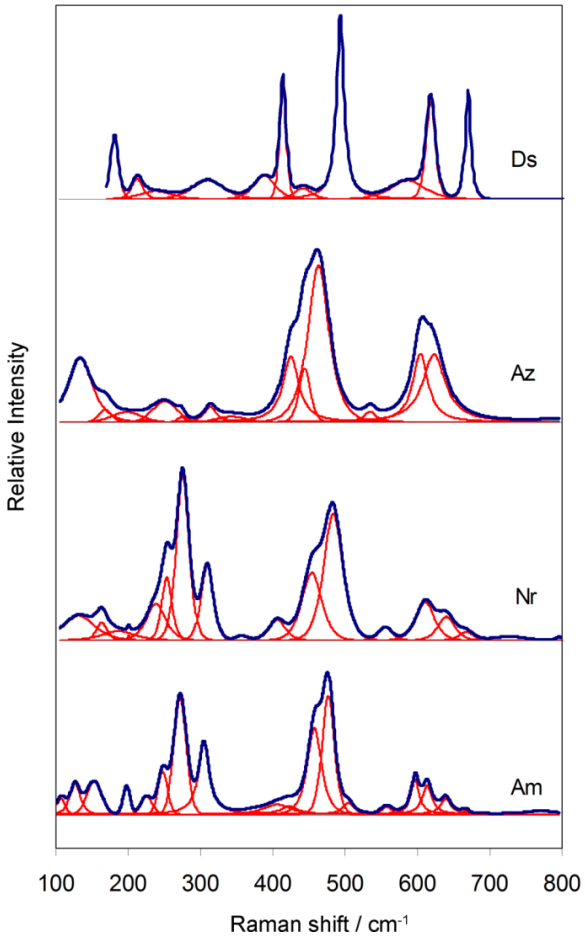

Figure 5.4. Raman spectra of samples Am, Nr, Az and Ds in the low-wavenumbers region. Blue envelope: Raman spectrum, red bands: Raman bands

Am sample indicate the Am to be more crystalline than the Nr. The same effect is observed for the sulfate asymmetric stretching bands, centered at 1199 and 1225 cm^{-1} in Am sample and at 1201 and 1232 cm^{-1} in Nr sample.

The Az sample shows five bands in the sulfate symmetric stretching centered at 972, 995, 1007, 1180 and 1155 cm^{-1}. The shoulders in both sides of the most intense band are likely associated with a distortion of the sulfate ion by hydrogen bonding and iron(III) direct complexation (section 4.2. and Sobron at al., 2007a). Copiapite-group minerals are based upon the formula $AFe_4^{3+}(SO_4)_6(OH)_2 \cdot 20H_2O$ where $A = Mg^{2+}$, Fe^{2+}, Cu^{2+}, $Al_{2/3}^{3+}$, or $Fe_{2/3}^{3+}$. The Raman shift of the v_1 sulfate stretching mode depends on the ionic radius of the cation bonded to the sulfate ion (Sasaki *et al.*, 1998; Chio *et al.*, 2005; Frost *et al.*, 2005). The Raman shift of the sulfate band and the blue

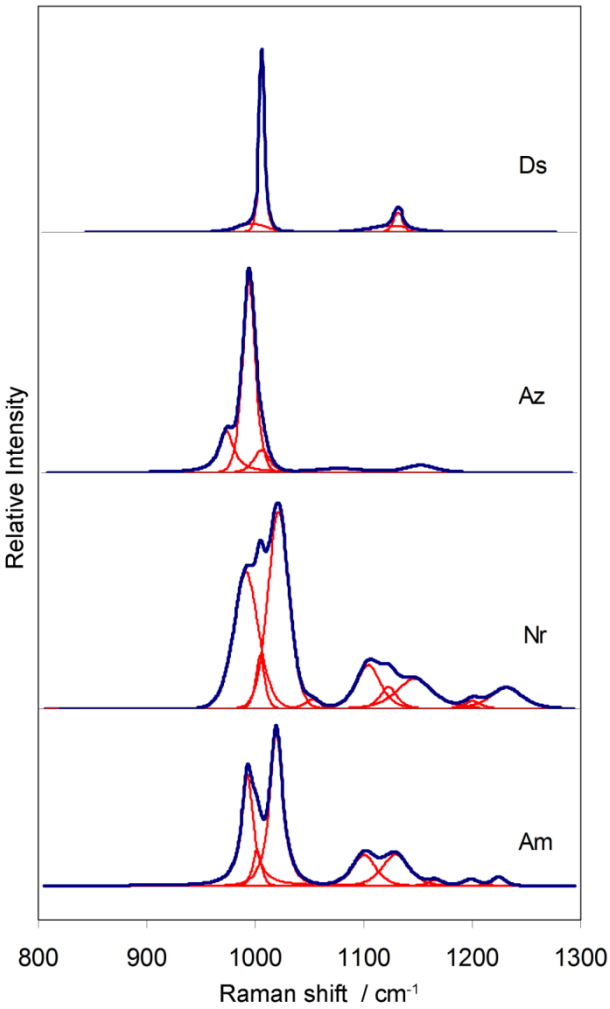

Figure 5.5. Raman spectra of samples Am, Nr, Az and Ds in the mid-wavenumbers region. Blue envelope: Raman spectrum, red bands: Raman bands

color of Az sample suggest the presence of cuprocopiapite. For Ds sample two intense bands are found at 1006 and 1133 cm^{-1} with shoulders at 996 and 1126 cm^{-1}, respectively. The presence of shoulders in the v_1 and v_3 sulfate bands may be due to higher site symmetry of Ds sample in comparison to the other samples.

Figure 5.6 shows the Raman spectra in the region 2800-3700 cm^{-1}. The OH stretching vibrations give raise to bands in this region, which in general overlap with water vibration bands for hydrous sulfates. For Am sample seven bands are found at 3091, 3198, 3307, 3394, 3491, 3526 and 3658 cm^{-1}. The same number of bands is observed in Nr sample, slightly shifted to 3101, 3186, 3315, 3399, 3486, 3524 and 3659 cm^{-1}. The sharp band at 3526 cm^{-1} may be assigned to Fe^{3+} /Fe^{2+}-OH vibration, and the

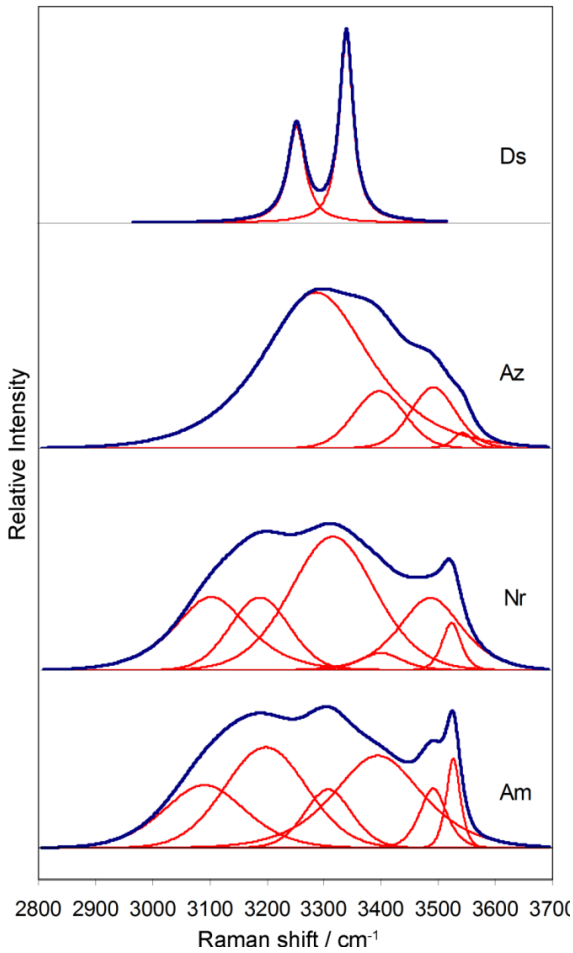

Figure 5.6. Raman spectra of samples Am, Nr, Az and Ds in the high-wavenumbers region. Blue envelope: Raman spectrum, red bands: Raman bands

broad continuum around 3200 cm^{-1} may be associated with water stretching vibrations, and therefore both samples may contain hydrous iron(II) and iron(III) oxides, likely belonging to the copiapite group. The yellow color of Am sample suggest the presence of ferricopiapite, $Fe_5^{3+}(SO_4)_6(OH)_2 \cdot 20H_2O$. Nr sample may be an iron(II)/iron(III) copiapite $Fe^{2+}Fe_5^{3+}(SO_4)_6(OH)_2 \cdot 20H_2O$. For Az sample four bands are observed at 3287, 3398, 3493 and 3544 cm^{-1}. The band at 3287 may be assigned to water in coordination with a cation. The same band was found at 3200 cm^{-1} for Nr and Am samples. The shift in 87 cm^{-1} of the band in the Az sample suggests the presence of a different cation.

The sharp band found for Nr and Am samples at 3526 cm^{-1} is observed as a shoulder in Az sample. This intensity decrease indicates a weakening of the cation-OH

bridging. It is suggested the presence of copper, whose ionic radius is greater than that of the iron. The presence of cuprocopiapite, $Cu^{2+}Fe_4^{3+}(SO_4)_6(OH)_2 \cdot 20H_2O$ is consistent with the analyses of the band analysis in the low and mid-wavenumbers regions of Az sample. Two intense bands are found in Ds sample. The higher frequency band is assigned to symmetrical bending vibrational modes whereas the lower frequency mode is ascribed to asymmetrical bending modes. They may arise as a consequence of the presence of two water molecules in the unit cell of gypsum, and as such is considered to be present in the Ds sample.

The mineral composition of the analyzed samples is summarized in Table 5.4.

Table 5.3. Results of the Raman spectral analysis of the natural sulfates from Rio Tinto

Ds			Az			Nr			Am		
Position	Intensity[a]	HWHM[b]	Position	Intensity	HWHM	Position	Intensity	HWHM	Position	Intensity	HWHM
176.9504	13,153	6.943515	132.5	99	22.1	129.1	120	25	106.1	87	8
208.6307	4,124	10	168.5	20.152	9.2	158.5	88	8.5	128.4	188	7.1
234.4785	1,624	27.30143	199.5	16	25	182	45	24.5	153.2	190	12.2
306.6903	3,892	27.25807	216.4	3.251	7.9	197.5	24	3	197.7	165	7
385.3199	4,808	18.49933	252	34	19.8	233.1	171	14.9	223	104	9.5
410.6924	23,697	5.673723	273.6	8.25	7.2	249.8	310	8.1	247.1	249	7.5
438.5456	2,239	15	305.5	24	10.3	273.3	827	12.2	271.8	690	10
490.5377	37,641	6.183748	344.1	9.182	20.5	305.2	364	11.3	304.2	426	8.3
584	3,784	30	425.6	100	12.1	352.5	25	8.5	372.3	17	12.8
616.0425	19,868	8.304241	440.9	84.012	8.9	402.1	101	12	406.2	58	18.1
668.0429	22,090	4.496022	466.2	250	18	449.7	320	16.4	421.9	45	9.4
			531.1	16.216	10	482.5	606	16	457.5	510	10.1
			602.3	107	11.5	552.2	68	11.2	476.6	12	11
			622.1	104.812	19.2	605.7	185	15.8	505.1	70	6.9
						636.1	115	15.3	557.5	42	6.1
						668	38	14.5	595.7	209	6.2
						726.5	22	27	613.5	171	7.1
									640.1	90	9.5
									667.2	22	4.5
									771.1	20	21.1
996	22,849	17.4436	972	500.2	9	992.1	1,126	12.1	993.1	630	6.5
1005.78	480,893	2.940867	993.2	2,300	6.5	1105.3	455	5.1	1002.2	515	5.1

Table 5.3. (cont.)

1125.96	16,519	27.82952	1006.1	270	7.2	1021	1,629	11.2	1019	2,260	8
1132.751	52,493	5.699048	1077.5	55.8	18.1	1053.2	76	5.9	1100.9	451	12
			1153.7	101	13.9	1102.8	361	10.1	1028.5	441	11.5
						1123.5	177	9.5	1166.7	91	6.2
						1147.5	253	16.5	1195.5	100	5.5
						1201.8	71	5.5	1224.4	118	5.5
						1233	183	18			
3404.809	0	16.21844	3282.1	744		3102.1	343	71.5	3091.5	308	80
3492.298	0	13.95935	3404.5	270.655		3188.5	340	60.1	3201	493	82.5
			3497.2	289		3315.8	625	86.7	3309.5	286	47.9
			3548	72.031		3405.2	79	45	3393.2	451	88.1
						3487.1	339	66.9	3489.8	290	29.5
						3524.9	221	20	3526.5	435	14.3

[a] Relative intensity

[b] Half width at half maximum

Table 5.4. Composition of the samples from Rio Tinto

SAMPLE	COMPOSITION
DESC011	**Gypsum**
AZUL41S	**Cu-copiapite**
NARAN41S	**Copiapite**
AMARI41S	**Fe-copiapite**

5.4. Combined Raman, Visible-Near Infrared reflectance and X-ray diffraction study of efflorescent sulfates from Rio Tinto

5.4.1. Abstract

In this section we report a characterization of some evaporitic salts from Rio Tinto by means of Raman spectroscopy, VNIR reflectance spectroscopy and X-ray diffraction (XRD). These techniques have been, and to great extent still are, considered as laboratory techniques. Nevertheless, in recent years many systems have been specifically designed for field use and planetary exploration, either for contact or remote investigations. In this context, the Raman/LIBS combined contact instrument has been ranked as a "Fundamental Instrument" for the ESA ExoMars mission, and an X-ray diffractometer is also scheduled for the mission ranked as a "Very Important Instrument" (ESA Pasteur Progress Letter 4, 2004). The LIBS technique has been successfully applied to remote sensing of distant targets (Knight *et al.*, 2000) whether or not it will be finally included within the Mars Science Laboratory ChemCam. (NASA News Release 04-398, 2004). Also reflectance spectroscopy has proved for years to be a sensitive mineralogical tool for the geological and geochemical studies of planetary surfaces. (Gendrin *et al.*, 2005).

The combination of Raman spectroscopy, reflectance spectroscopy and X-ray diffraction has been tested on natural samples from Rio Tinto. The small differences observed upon interpretation of the results from the three techniques allow obtaining a complete picture of the mineralogical composition of the samples.

5.4.2. Experimental

5.4.2.1. Sampling

Efflorescent salts from acidic surface stream waters were collected from several sampling spots near the site considered as the source of the river, Peña de Hierro (Spanish for iron crag). The site is named after the intensive mining developed in its surrounding devoted to the extraction of iron.

5.4.2.2. XRD

XRD was performed using the "mini-Chemin" instrument (*cf*. 2.4). The miniChemin instrument consists of a power supply / X-ray tube, sample holder, CCD detector, control electronics, computer and battery/power management system. The powdered samples have been flowed into the cell through an opening at the top. The sample holder employs a sonic frequency piezoelectric shaker system, which causes the powdered sample material to flow with a convection pattern similar to a liquid, exposing all grains to the beam in random orientation. This allows "mini-Chemin" to use coarsely ground powder not suitable for standard XRD systems. Mineral identification was achieved through peak comparison against the ICCD mineral database.

5.4.2.3. VNIR reflectance

VNIR spectra were measured using a FieldSpec®ProFR from Analytical Spectral Devices (ASD) with a contact probe and solar simulated light source. This system is designed for lab and field use, and was used in the lab in this study. Spectra were measured relative to Halon of spots ~1.5 cm across on the rock surfaces at 2 nm spectral resolution from 0.35 to 2.50 µm.

5.4.2.3. Raman spectroscopy

The samples were placed on a 3D-motion stage of an inVia Raman microscope (Renishaw (*cf*. 2.3)), and analyzed using 20× objective lenses. The 632.8 nm line from a Renishaw He-Ne laser was used excitation source. Laser power at the sample was measured as 1mW. The spectra were recorded within the region 100-3500 cm^{-1} with a spectral resolution of 4 cm^{-1}.

5.4.3. Results and discussion

XRD patterns of the samples are displayed in Figures 5.7 to 10. The XRD patterns of samples RTNP10, 5 and 3 are dominated by gypsum, while the XRD pattern of sample RTNP07 includes contributions from copiapite and jarosite. Traces of jarosite are also observed for the 10 and 5 samples. The additional peaks in the 3 samples are more likely due to Na-jarosite. Quartz is a major component in sample RTNP03, and is also present in samples RTNP07 and 10.

Figure 5.11 shows VNIR reflectance spectra of two spots of ~1 cm in diameter on the surface of RTNP rock sample 03. These data are compared to particulate samples of K-jarosite (JB53), gypsum (JB556) and goethite (JB54) from previous studies (reflectance offset for clarity). Jarosite contains features at 0.43, 0.89, 1.46, 1.85 and 2.26 µm (*e.g.* Bishop and Murad, 2005) that correspond well to the features observed in the spectra of RTNP03. The strong water combination bands in the RTNP03 spectra near 1.45 and 1.95 µm are highly consistent with gypsum as well as the small shoulder near 1.76 µm (*e.g.* Bishop *et al.*, 2004). Goethite exhibits a broader Fe^{3+} transition than jarosite and reflectance peaks at 0.59 and 0.76 µm (*e.g.* Bishop *et al.*, 1993) that could be contributing to the RTNP03 spectra as well.

Figure 5.12 shows VNIR reflectance spectra of two spots ~1 cm in diameter on the surface of RTNP rock sample 05. These data are compared to particulate samples of gypsum (JB556) <63 µm, K-jarosite (JB53) <45 µm, ferricopiapite (JB620) <125 µm, ferrihydrite (JB499) <45 µm and goethite (JB54) <45 µm from previous studies (reflectance offset for clarity). Spectrum RTNP05_01 is consistent with jarosite, gypsum and goethite as in the spectra of sample RTNP03. Spectrum RTNP05_02 lacks the jarosite features and exhibit broader water bands at shorter wavelengths and a broader Fe^{3+} band at longer wavelengths more consistent with ferrihydrite (Bishop and Murad, 2002) and ferricopiapite (Bishop *et al.*, 2005). The Fe^{3+} reflectance peak near 0.6 µm is also consistent with goethite.

Figure 5.13 shows VNIR reflectance spectra of two spots ~1 cm in diameter on the surface of RTNP rock sample 07. These data are compared to particulate samples

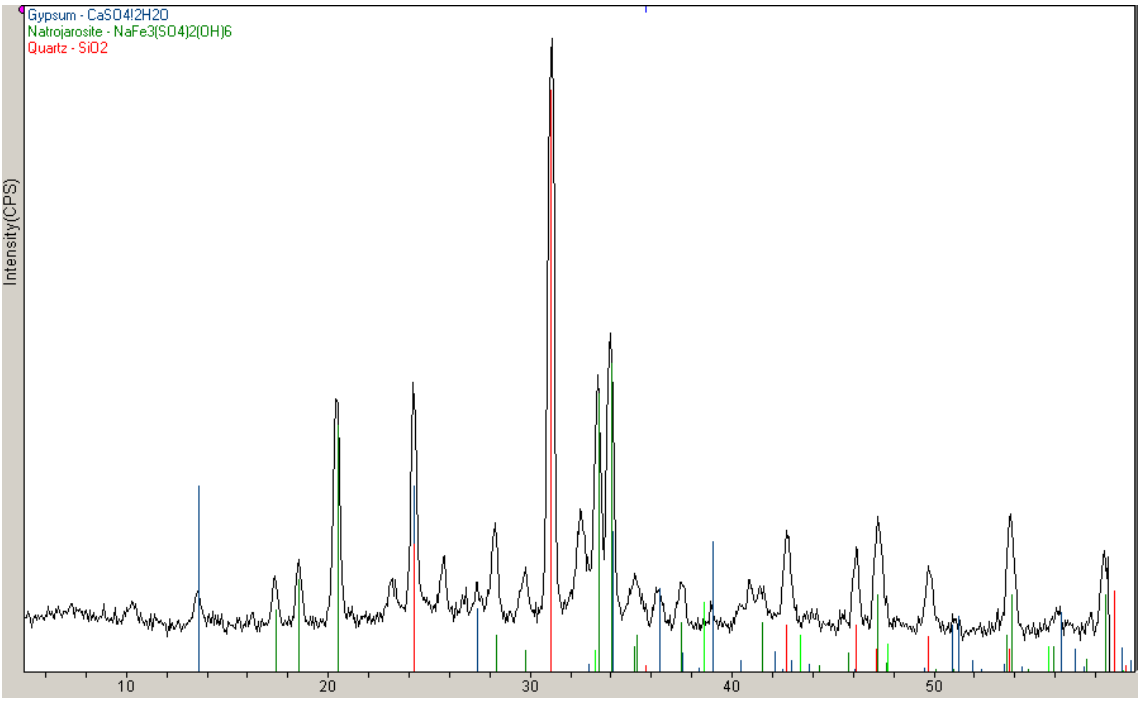

Figure 5.7. XRD pattern of sample RTNP03. Quartz, gypsum and Na-jarosite have been identified

of gypsum (JB556) <63 µm and ferricopiapite (JB620) <125 µm, each offset +0.1 for clarity. The Fe^{3+} bands at 0.43 and 0.87 µm are characteristic of ferricopiapite (Bishop *et al.*, 2005). The water bands at 1.44 and 1.93 µm are consistent with a combination of ferricopiapite and gypsum, and the weak feature at 2.2 µm is consistent with gypsum.

Figure 5.14 shows VNIR reflectance spectra of two spots ~1 cm in diameter on the surface of RTNP rock sample 10. These data are compared to particulate samples of gypsum (JB556) <63 µm, ferrihydrite (JB499) <45 µm, and goethite (JB54) <45 µm from previous studies. These spectra of rock RTNP10 are highly consistent with gypsum, matching the triplet at 1.44, 1.49 and 1.54 µm, the bands near 1.75 and 1.94 µm, and exhibiting the doublet at 2.20 and 2.26 µm. Some ferrihydrite is likely present as well due to the broadening of the Fe^{3+} band near 0.9 µm and the water bands near 1.4 and 1.9 µm, and some goethite is consistent with these spectra due to the shoulder near 0.6 µm.

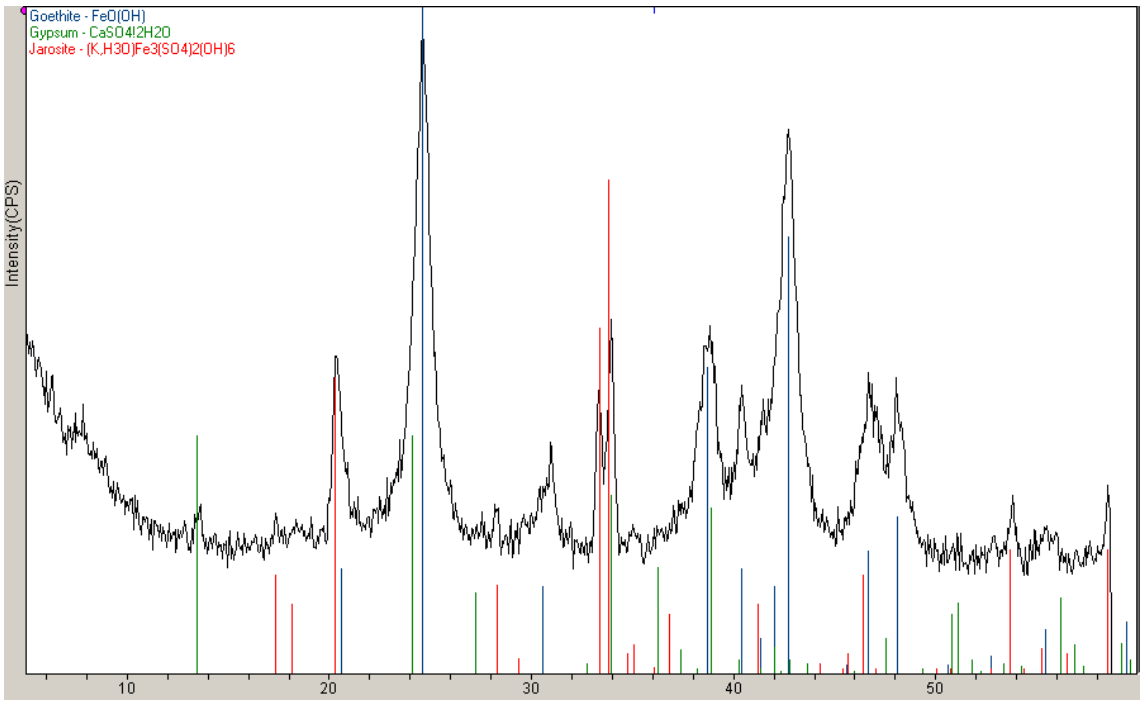

Figure 5.8. XRD pattern of sample RTNP05. Gypsum, goethite and K-jarosite have been identified

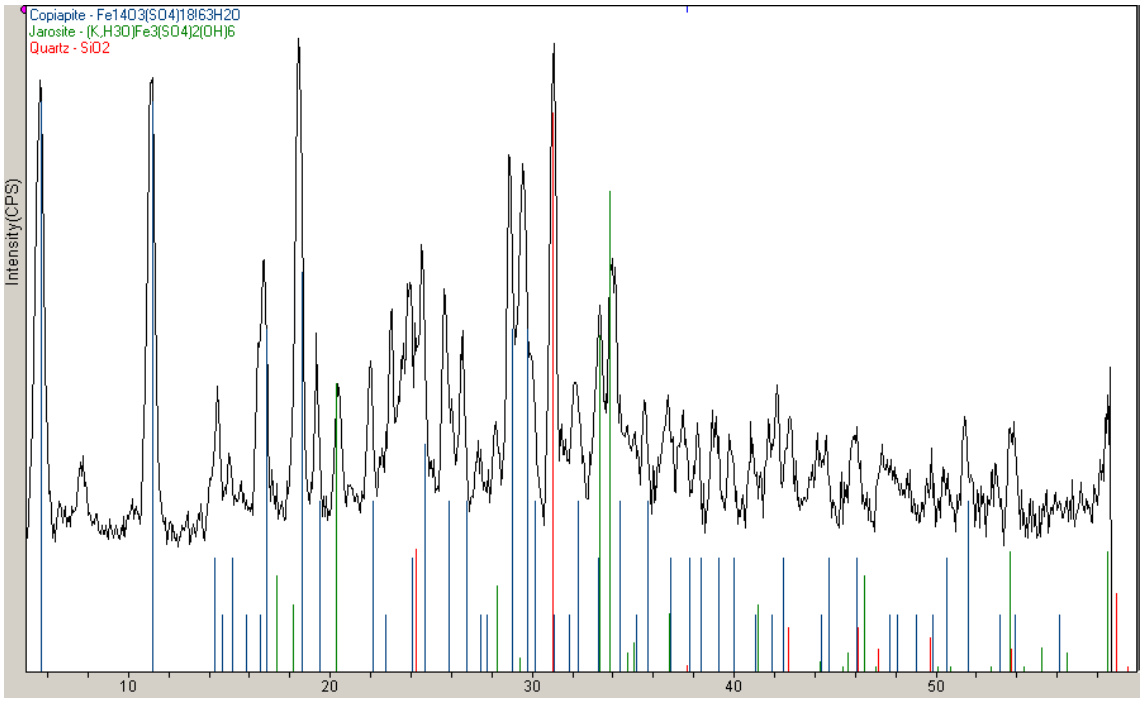

Figure 5.9. XRD pattern of sample RTNP07. Copiapite, K-jarosite and quartz have been identified

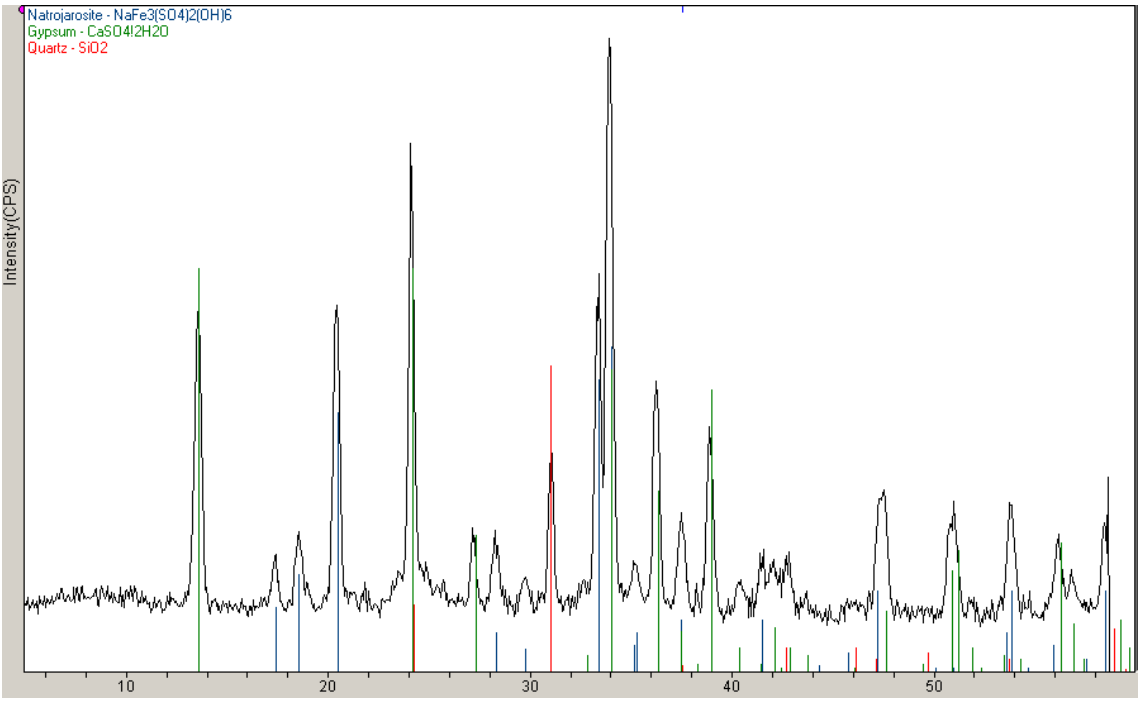

Figure 5.10. XRD pattern of sample RTNP010. Gypsum, quartz and Na-jarosite have been identified

In all cases, the reflectance spectra of the RTNP samples are darker than the lab mineral spectra. This is because the RTNP samples are all rock surfaces, while the mineral spectra are all particulate samples.

Raman spectra of sulfate rich minerals are mainly composed of bands arising from sulfate molecular vibrations and water (see section 2.2 for band assignment). The Raman spectra of the samples are shown in Figure 5.15. The effect of a reduction in symmetry in the crystal structure of these sulfate samples may be readily observed in the Raman spectra as the splitting of the sulfate bands in the wavenumbers region 100-1300 cm^{-1}. Two sets of bands centered around 450 and 600 cm^{-1} are found in all the Raman spectra. They are attributed to the v_2 and v_4 vibrational modes of the sulfate tetrahedral oxyanions, respectively (*cf*. 2.2). The presence of multiple bands around 1000 cm^{-1} for the RTNP07 sample indicates that different sulfates are present in the mineral structure. The sharp band at 3526 cm^{-1} may be assigned to Fe^{3+} /Fe^{2+}-OH vibration, and the broad continuum around 3200 cm^{-1} may be associated with water stretching vibrations, and therefore the sample may contain hydrous iron(II) and

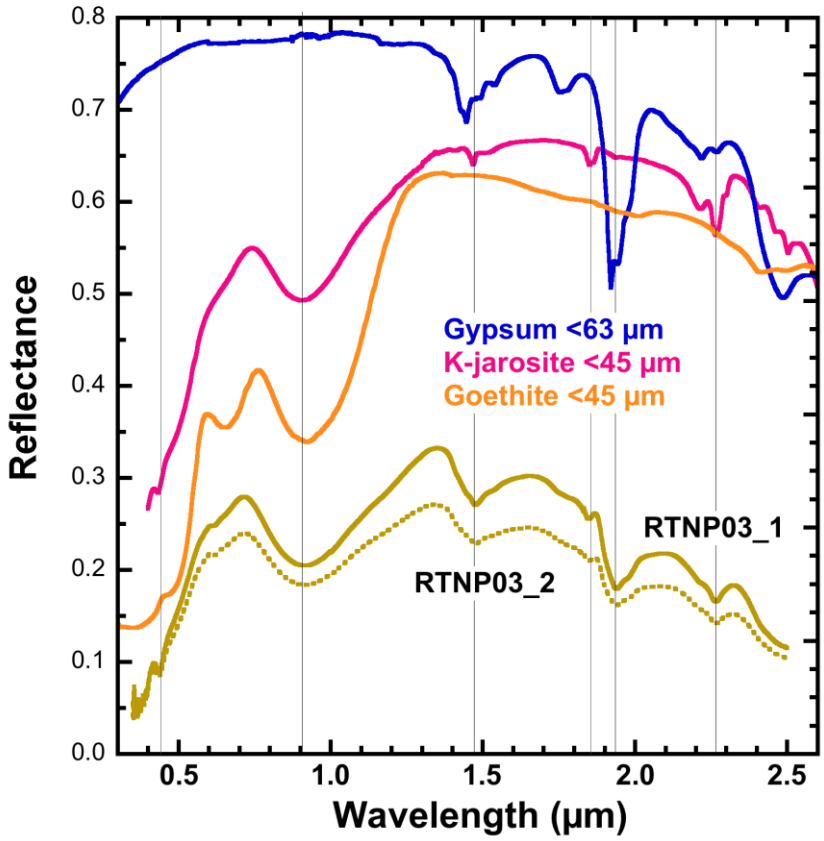

Figure 5.11. VNIR reflectance spectra of sample RTNP03 compared to spectra of gypsum, K-jarosite and goethite

iron(III) oxides, likely belonging to the copiapite group. The yellow color of the sample suggest the presence of ferricopiapite, $Fe_5^{3+}(SO_4)_6(OH)_2 \cdot 20H_2O$ as the predominant mineral phase. The existence of iron(II)/iron(III) sulfates is likely in an environment such as Rio Tinto since iron(II) may be easily oxidized into iron(III) when exposed to water, oxygen and often to microbes (López-Archilla *et al.*, 2001).

The Raman spectrum of sample RTNP10 shows two intense bands at 1006 and 1137 cm^{-1}. These bands are characteristic of gypsum (Dickinson and Dillon, 1929). The 410 and 490 cm^{-1} doublet and the 614 and 667 cm^{-1} doublet originate from the degenerate sulfate ν_2 and ν_4 vibrational modes, respectively. Additionally, the pair of bands located in the water-stretching region around 3406 and 3494 cm^{-1} are indicative of the presence of two water molecules in the unit cell, consistent with gypsum.

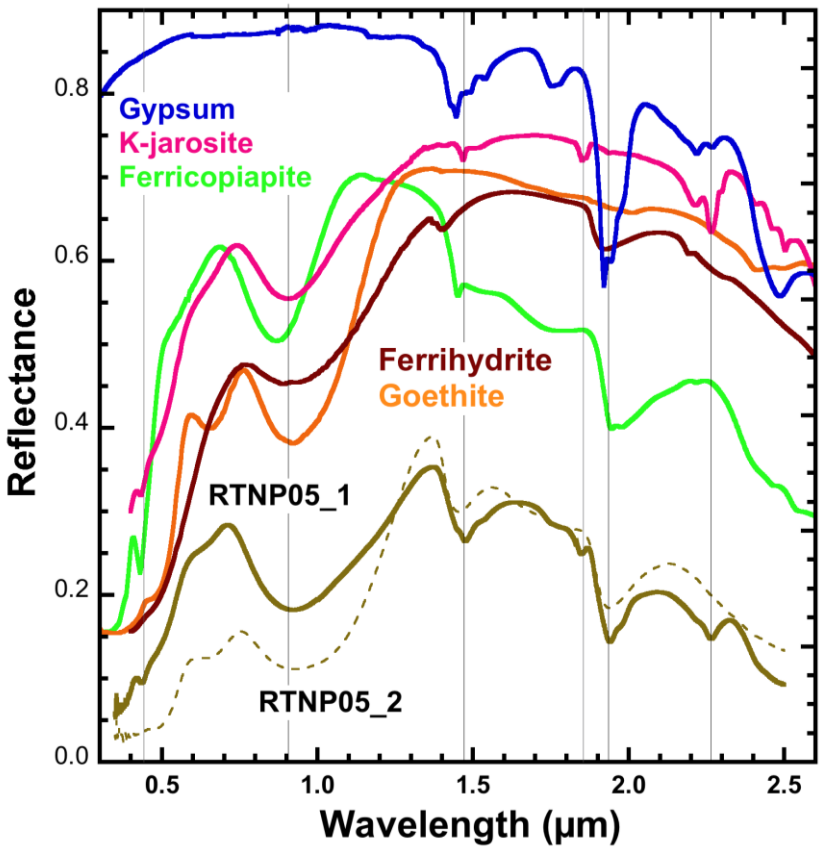

Figure 5.12. VNIR reflectance spectra of sample RTNP05 compared to spectra of gypsum, K-jarosite, goethite, ferrihydryte and ferricopiapite

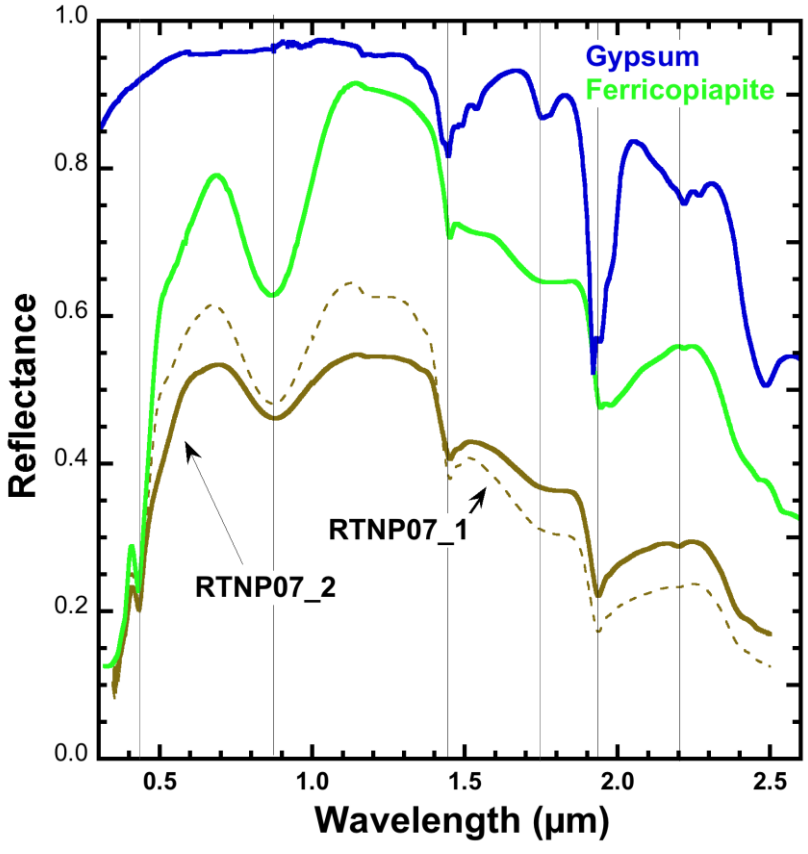

Figure 5.13. VNIR reflectance spectra of sample RTNP07 compared to spectra of gypsum and ferricopiapite

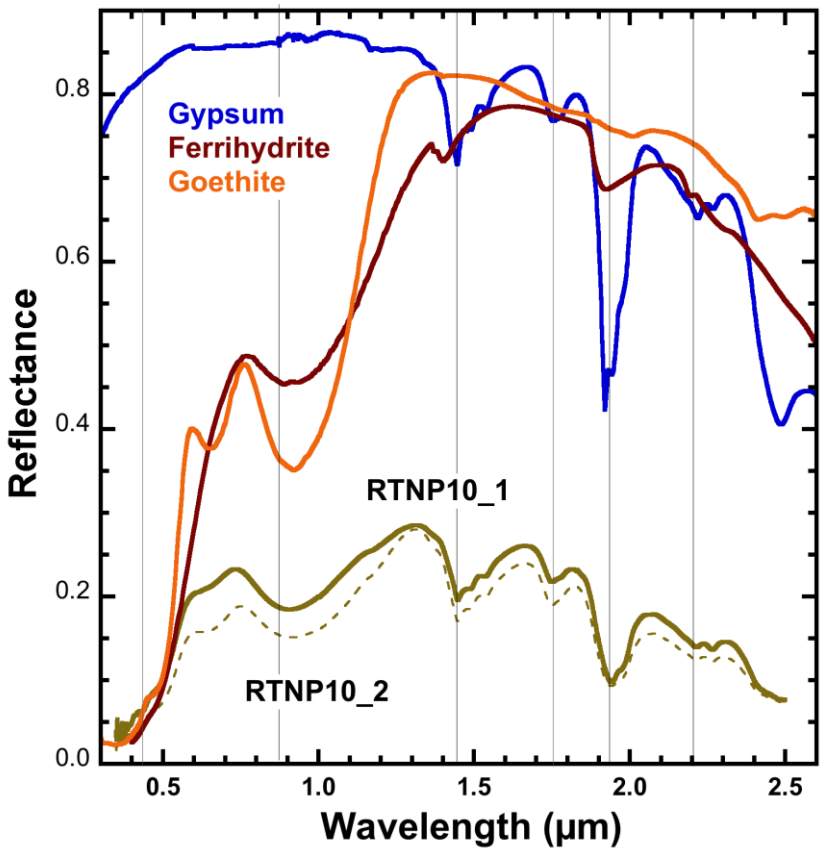

Figure 5.14. VNIR reflectance spectra of sample RTNP10 compared to spectra of gypsum, goethite and ferrihydryte

Two Raman spectra, RTNP05a and RTNP05b were recorded for the RTNP05 sample, corresponding to two *a-priori* different mineral phases. The 05a spectrum shows a sharp intense band at 3405 cm^{-1} with two shoulders at 3371 and 3443 cm^{-1}. A further band is observed at 3497 cm^{-1}. Jarosites show broad bands centered around those positions. (Chio *et al.*, 2005; Frost *et al.*, 2006a). However, the band at 3497 cm^{-1} is often hidden by the most intense band. This is not the case for the 05a spectrum. One possible explanation is that an additional concentration of water molecules, associated with other cations, is present in the sample. This is consistent with the presence of an additional sharp band at 1137 cm^{-1} in the sulfate stretching region, likely due to the presence of gypsum. The bands at 1108 and 1147, cm^{-1} are unambiguously assigned to jarosite, and the band at 1007 cm^{-1}, also characteristic of jarosites (Chio *et al.*, 2005), is located in the same position as that of the v_1 stretching

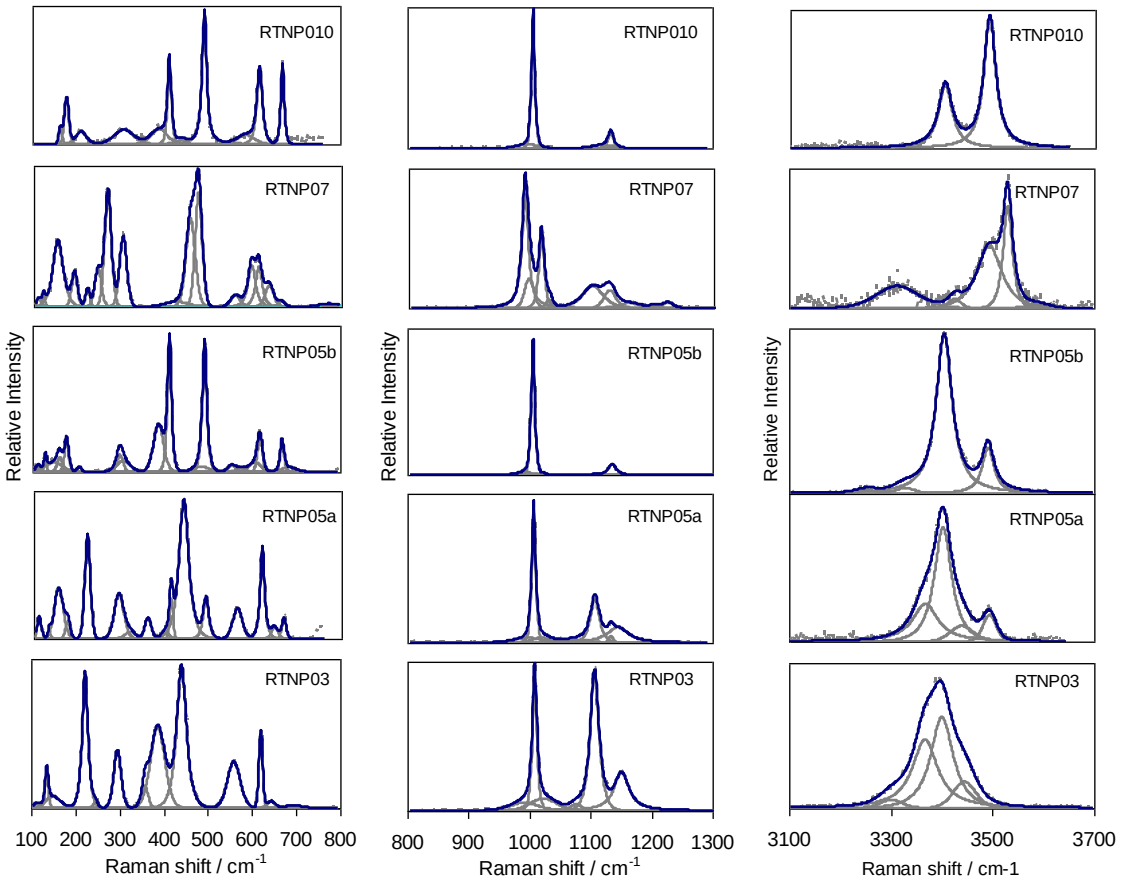

Figure 5.15. Raman spectra of the samples in the regions of interest

vibration of sulfate in gypsum. Therefore the Raman spectrum 05a of the RTNP05 sample contains fingerprints of both jarosite and gypsum mineral phases.

The RTNP05b spectrum looks similar to that of RTNP10 sample in the low and mid wavenumbers regions. However, the 05b spectrum shows two sharp bands at 3407 and 3493 cm^{-1} in the high wavenumbers region at approximately the same position as those of the RTNP10 sample. The relative intensities of those bands are inverted for the 05 sample, though. The relative intensity of the Raman modes is often sensitive to crystal orientation. It is suggested that the RTNP05 contains gypsum according to the 5b Raman spectrum, although the measuring and/or crystal geometries may vary from those of sample RTNP10. As for the RTNP05a, the RTNP03 Raman spectrum show characteristic features of jarosite. Additionally, a strong band is observed at 386 cm^{-1}, attributed to a vibration of the $[Fe(H_2O)_6]^{2+}$ complex (Sobron *et*

al., 2007b; Hester and Plane, 1964). Sample RTNP03 is composed of jarosite and probably an unidentified hydrated Fe^{2+} sulfate.

Table 5.5 summarizes the results from the three techniques used for the analysis of the Rio Tinto sulfates.

Table 5.5. Summary of the mineral identification of the Rio Tinto samples: major compounds (bold) and trace compounds (light)

	Sample ID			
	RTNP03	RTNP05	RTNP07	RTNP10
XRD	**Gypsum** **Quartz** Na-jarosite	**Gypsum** K-jarosite	**Copiapite** **K-jarosite** Quartz	**Gypsum** K-jarosite Quartz
VNIR	**K-jarosite** **Gypsum** Goethite	**K-jarosite** **Gypsum** **Goethite** Ferrihydrite Ferricopiapite	**Ferricopiapite** **Gypsum**	**Gypsum** Ferrihydrite Goethite
RAMAN	**K-jarosite** UnID sulfate	**Gypsum** **K-jarosite**	**Ferricopiapite**	**Gypsum**

Chapter 6

conclusions and future work

6.1. Summary and conclusions

In this thesis we have characterized synthetic aqueous systems that mimic the extreme conditions of Rio Tinto's stream waters. Natural acidic aqueous samples from the acid mine drainage site have been analyzed on the basis of the equilibrium relationships, speciation constrains, and mass transport properties derived from the Raman spectral investigations on the synthetic solutions. Sulfate efflorescent salts from Rio Tinto, along with samples from Iron Mountain, have also been characterized by means of Raman spectroscopy and complementary techniques such as VNIR reflectance spectroscopy and X-ray diffraction. Automated data-processing routines have been developed and implemented in VBA in order to retrieve the maximum Raman information from the Raman spectra while minimizing the contribution of noise and other artifacts to the collected spectra.

The iron(II) sulfate-sulfuric acid-water system originates when groundwater flows through the cracks in the crushed sulfides or sulfur-rich minerals. It is one of the major constituents in AMD, and is the direct cause of acidification of river's streams in mines. Accurate quantitative analyses of concentrations of species present in the system iron(II) sulfate-sulfuric acid-water have been achieved in this thesis, along with the characterization of the equilibriums in this system in terms of the activity coefficients product. This is essential in order to establish physico-chemical models of acid sulfate waters as this particular system turns out to have a highly non-ideal behavior. Further, Raman spectroscopy has provided a means to corroborate previous findings on the formation of iron(II) hexahydrate complexes in the mentioned system. The activity coefficients product has been calculated as a function of iron(II) sulfate concentration with iron concentrations exceeding Rio Tinto's. The logarithmic relationship between the activity coefficients product and the concentration of iron (II) sulfate found for this system gives an idea of the high non-ideality if this system, and allows to extrapolate values beyond the limits of salt concentrations used in this work.

For instance, the extremely acidic mine water from the Richmond Mine in Iron Mountain may contain up to 1.45 mol/kg of iron(II) (Nordstrom *et al.*, 2000).

Another system of relevance in the framework of the acid mine drainage is the iron (III)-sulfuric acid-water system. The speciation in the system monitored by Raman spectroscopy of synthetic solutions reveals the existence of sulfate-iron(III) interactions in the Fe^{3+} inner sphere through oxygens from the sulfate units and in the outer sphere through hydrogen bonds. The Raman technique provides the accuracy and repeatability critical for this qualitative and quantitative analysis. Particularly, molecular vibrations of iron(III) complexes are determined by specific wavelengths in the Raman spectra, and intensity and width changes of the Raman bands corresponding to iron(III) complexes molecular vibrations can be quantified very rapidly.

Investigation of the abovementioned systems allowed us to know the influence of salt and acid concentration on the intensities, widths and shapes of the bands ascribed to the sulfate, bisulfate and water molecules. Spectral fingerprints of these molecular structures have been detected in the Raman spectra of the stream water samples from Rio Tinto, and the relative abundance of sulfate and bisulfate ions and water, predominant species in acid mine ground waters, has been derived from the Raman spectra of the natural aqueous samples. Mine tailings such as the site under study contain large amounts of sulfur-rich mineral and are characterized by highly acidic waters. Characterization of the chemical constituents of stream water in acid mine drainage-contaminated sites is exceedingly important because it is extensively used to design treatment strategies. Further, an early detection of the ionic species associated with acid sulfate waters may help predicting the potential for acid mine drainage. For this purpose we have performed *ex-situ* Raman spectroscopy as a means of characterizing the hydrogeochemistry of Rio Tinto area. However, the possibility of using a portable Raman spectrometer for *in-situ* analysis of Rio Tinto stream waters and mineralogy is currently being explored and preliminary Raman spectra obtained *in-situ* (Rull *et al.*, 2003) justify the importance of Raman spectroscopy as a potential tool

for the characterization of Rio Tinto hydrochemistry, and hence of any environment containing acid mine drainage.

Diffusion of the molecular species within the system sulfuric acid-water has been monitored by Raman spectroscopy, a thermodynamic-chemical model of the mass transport properties of the species has been established, and its parameters optimized. It has been showed that the non-ideality of this system plays a crucial role in its mass transport properties, which however have been explained in terms of a diffusion model for the multicomponent system. In summary, the diffusion coefficients are not constant (characteristic of ideal systems) but are a function of the concentration of the species in solution. The model has been conceived in such a way that it can be adapted to any multicomponent mixture provided the equilibriums among the ions are known. We have shown that Raman spectroscopy may provide the means to derive the speciation and concentration of species in multicomponent systems, and thus the model-based measurement of the diffusion properties using Raman is presented as a robust and accurate technique.

Sulfate efflorescent salts (sampled at the same spots as the water samples) from Rio Tinto have been analyzed in this thesis. The spectral signatures from various forms of iron sulfates have been found in the samples and used for their identification. Gypsum and ferrous and ferric sulfates have been detected in the efflorescences.

Sulfate efflorescent salts from Iron Mountain, formed from extremely acidic waters via drainage from sulfide mining, have been also characterized by means of Raman spectroscopy. Gypsum, ferricopiapite, copiapite, melanterite, coquimbite and voltaite are found in the samples. However the Raman spectra of the samples are difficult to analyze, showing overlapping bands and shoulders that may be due to the inclusion of unidentified sulfates and hydroxides in the main mineral matrix.

No *in-situ* Raman spectrum was recorded, however recent advances in optics, lasers and detector systems have allowed for the development of compact field instruments for *in-situ* analyses. Particularly, the laser Raman technique has experienced outstanding advances in terms of portability and robustness in recent

years, and light-weight, small and tough field portable Raman spectrometers are commercially available at present day (*e.g.* B&W Tek Inc., 2006). It is our believe that in the coming years the Raman technique will become a routine analytical tool for field measurements, and future field work is expected to greatly benefit from the results of the research we have presented.

A suite of lab techniques have been used to investigate another set of mineral samples from the Rio Tinto environment. We have shown results of the visible/near-infrared (VNIR) reflectance spectra that can be compared to CRISM and OMEGA hyperspectral image cubes of Mars, X-ray diffraction patterns that can be compared with the Chemin instrument on MSL, and Raman spectra that are planned for ExoMars. A variety of mineral phases are detected within the samples, including K and Na-jarosite, gypsum, goethite, copiapite and ferricopiapite. The XRD technique detected quartz in some of the samples, however no traces of this component were detected by the other techniques. It is likely that the rock substrate underneath the evaporated sulfate layers contained quartz crystals. While VNIR reflectance and Raman spectroscopies, as non-destructive techniques, retrieved information from the evaporate layers alone, the powder used for the XRD analyses contained both sulfate layer and rock substrate grains, and thus information from the latter is included in the XRD patterns. The VNIR reflectance identified various sulfate compounds in each of the samples while XRD, and specially Raman only allow for identifying one or two different phases.

While VNIR spectroscopy has proven most powerful for the characterization of the water and anions in minerals, water is a very intense absorber and may mask the reflectance of the cation-hydroxil units (M-OH, where *M* represents a metallic cation). For this reason the identification of spectral features associated to hydrated minerals in the VNIR spectra is not always unambiguous. One of the advantages of Raman spectroscopy is that water is a very poor scatterer, and hence the hydroxyl stretching of the M-OH units can be better resolved, and as results, more accurate band assignments can be achieved. In any case, one of the difficulties associated with iron and sulfate-bearing compounds collected in field-work is that they are often found to

be poorly crystalline, making detection using XRD techniques difficult. XRD studies may be used to investigate those compounds, although the XRD patterns will be dominated by the highly crystalline compounds present in the mineral matrix, such as quartz in the case of the analyzed samples in this work. Vibrational spectroscopy techniques frequently enable better detection of sulfate materials. However, Raman spectra collection and interpretation is sometimes difficult for low crystalline minerals. Raman microscopy provides the means to overcome this difficulty and analyze spots in the order of 25 to 50 microns in diameter. However, by analyzing such small areas one constrain the mineralogical investigation to crystal-size spots, and frequently collects Raman spectra containing information from a single phase. On the other hand, VNIR spectra from spots ~1.5 cm across were measured, notably increasing the probabilities to find different compounds in a single spectrum. A Raman spectral map could have been measured on the samples in order to scan equivalent surfaces as the VNIR, but this would have required much longer times, and was beyond the scope of this thesis.

Nonetheless, the main goal of this combined analysis was to show that the three techniques are fully complementary and could be used simultaneously for the characterization of sulfate and iron rich mineralogy without sample preparation (except for XRD) and down to the crystal size (Raman). In samples were many hydrous sulfates are present, Raman and XRD can complement well VNIR reflectance by unambiguously telling among the different phases. For low crystalline samples, Raman can provide a definitive mineral identification, overcoming the difficulties associated with XRD in those circumstances.

In order to remove the spectral information related to non-Raman scattering phenomena, noise and baseline must carefully attenuated (or removed, when possible) after Raman spectra collection. Additionally, the instrumentally broadened Raman spectra must be processed in order to reduce the broadening and to obtain an equivalent to the true Raman spectrum. Commercial software (*e.g.* BRUKER Optics Inc., 2006; Thermo Fisher Scientific Inc., 2008) is available to perform the data treatment required to retrieve the information from the Raman bands ascribed to molecular vibrations. However, the commercial packages include proprietary software

that provides non-customizable and frequently non-user friendly graphical interfaces and unalterable calculus routines that, from our point of view, make the treatment of the Raman spectra a tedious task where the user loses control over the physical meaning of the data, at best. We understand that every Raman spectrum is unique and, as such, very flexible (although robust) data treatment routines are required for its analysis. For this reason we have developed own software for the post-processing of the Raman spectra. The routines conceived and developed as part of this thesis have been systematically applied to the collected spectra. All the routines have been implemented in Microsoft's Visual Basic for Applications (VBA) within Excel. Potential users of this software should just be familiar with the use of Excel's spreadsheets in order to handle the Raman data analysis through the nice and user-friendly graphical interface we have developed in the context of Excel.

The software includes noise reduction routines based on the Fast Fourier Transform, baseline calculations through linear interpolation, band Fourier self-deconvolution, and band fitting routines based on Marquardt method. Additionally, a search-match routine has been developed for an in-line estimation of predominant compounds in mineral mixtures. Construction of dedicated sample libraries through systematic collection programs is crucial for a full characterization of the samples. This is an ongoing task; new Raman spectra of organic and inorganic compounds are continuously being implemented in a database. With current computer processors (*e.g.* Intel® Core™2 Duo), the software package takes less than 1000 milliseconds to perform and in-depth automated postprocessing of a raw Raman spectrum, yielding the mineral composition of the sampled spot if compared against a suitable database.

6.2. Contributions of this thesis

In summary the main contributions of this thesis are as follows:

- An exhaustive Raman-based modeling of the chemical equilibriums, speciation, and mass transport properties of synthetic solutions that mimic the composition of stream waters containing acid mine drainage.
- A dedicated Raman spectroscopic characterization of stream water samples from Rio Tinto and sulfate and iron-bearing minerals from Rio Tinto and Iron Mountain Mine.
- A combined analysis of sulfate minerals from Rio Tinto by visible-near infrared reflectance spectroscopy, Raman spectroscopy and X-ray diffraction.
- The development and implementation of routines for the Raman data automated processing. The routines are written in Microsoft Visual Basic for Applications and are accessed through the user-friendly interface provided by Microsoft Excel.

6.3. Future Development

The results presented are just the first stage of the knowledge and advances that can achieved by means of Raman spectroscopic investigations on acid mine drainage-related aqueous and mineral systems. The novel results obtained and discussed in this thesis pave the way for future research on the treated topics. Particularly, the following issues could be subject to further investigation:

1. The systematic characterization of natural sulfate and iron minerals by means of Raman spectroscopy, visible-near infrared reflectance spectroscopy, X-ray diffraction and laser-induced breakdown

spectroscopy, among others. These techniques have demonstrated to be fully complementary (*e.g.*, Figure 6.1). Dedicated laboratory combined analyses of selected natural solid samples with these techniques would reveal important features from the present mineral phases such as crystallinity, hydration state, cationic substitution and thermal decomposition.

2. These features may be correlated with the nature of the aqueous system from which the minerals are formed, allowing for the establishment of detailed precipitation models (sequences) for each of the mineral phases found in the samples in accordance with day-night and seasonal temperature variations in the field sites. Such models are really a definition of the range of environmental stability for each mineral, *i.e.*, a classification of the minerals as a function of their precipitation order, or increasing solubility in a given aqueous system. The reverse application of those precipitation models to the current Martian iron sulfate mineral phases would for instance help obtaining a complete picture of the acidic waters that once flooded that planet's surface via describing phase relations in those waters.

3. From comparison of derived models for synthetic and natural precipitation of sulfate minerals within acid mine drainage and acid mine drainage-like aqueous solutions, information on the occurrence of mineral phases and their main features may be obtained and correlated with the aqueous systems, pressure, temperature, and biological activity (if present) conditions. In line with some of the objectives of the NASA Astrobiology Roadmap, these results could serve as a basis for future attempts in modeling the Martian acidic aqueous systems from which today's Martian mineralogy is thought to have originated, and in which the presence of microorganisms could have played a crucial role.

4. The precise chemical composition of acid mine drainage and associate mineralogy could be determined and then correlated with bands' features in the Raman spectra. This would be the basis for the establishment of measuring protocols for the concentration of species in acidic sulfate waters based on the Raman technique. We expect this technique to be extremely useful for fast and accurate *in-situ* detection and characterization of acid mine drainage products in mining scenarios, representing a great improvement in the current state-of-the-art of acid mine drainage description.

5. The experimental measurement of the concentration of species and the current geometry for the diffusion experiments could be notably improved. Raman spectral collection with a microRaman head could improve the signal to noise ratio in the Raman spectra and likely improve the detection limit in the experiment. As for the diffusion model, a further step we are considering is connecting the proposed model, or a revised version, to a general thermodynamic model of the equilibrium speciation and diffusion in multicomponent liquid mixtures.

6. The improvement of the routines for the processing of Raman spectra. This is required in order to advance in the automation of the operations on the Raman data and to minimize user-interaction in the process while maintaining accuracy and precision in the modeling of Raman bands' properties. On the other hand, construction of dedicated sample libraries through systematic Raman, LIBS and VNIR reflectance spectra and XRD patterns collection programs would be desirable for the autonomous identification of minerals via further versions of the software we have presented.

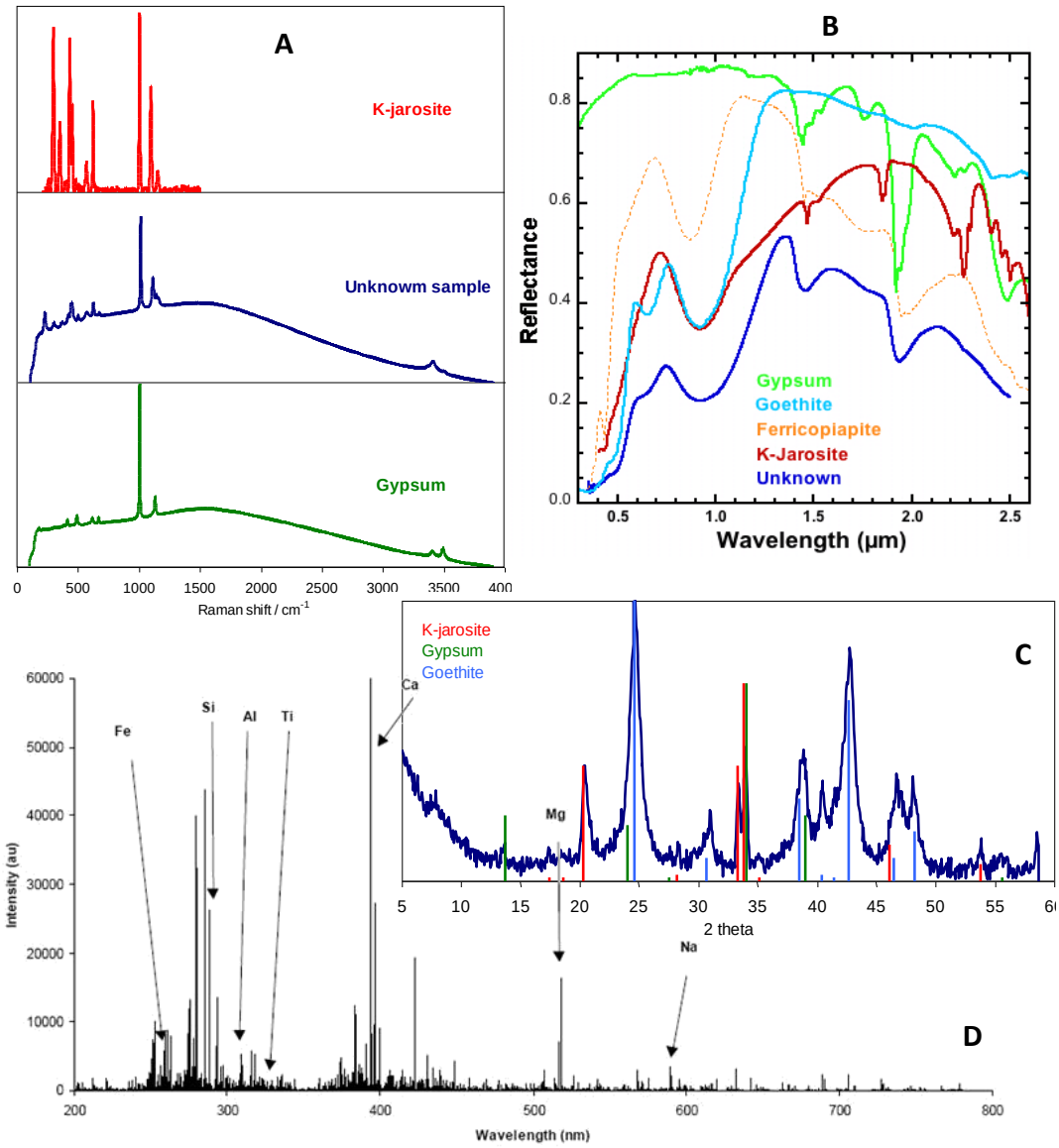

Figure 6.1. (a) Raman spectrum of an "Unknown sample" from Rio Tinto, likely composed of a mixture of gypsum and K-jarosite. (b) VNIR reflectance spectrum indicating the presence of gypsum and goethite, but also consistent with jarosite and ferricopiapite. (c) XRD pattern of the same sample identified as a mixture of gypsum, K-jarosite and goethite (FeO(OH)). The use of LIBS could yield the definitive elemental composition of the sample and determine whether potassium (K) or other cations are present or not in the sample and hence confirm the presence of K-jarosite. The LIBS spectrum of the Unknown sample was not available at the time this document was prepared. However, a LIBS spectrum of basalt is plotted in (d) as an example.

References

Allen S.K., Allen J.M., Lucas S. (1996) Concentrations of contaminants in surface water samples collected in west-central Indiana impacted by acidic mine drainage. *Environmental Geology*, 27, 34-37.

Alpers C.N., Nordstrom D.K., Spitzley J. (2003) Extreme acid mine drainage from a pyritic massive sulfide deposit: the Iron Mountain end-member. In: Jambor J.L., Blowes D.W., Ritchie A.I.M. (eds.) *Environmental Aspects of Mine Wastes*. Mineralogical Association of Canada, Short Course, (31) 407-430.

Amils R., González-Toril E., Fernández-Remolar D., Gómez R., Rodríguez N., Durán C. (2002) Interaction of the sulfur and iron cycles in the Tinto River ecosystem. *Re/Views in Environmental Science & Bio/Technology*, 1, 299-309.

Andor Technology PLC (2008). *Raman Spectroscopy*. [Online]. Available from: http://www.andor.com/learn/applications/?docID=64. [Accessed 10th April 2008].

Atakan A.K., Blass W.E., Jennings D.E. (1980) Elimination of Baseline Variations from a Recorded Spectrum by Ultra-low Frequency Filtering. *Applied Spectroscopy*, 34(3), 369-372.

Avery D. (1974) *Not on Queen Victoria's Birthday: The story of the Rio Tinto*. London, Collins.

B&W Tek Inc. (2006) *i-Raman™ Raman Spectrometer System*. [Online] Available from: http://www.bwtek.com/products/spectrometer_systems/portable_systems/i-Raman/i-Raman.html. [Accesed April 10th 2008].

Baes C.J. Mesner R.E. (1986*) The Hydrolisis of Cations*. Malabar, Krieger.

Bigham J.M., Nordstrom D.K. (2000). Iron and Aluminum Hydroxysulfates from Acid Sulfate Waters. In: Sulfate Minerals: Crystallography, Geochemistry and Environmental Significance. In: Alpers C.N., Jambor J.L., Nordstrom D.K. (eds.) *Sulfate Minerals. Crystallography, Geochemistry, and Environmental Significance* (Reviews in Mineralogy and Geochemistry, vol. 40). Washington, DC, Mineralogical Society of America, pp. 351- 403.

Bird, R.B., Stewart, W.E., Lightfoot, E.N. (2002) *Transport Phenomena*. 2nd edition. New York, John Wiley.

Bishop J.L., Pieters C.M., Burns R.G. (1993) Reflectance and Mössbauer spectroscopy of ferrihydrite-montmorillonite assemblages as Mars soil analog materials. *Geochimica et Cosmochimica Acta,* 57, 4583-4595.

Bishop J.L., Murad E. (2002) Spectroscopic and Geochemical Analyses of Ferrihydrite from Hydrothermal Springs in Iceland and Applications to Mars. In: Smellie J.L., Chapman M.G. (eds.) *Volcano-Ice Interactions on Earth and Mars.* Geological Society, Special Publication No.202, pp. 357-370.

Bishop J.L., Murad E., Lane M.D., Mancinelli R.L. (2004) Multiple techniques for mineral identification on Mars: A study of hydrothermal rocks as potential analogues for astrobiology sites on Mars. *Icarus*, 169, 331-323.

Bishop J.L., Dyar M.D., Lane M.D., Banfield J.F. (2005) Spectral identification of hydrated sulfates on Mars and comparison with acidic environments on Earth. *International Journal of Astrobiology*, 3, 275-285.

Bishop J.L., Murad E. (2005) The visible and infrared spectral properties of jarosite and alunite. *American Mineralogist*, 90, 1100-1107.

Boulter C.A. (1996) Extensional tectonics and magmatism as drivers of convection leading to Iberian Pyrite Belt massive sulphide deposits? *Journal of the Geological Society*, 153, 181-184.

BRUKER Optics Inc. (2006) *OPUS - OPtics Users Software*. [Online]. Available from: http://www.brukeroptics.com/opus/index.html. [Accessed April 10th 2008].

Burns R.G. (1994) Schwertmannite on Mars: Deposition of this oxyhydroxysulfate mineral in acidic saline meltwaters. In *Proceedings of the Lunar and Planetary Science Conference* XXV, pp. 203.

Butterworth S. (1930) On the Theory of Filter Amplifiers. *Experimental Wireless and the Radio Engineer*, 7, 536-541.

Chantry G.W. (1971). *The Raman Effect*. New York, Marcel Dekker.

Chen H., Irish D.E. (1971a) A Raman Spectral Study of Bisulfate-Sulfate Systems, II. Constitution, Equilibria, and Ultrafast Proton Transfer in Sulfuric Acid. *The Journal of Physical Chemistry*, 75(17), 2672-2681.

Chen H., Irish D.E. (1971b) A Raman Spectral Study of Bisulfate-Sulfate Systems, III. Salt Effects. *The Journal of Physical Chemistry*, 75(17), 2681-2684.

Chio C.H., Sharma S.K., Muenow D.W. (2005) Micro-Raman studies of hydrous ferrous sulfates and jarosites. *Spectrochimica Acta Part A: Molecular and Biomolecular Spectroscopy*, 61(10), 2281-2287.

Chui C.K. (1992) *An Introduction to Wavelets*. Amsterdam, Elsevier.

Clark B.C., van Hart D. (1981) The salts of Mars. *Icarus*. 45, 370.

Clark B.C., Morris R.V., McLennan S.M., Gellert R., Jolliff B., Knoll A.H., Squyres S.W., Lowenstein T.K., Ming D.W., Tosca N.J., Yeni A., Christensen P.R., Gorevan S., Brückner J., WCalvin W., Dreibus G., Farrand W., Klingelhoefer G., Waenke H., Zipfel J., Bell III J.F., Grotzinger J., McSween H.Y., Rieder R. (2005) Chemistry and mineralogy of outcrops at Meridiani Planum. *Earth and Planetary Science Letters*, 240(1), 73-94.

Clark R.J.H., Hester R.E. (eds.). (1975) *Advances in Infrared and Raman Spectroscopy*. London, Heyden.

Clegg S.L., Brimblecombe P. (1995) Application of a Multicomponent Thermodynamic Model to Activities and Thermal Properties of 0-40 mol kg^{-1} Aqueous Sulfuric Acid from < 200 to 328 K. *Journal of Chemical Engineering Data*, 40(1), 43-64.

Clegg S.L., Rard J.A., Pitzer K.S. (1994) Thermodynamic Properties of 0-6 mol kg^{-1} Aqueous Sulfuric Acid from 273.15 to 328.15 K. *Journal of the Chemical Society. Faraday Transactions*, 90(13), 1875-1894.

Clinick A. (2001) *Introducing Visual Studio for Applications*. [Online]. Available from: http://msdn2.microsoft.com/en-us/library/ms974548.aspx. [Accessed April 10th 2008].

Courreges-Lacoste G.B., Ahlers B., Perez F.R. (2007) Combined Raman spectrometer/laser-induced breakdown spectrometer for the next ESA mission to Mars. *Spectrochimica Acta Part A: Molecular and Biomolecular Spectroscopy*, 68(4), 1023-1028.

Cox R.A., Haldna U.L., Idler K.L., Yates K. (1981) Resolution of Raman spectra of aqueous sulfuric acid mixtures using principal factor analysis. *Canadian Journal of Chemistry*, 59, 2591-2598.

Dawson B.S.W., Irish D.E., Toogood G.E. (1986) Vibrational Spectral Studies of Solutions at Elevated Temperatures and Pressures. 8. A Raman Spectral Study of Ammonium Hydrogen Sulfate Solutions and the HSO_4^--SO_4^{2-} Equilibrium. *The Journal of Physical Chemistry*, 90(2), 334-341.

Dickinson R.G., Dillon R.T. (1929) The Raman spectrum of gypsum. *Proceedings of the National Academy of Sciences USA*. 15, 695-699.

Dubessy J., L'Homme T., Boiron M-C., Rull F. (2002) Determination of chlorinity in aqueous fluids using Raman spectroscopy of the stretching band of water at room temperature: application to fluid inclusions. Applied Spectroscopy, 56(1), 99-106.

Duhamel P., Vetterli M. (1990) Fast fourier transforms: A tutorial review and a state of the art. *Signal Processing*, 19(4) 259-299.

ESA Pasteur Progress Letter (2004). *Pasteur Instrument Payload for the ExoMars Rover Mission Number 4*. [Online] Accesible from: http://esamultimedia.esa.int/docs/Aurora/Pasteur_Newsletter_4.pdf. [Accessed April 10th 2008].

Ewing G.W. (1997) *Analytical Instrumentation Handbook.* New York, Marcel Dekker. pp. 39.

Fernández-Remolar D., Morris R.V., Gruener J.E., Amils R., Knoll A.H. (2005) *Earth and Planetary Science Letters*, 240, 149-167.

Friesen W.I., Michaelian K.H. (1985) Deconvolution in the Frequency Domain. *Applied Spectroscopy*, 39(3), 484-490.

Friesen W.I., Michaelian K.H. (1988) Fourier Deconvolution of Raman spectra. *Canandian Journal of Spectroscopy*, 33(2), 29-34.

Frost R.L., Kloprogge, J.T., Williams P.A., Leverett P. (2000) Raman microscopy of some natural pseudo-alums: halotrichite, apjohnite and wupatkiite, at 298 and 77 K. *Journal of Raman Spectroscopy*, 31(12), 1083-1087.

Frost R.L., Weier M.L., Kloprogge J.T., Rull F., Martinez-Frias J. (2005) Raman spectroscopy of halotrichite from Jaroso, Spain. *Spectrochimica Acta Part A: Molecular and Biomolecular Spectroscopy*, 62(1-3), 176-180.

Frost R.L., Wills R., Weier M.L., Martens W., Mills S. (2006a) A Raman spectroscopic study of selected natural jarosites. *Spectrochimica Acta Part A: Molecular and Biomolecular Spectroscopy,* 63(1), 1-8.

Frost R.L., Wills R., Kloprogge J.T., Martens W. (2006b) Thermal decomposition of ammonium jarosite $(NH_4)Fe_3(SO_4)_2(OH)_6$. *Journal of Thermal Analysis and Calorimetry*, 84(2), 489–496.

G.R.Landsberg, L.Mandelstam (1928) Über eine neue Erscheinung in der Lichtzerstreuung in Krystallen. *Naturwissenschaften*, 16(33), 653.

Gabelmann-Gray L., Fenichel H. (1979) Holographic interferometric study of liquid diffusion. *Applied Optics*, 18(3), 343-345.

Gendrin A., Mangold N., Bibring J-P., Langevin Y., Gondet B., Poulet F., Bonello G., Quantin C., Mustard J., Arvidson R., LeMouelic S. (2005) Sulfates in Martian Layered Terrains: The OMEGA/Mars Express View. *Science*, 307, 1587-1591.

Gilson T.R., Hendra P.J. (1972) *Laser Raman Spectroscopy*. London, Wiley-Interscience.

González-Toril E., Llobet-Brossa E., Casamayor E.O., Amann R., Amils R. (2003) Microbial Ecology of an Extreme Acidic Environment, the Tinto River. *Applied and Environmental Microbiology*, 69(8), 4853-4865.

Griffiths P.R., Pariente G.L. (1986) Introduction to spectral deconvolution, *Trends in Analytical Chemistry*, 5(8), 209-215.

Hester R.E., Plane R.A. (1964) Solvation of Metal Ions in Aqueous Solutions : the Metal-Oxygen Bond. *Inorganic Chemistry*, 3(5), 768-769.

inXitu Inc. (2008) *Rock and Mineral Analyzer.* [Online] Available from: http://www.inxitu.com/html/product_services.htm. [Accessed April 10th 2008].

Irish D.E., Chen H. J. (1970) Equilibria and Proton Transfer in the Bisulfate-Sulfate System. *The Journal of Physical Chemistry*, 74(21), 3796-3801.

Jamieson H.E., Robinson C., Alpers C.N., Nordstrom D.K., Poustovetov A., Lowers H.A. (2005) The composition of coexisting jarosite-group minerals and water from the Richmond Mine, Iron Mountain, California. *The Canadian Mineralogist*, 43(4), 1225-1242.

Kaiser Optical Systems Inc. (2008). HoloSpec *f*/1.8i Holographic Imaging Spectrograph. [Online]. Available from: http://www.kosi.com/spectrographs/holospeci.html. Accessed April 10th 2008].

Kauppinen J.K., Moffatt D.J., Cameron D.G., Mantsch H.H. (1981a) Noise in Fourier self-deconvolution. *Applied Optics*, 20(10), 1866-1879.

Kauppinen J.K., Moffat D.J., Mantsch H.H., Cameron D.G. (1981b) Fourier self-deconvolution: A method for resolving intrinsically overlapped bands. *Applied Spectroscopy*, 35(3), 271-276.

Kinkel A.R., Hall W.E., Albers, J.P. (1956) Geology and base-metal deposits of West Shasta copper-zinc district, Shasta County, California. *United States Geological Survey, Professional Paper* 285.

Klingelhöfer G., Morris R.V., Bernhardt B., Schröder C., Rodionov D.S., de Souza Jr. P.A., Yen A., Gellert R., Evlanov E.N., Zubkov B., Foh J., Bonnes U., Kankeleit E., Gütlich P., Ming D.W., Renz F., Wdowiak T., Squyres S.W., Arvidson R.E. (2004) Jarosite and Hematite at Meridiani Planum from Opportunity's Mössbauer Spectrometer. *Science*, 306, 1740-1745.

Knight A.K., Scherbarth N.L., Cremers D.A., Ferris M.J. (2000) Characterization of Laser-Induced Breakdown Spectroscopy (LIBS) for Application to Space Exploration. *Applied Spectroscopy*, 54(3), 331-340.

Knoll A.H., Carr M., Clark B., des Marais D.J., Farmer J.D., Fischer W.W., Grotzinger J.P., McLennan S.M., Malin M., Schröder C., Squyres S., Tosca N.J., Wdowiak T. (2005) An astrobiological perspective on Meridiani Planum. *Earth and Planetary Science Letters*, 240, 179-189.

Knopf D.A., Luo B.P., Krieger U.K., Koop T. (2003). Thermodynamic Dissociation Constant of the Bisulfate Ion from Raman and Ion Interaction Modeling Studies of Aqueous Sulfuric Acid at Low Temperatures. *Journal of Physical Chemistry A*, 107(21), 4322-4332.

Knopf D.A., Luo B.P., Krieger U.K., Koop T. (2005). Reply to “Comment on the ‘Thermodynamic Dissociation Constant of the Bisulfate Ion from Raman and Ion

Interaction Modeling Studies of Aqueous Sulfuric Acid at Low Temperatures'". *Journal of Physical Chemistry A*, 109(11), 2707-2709.

Landsberg G.R., Mandelstam L.I. (1928) Eine neue Erscheinung bei der Lichtzerstreuung in Krystallen. *Naturweissen*, 16, 557-558.

Lane M.D.,Dyar M.D., Bishop J.L. (2004) Spectroscopic evidence for hydrous iron sulfate in the Martian soil. *Geophysical Research Letters*, 31, L19702.

Lazaroff N., Sigal W., Wasserman A. (1982) Iron Oxidation and Precipitation of Ferric Hydroxysulfates by Resting Thiobacillus ferrooxidans Cells. *Applied and Environmental Microbiology*, 43(4), 924-938.

Leistel J.M., Marcoux E., Thiéblemont D., Quesada C., Sánchez A., Almodóvar G.R., Pascual E., Sáez R. (1988) The volcanic-hosted massive sulphide deposits of the Iberian Pyrite Belt Review and preface to the Thematic Issue. *Mineralium Deposita*, 33(1-2), 2-30.

Lietzke M.H., Stoughton R.W., Young T.F. (1961) The bisulfate acid constant from 25 to 225° as computed from sulubiity data. *The Journal of Physical Chemistry*, 65, 2247-2249.

Lifshitz E.M., Landau L.D. (1980) *Course of theoretical physics, Volume V: Statistical Physics*. 3rd edition. Butterworth-Heinemann.

Long D.A. (1977). *Raman Spectroscopy*.U.K., McGraw-Hill.

López-Archilla A.I., Marín I., Amils R. (1993) Bioleaching and interrelated acidophilic microorganisms from Río Tinto, Spain. *Geomicrobiology Journal*, 11, 223–233.

López–Archilla A.I., Marin I., Amils R. (2001) Microbial Community Composition and Ecology of an Acidic Aquatic Environment: The Tinto River, Spain. *Microbial Ecology*, 41, 20-35.

Magini M. (1979) Solute structuring in aqueous iron (III) sulphate solutions. Evidence for the formation of iron(III)-sulphate complexes. *The Journal of Physical Chemistry*, 70(1), 317-324.

Majzlan J., Myneni S.C.B. (2005) Speciation of Iron and Sulfate in Acid Waters: Aqueous Clusters to Mineral Precipitates. *Environmental Science and Technology*, 39(1), 188-194.

Marquardt D.W. (1963) An algorithm for least-squares stimation of nonlinear parameters. *Journal of the Society for Industrial and Applied Mathematics*, 11(2), 431-441.

Mellado D., González-Clavijo E., Tornos F., Conde C. (2006) Geología y estructura de la Mina de Río Tinto (Faja Pirítica Ibérica, España). *GEOGACETA*, 40, 231-234.

Morton K.W., Mayers D.F. (2005) *Numerical Solution of Partial Differential Equations, An Introduction*. Cambridge, University Press.

Mossier-Boss P.A., Lieberman S.H. (2000) Detection of Nitrate and Sulfate Anions by Normal Raman Spectroscopy and SERS of Cationic-Coated, Silver Substrates. *Appl. Spectrosc.,* 54(8), 1126-1135.

Myhre C.E., Christensen D.H., Nicolaisen F.M., Nielsen C.J. (2003) Spectroscopic Study of Aqueous H2SO4 at Different Temperatures and Compositions: Variations in Dissociation and Optical Properties. *Journal of Physical Chemistry A*, 107, (12), 1979-1991.

Myneni S.C.B. (2000) X-ray and Vibrational Spectroscopy of Sufate in Earth Materials. In: Alpers C.N., Jambor J.L., Nordstrom D.K. (eds.) *Sulfate Minerals. Crystallography, Geochemistry, and Environmental Significance* (Reviews in Mineralogy and Geochemistry, vol. 40). Washington, DC, Mineralogical Society of America, pp. 113-172.

Nakamoto K. (1997) *Infrared and Raman Spectra of Inorganic and Coordination Compounds*. 5th edition. New York, John Wiley and Sons.

NASA Ames Research Center (2005) *Mars Astrobiology Research and Technology Experiment*. [Online] Accesible from: http://marte.arc.nasa.gov. [Accessed April 10th 2008].

NASA News Release 04-398. (2004) *NASA Selects Investigations for the Mars Science Laboratory*. [Online] Accesible from: http://www.nasa.gov/home/hqnews/2004/dec/HQ_04398_MSL_Selections.html. [Accessed April 10th 2008].

Nordstrom D.K. (1982) Aqueous pyrite oxidation and the consequent formation of secondary iron minerals. In: Kittrick J.A., Fanning D.S., Hossner L.R. (eds.) *Acid Sulfate Wathering*. Soil Science Society of America Special Publication no. 10, pp. 37-56.

Nordstrom D.K., Southam G. (1997) Geomicrobiology of Sulfide Mineral Oxidation. In: Banfield J.F., Nealson K.H. (eds.) *Geomicrobiology: Interactions between Microbes and Minerals* (Reviews in Mineralogy Vol. 35). Washington, DC, Mineralogical Society of America, pp. 361-390.

Nordstrom D.K., Alpers C.N. (1999a) Geochemistry of acid mine waters. In: Plumlee G.S., Logsdon M.J. (eds.) *The Environmental Geochemistry of Mineral Deposits. Part A. Processes, methods and health issues*. Reviews in Economic Geology, 6A, pp. 133-160.

Nordstrom DK, Alpers CN. (1999b) Negative pH, efflorescent mineralogy, and consequences for environmental restoration at the Iron Mountain Superfund site, California. In: Smith J.V., Buseck P.R., Ross M. (eds.), *Geology, Mineralogy, and Human Welfare*. Proceedings of the National Academy of Sciences U.S.A., 96, 3455-3462.

Nordstrom D.K., Alpers, C.N., Ptacek C., Blowes D.W. (2000) Negative pH and Extremely Acidic Mine Waters from Iron Mountain, California. *Environmental Science and Technology,* 34(2), 254-258.

Nordstrom D.K. (2000) Advances in the hydrogeochemistry and microbiology of acid mine waters. *International Geology Review*, 42, 499-515.

Pearson G.A. (1987) Optimization of Gaussian resolution enhancement. *Journal of Magnetic Resonance*, 74(3), 541-545.

Perry R.H., Green D.W. (1997) *Perry's Chemical Engineers' Handbook*. 7th edition. McGraw-Hill Professional.

Press W.H., Teukolsky S.A., Vetterling W.T., Flannery B.P. (1992) *Numerical Recipes in C: The Art of Scientific Computing*. 2nd edition. Cambridge University Press.

Rader C.M., Brenner N.M. (1976) A new principle for fast Fourier transformation. *IEEE Transactions on Acoustics, Speech, and Signal Processing*, vol. ASSP-24(3), 264-266.

Raman C.V., Krishnan K.S. (1928) A new type of Secondary Radiation. *Nature*, 121, 501-502.

Reardon E.J. Beckie R.D. (1987) Modelling chemical equilibria of acid mine-drainage: The FeSO4-H2SO4-H2O system. *Geochimica et Cosmochimica Acta*, 51, 2355-2368.

Rieder R., Gellert R., Anderson R.C., Brückner J., Clark B.C., Dreibus G., Economou T., Klingelhöfer G., Lugmair G.W., Ming D.W, Squyres S.W., d'Uston C., Wänke H., Yen A., Zipfel J. (2004) Chemistry of Rocks and Soils at Meridiani Planum from the Alpha Particle X-ray Spectrometer. *Science*, 306, 1746-1749.

Rodriguez A., Sobron F., Rull F., Prieto A.C., Edwards, H.G.M. (1995) Mass diffusion transport studies of lithium sulfate in aqueous solutions using Raman spectroscopy. *Applied Spectroscopy*, 49(8), 1131-1136.

Ross S.D. (1974) Sulphates and other oxy-anions of group VI. In: Farmer V.C. (ed.) *The Infrared Spectra of Minerals*. London, Mineralogical Society, pp. 423-444.

Rull F., Jimenez J., Sobron F., Rodriguez A. (1993) Intensity and band profile of Raman spectra of optoelectronic materials. In: Marshall J.M., Kirov N. (eds.) *Electronic and Optoelectonic Materials for the 21st Century*. Singapore, World Science Pub., pp.228-247.

Rull F., Sobron F., Nielsen O.F. (1995) Dependence on concentration and temperature of the dynamics of SO42- in LiSO4, NaSO4 and K2SO4 aqueous solutions studies by Raman spectroscopy. *Journal of Raman spesctroscopy*, 26, 663-668.

Rull F., Medina J., Sansano A., Sanz A., Sobrón F., Sobrón P. (2003) A Raman spectral study of acidic aqueous solutions and associated minerals in Río Tinto (Spain). In: Sawaya-Lacoste H. (ed.). *Proceedings of the 3rd European Workshop on Exo/Astrobiology - Mars: The Search for Life, Madrid, Spain*. Noordwijk, The Netherlands: ESA Publication Division. ESA SP-545: 123-126.

Runnells D.D., Shepard T.A., Angino E.E. (1992) Metals in water. Determining natural background concentrations in mineralized areas. *Environmental Science and Technology*, 26, 2316–2322.

Sarrazin P.C., Brunner W., Blake D.F., Steele A., Midtkandal I., Amundsen, H. (2007) Field Study of Mars Analog Materials in Spitsbergen (Norway) Using a Portable X-ray Diffraction Instrument. *American Geophysical Union Fall Meeting 2007*, abstract #P31C-0548.

Sasaki K., Tanaike O., Konno H. (1998) Distinction of jarosite -group compounds by Raman spectroscopy. *The Canadian Mineralogist*, 36(5), 1225-1235.

Savitzsky A., Golay M.J.E. (1964) Smoothing and Differentiation of Data by Simplified Least Squares Procedures. *Analytical Chemistry*, 36(8), 1627-1639.

Serrano, J., Viñas, L., López Fernández, A.J. (1995) Proyecto de regeneración de los ríos Tinto y Odiel (Huelva). *Tecnoambiente*, 53, 53–56.

Sharma S.K., Chio C.H., Muenow D.W. (2006) Raman spectroscopic investigation of ferrous sulfate hydrates. In *Proceedings of the Lunar and Planetary Science Conference* XXXVII, Abstract no. 1078.

Sharma S.K., Misra A.K., Lucey P.G., Wiens R.C., Clegg S.M. (2007) Combined remote LIBS and Raman spectroscopy at 8.6 m of sulfur-containing minerals, and minerals

coated with hematite or covered with basaltic dust. *Spectrochimica Acta Part A: Molecular and Biomolecular Spectroscopy*, 68(4), 1036-1045.

Sharma S.K. (2007) New trends in telescopic remote Raman spectroscopic instrumentation. *Spectrochimica Acta Part A: Molecular and Biomolecular Spectroscopy*, 68(4), 1008-1022.

Singer P.C., Stumm W.W. (1970) Acidic Mine Drainage: The Rate-Determining Step. *Science*, 167, 1121-1123.

Sobron P. (2003) *Caracterización por espectroscopía Raman de los procesos de difusión de ácido sulfúrico en agua*. M. Sci. Dissertation. University of Valladolid.

Sobron P., Eide U.M., Nielsen C.J., Rull F., Sobron F., Sanz A., Medina J. Diez J.L. (2006) Diffusion Phenomena in the System Sulfuric Acid-Water: Application to the Extreme Environment of Tinto River, Spain. *International Symposium on Solubility Phenomena 2006*, abstract #AV12.

Sobron P., Rull F., Sobron F., Sanz A., Medina J., Nielsen C.J. (2007a) Raman spectroscopy of the system iron(III)-sulfuric acid-water: an approach to Tinto River's (Spain) hydrogeochemistry. *Spectrochimica Acta Part A: Molecular and Biomolecular Spectroscopy*, 68(4), 1138-1142.

Sobron P., Rull F., Sobron F., Sanz A., Medina J., Nielsen C.J. (2007b) Modeling the physico-chemistry of acid sulfate waters through Raman spectroscopy of the system $FeSO_4$-H_2SO_4-H_2O. *Journal of Raman Spectroscopy*, 38(9), 1127-1132.

Sobrón P., Sobrón F., Sanz A., Rull F. (2008a) Raman signals processing software for automated identification of mineral phases and biosignatures on Mars. *Applied Spectroscopy*, 62(4), 364-370.

Sobron P., Sanz A., Acosta T., Rull F. (2008b) A Raman spectral study of stream waters and efflorescent salts in Rio Tinto, Spain. *Spectrochimica Acta Part A: Molecular and Biomolecular Spectroscopy*. Under review.

Tepavitcharova S., Balarex Chr., Rull F., Rabadjieva D., Iliev A. (2005) Raman spectroscopic studies of ion association in the Na^{+}, Mg^{2+}/Cl^{-}, SO_4^{2-}/H_2O system. *Journal of Raman spectroscopy*, 36, 891-897.

Thermo Fisher Scientific Inc. (2008). *Grams Suite*. [Online]. Available from: http://www.thermo.com/eThermo/CMA/PDFs/Product/productPDF_24179.pdf. [Accessed April 10th 2008].

U.S. Environmental Protection Agency. Technical Document: Acid Mine Drainage Prediction. 1994.

Wang A., Freeman J.J., Jolliff B.L., Chou I.M. (2006) Sulfates on Mars: A systematic Raman spectroscopic study of hydration states of magnesium sulfates. *Geochimica et Cosmochimica Acta*, 70, 6118–6135.

Wasserman, P.D. (1989) *Neural Computing: Theory and Practice*. New York, Van Nostrand Reinhold.

Wiens R.C., Sharma S.K., Thompson J., Misra A., Lucey P.G. (2005) Joint analyses by laser-induced breakdown spectroscopy (LIBS) and Raman spectroscopy at stand-off distances. *Spectrochimica Acta Part A: Molecular and Biomolecular Spectroscopy*, 61(10), 2324-2334.

Woodward L.A. (1967) *General Introduction to Raman spectroscopy. Theory and Practice*. New York, Plenum.

Young T.F., Maranville L.F., Smith H.M. (1959) Raman spectral investigations of ionic equilibria in solutions of strong electrolytes. In: Hammer W.J. (ed.) *The structure of Eloctrolytic Solutions*. New york, Wiley, pp. 35-63.

Appendix A

publications related to this thesis

In peer-reviewed journals

- Sobron P., Sobron F., Eide U.M., Nielsen C.J., Rull F. (draft) Model-based investigations on the diffusion properties of sulfuric acid into water by Raman spectroscopy. *Journal of Physical Chemistry.*

- Sobron P., Bishop J.L., Blake D.F., Chen B., Rull F. (draft) Raman, VNIR reflectance and XRD analysis of efflorescent sulfates from Rio Tinto (Spain). *International Journal of Astrobiology*.

- Sobron P. and Alpers C.N. (draft) Raman spectroscopy of sulfate efflorescences from Iron Mountain Superfund Site, California. *Journal of Raman spectroscopy.*

- Sobron P., Sanz A., Acosta T., Rull F. (2008) A Raman spectral study of stream waters and efflorescent salts in Rio Tinto, Spain. *Spectrochimica Acta Part A*. Under review.

- Sobron P., Sobron F., Sanz A., Rull F. (2008) Raman signals processing software for automated identification of mineral phases and biosignatures on Mars. *Applied Spectroscopy*, 62(4), 364-370.

- Sobron P., Rull F., Sobron F., Sanz A., Medina J., Nielsen C.J. (2007) Modeling the physico-chemistry of acid sulfate waters through Raman spectroscopy of the system $FeSO_4$-H_2SO_4-H_2O. *Journal of Raman Spectroscopy,* 38, 1127-1132.

- P. Sobron, F. Rull, F. Sobron, J. Medina, A. Sanz, C.J. Nielsen (2007) Raman spectroscopy of the system iron(III)-sulfuric acid-water: an approach to Tinto River's (Spain) hydrogeochemistry. *Spectrochimica Acta Part A,* 68, 1138-1142.

In international conference proceedings

- Sobron P., Rull F., Sobron F., Medina J., Sanz A. (2007) Characterization of Tinto River's (Spain) aqueous solutions by Raman spectroscopy. Proceedings of the 6th European Workshop on Astrobiology, Lyon, France. *International Journal of Astrobiology,* 6(1), 59-87.

- Sobron P., Meide U., Nielsen C.J., Rull F., Sobron F., Sanz A., Medina J., Diez J.L. (2006). Modeling the Tinto River water: diffusion of molecular species in the system sulfuric acid-water by Raman spectroscopy. Proceedings of the Astrobiology Science Conference (AbSciCon) 2006, Washington D.C., USA. *Astrobiology*, n(1), 174-221

Abstracts

- Bishop J.L, Alpers C.N., Coleman M.L., Sobron P., Lane M.D., Darby Dyar M., Schiffman P. (2008) Sulfates on Mars: Comparison with Spectral Properties of Analog Sites. *Goldschmidt 2008*. Vancouver, Canada.

- Sobron P., Sanz A., Alpers C.N., Rull F. (2008) Raman investigation into sulfate-bearing minerals from Iron Mountain, California, U.S.A. *GEORAMAN'08: 8th International Conference on Raman Spectroscopy Applied to the Earth Sciences - Sensu Latu.* Ghent, Belgium.

- Sansano A., Sobron P., Medina J., Sanz A., Rull F. (2008) Mineralogy of the evaporate sediments in Rio Tinto banks. An initial approximation through simulation. *GEORAMAN'08: 8th International Conference on Raman Spectroscopy Applied to the Earth Sciences - Sensu Latu.* Ghent, Belgium.

- Sobron P., Sanz A., Acosta T., Rull F. (2008). Hydrated sulfates on the Rio Tinto (Spain) Martian analog in association with acidic waters. *Mars Water Cycle Workshop*. Paris, France.

- Sobron P., Sanz A., Medina J., Sobron F., Rull F., Nielsen C.J. (2007) Raman spectral characterization of a terrestrial scenario with implications for Mars exploration: Rio Tinto, Spain. *European Mars Science and Exploration Conference: Mars Express & ExoMars*. ESTEC, Noordwijk, The Netherlands.

- Sobron P., Rull F., Sobron F., Sanz A., Acosta T. (2007) Practical use of LIBS and Raman spectroscopy in Exo/Astrobiology: Rio Tinto (SW Spain) environment. *4th AbGradCon @ Bioastronomy 2007*. San Juan, Puerto Rico.

- Sobron P., Nielsen C.J., Sanz A. (2007) Characterization of the chemical constituents of stream water and its associated precipitates and efflorescent minerals in Rio Tinto (Huelva, Spain). *2nd International Workshop Exploring Mars and its Earth Analogues*. Trento, Italy.

- Sobron P., Rull F., Sobron F. Sanz A. Acosta, T. (2007) Remote Raman/LIBS instrument for the characterization of Mars terrestrial analogues. *2nd International Workshop Exploring Mars and its Earth Analogues*. Trento, Italy.

- Sobron P., Eide U.M., Nielsen C.J., Rull F., Sobron F., Sanz A., Medina J., Diez J.L. (2006) Diffusion phenomena in the system sulfuric acid-water: application to the extreme environment of Tinto River, Spain. *12th International Symposium on Solubility Phenomena and Related Equilibrium Processes*. Freiberg, Germany.

- Sobron P., Sobron F., Sanz A., Rull F. (2006) Modeling Tinto River (Spain) hydrogeochemistry. II. Speciation of iron-III in acid solutions by Raman spectroscopy. *GEORAMAN'06: 7th Internacional Conference on Raman Spectroscopy Applied to Earth and Planetary Sciences*. Almuñécar, Spain.

- Sobron P., Eide U.M., Nielsen C.J., Sobron F. (2006) Modeling Tinto River (Spain) hydrogeochemistry. I. Diffusion of molecular species in the system sulfuric acid-

water by Raman spectroscopy. *GEORAMAN'06: 7th Internacional Conference on Raman Spectroscopy Applied to Earth and Planetary Sciences*. Almuñécar, Spain.

- Sobron P., Sanz A., Rull F., Sobron F., Medina J. (2005) Raman spectroscopy applied to the study of the aqueous acid solutions of Rio Tinto (Spain). *Primer encuentro científico de la Sociedad Española de Mineralogía y la Sociedad Francesa de Mineralogía y Cristalografía*. Biarritz, France.

- Sobron P., Sanz A., Rull F., Sobron F., Medina J. (2005) A Raman spectral and thermodynamic study of aqueous iron(II) sulfate solutions. Application to the acidic solutions of Rio Tinto (Spain). *2nd Astrobiology Graduate Conference*. La Jolla, California.

- Sobron P., Sanz A., Rull F., Sobron F., Medina J. (2005) Estudio espectroscópico y termodinámico del equilibrio sulfúrico-sulfato en solución acuosa: aplicación a las soluciones ácidas de Río Tinto (Huelva). *XXV REUNIÓN DE LA SOCIEDAD ESPAÑOLA DE MINERALOGÍA*. Alicante, Spain.

Young Investigator award from the Spanish Society of Mineralogy

- Rull F., Sobron P., Sanz A., Sobron F. (2004) Espectroscopía Raman aplicada al estudio de las soluciones acuosas de Río Tinto. *XXIV Reunión de la Sociedad Española de Mineralogía*. Cuenca, Spain.

- Rull F., Sanz A., Sobron F., Sobron P, Medina J. (2004) Spectroscopic Raman study of acidic aqueous solutions in Rio Tinto (Spain). *11th International Symposium on Solubility Phenomena and Related Equilibrium Processes*. Aveiro, Portugal.

- Rull F., Medina J., Sansano A., Sanz A., Sobron F., Sobron P. (2003) A Raman spectral study of acidic aqueous solutions and associated minerals in Río Tinto (Spain). *3th European Workshop on Exo/Astrobiology*. Madrid, Spain.

Appendix B

conclusiones y líneas futuras

B.1. Resumen y conclusiones

En el transcurso de esta tesis doctoral hemos caracterizado soluciones acuosas sintéticas que se reproducen las condiciones extremas de las aguas de Río Tinto. Hemos analizado muestras naturales de agua del río basándonos en los resultados obtenidos mediante la técnica Raman con los sistemas sintéticos, en concreto las relaciones de equilibrio y especiación, y las propiedades de transporte de materia. También hemos caracterizado eflorescencias ricas en sulfato de Río Tinto utilizando la espectroscopía Raman como herramienta fundamental, además de otras técnicas complementarias como la reflectancia en el infrarrojo cercano y el visible (VNIR) y la difracción de rayos-X. Hemos desarrollado rutinas de procesado automático de datos en lenguaje VBA para obtener la máxima información de los espectros Raman y minimizar la contribución del ruido y otras interferencias en los espectros.

El sistema sulfato de hierro(II)-ácido sulfúrico-agua se produce cuando las aguas subterráneas fluyen a través de grietas en zonas con alto contenido en azufre. Dicho sistema es uno de los componentes principales del drenaje ácido de mina, y es la causa directa de la acidificación de los ríos relacionados con minas. En esta tesis hemos logrado una cuantificación precisa de las concentraciones de las especies presentes en el sistema hierro(II)-ácido sulfúrico-agua, y hemos caracterizado los equilibrios en el mismo en función del producto de coeficientes de actividad. Esto cobra gran importancia a la hora de establecer modelos físico-químicos de aguas ácidas ya que este sistema en particular tiene un comportamiento muy alejado de la idealidad. Además, la espectroscopía Raman ha permitido corroborar resultados previamente publicados sobre la formación de complejos de hierro(II) hexahidratado dentro del mismo sistema. Se han calculado los productos de coeficientes de actividad como función de la concentración de sulfato de hierro(II), siendo la concentración de hierro mayor que la de las aguas de Río Tinto. Hemos obtenido una relación logarítmica entre el producto de coeficientes de actividad y la concentración de sulfato de hierro(II) que da idea de la fuerte no-idealidad del sistema estudiado y permite asimismo extrapolar valores más allá de los límites de concentración de sal utilizados en este trabajo. A

modo de ejemplo podemos citar el trabajo de Nordstrom *et al.* (2000) en el que se recogen concentraciones de hasta 1.45 mol/kg de hierro(II) en las aguas ácidas de Richmond Mine en Iron Mountain.

Otro de los sistemas que cobra especial importancia en el marco del drenaje ácido de mina es el sistema hierro(III)-ácido sulfúrico-agua. El estudio la especiación iónica en este sistema mediante espectroscopía Raman revela la existencia de interacciones sulfato-hierro(III) en la esfera interior de Fe^{3+} a través de oxígenos que provienen de las unidades de sulfato, y en la esfera exterior a través de enlaces de hidrógeno. La técnica Raman proporciona una gran precisión y repetibilidad en las medidas, lo que es fundamental en los análisis cualitativos y cuantitativos. En particular, las vibraciones moleculares de los complejos de hierro(III) quedan determinadas por longitudes de onda específicas en los espectros Raman, de modo que los cambios en intensidad y anchura en las bandas Raman asociadas a las vibraciones moleculares de esos compuestos pueden ser cuantificados fácilmente.

El estudio de los sistemas mencionados en los párrafos anteriores nos ha permitido conocer la influencia de la concentración de sal y ácido en las intensidades, en las anchuras y en los perfiles de las bandas asociadas a las moléculas de sulfato, bisulfato y agua. Hemos detectado las signaturas espectrales de estas estructuras moleculares en muestras selectas de agua de Río Tinto, y a partir de los espectros Raman de estas muestras acuosas naturales hemos calculado las concentraciones relativas de sulfato y bisulfato, las especies predominantes en las aguas ácidas asociadas a la actividad minera.

Las áreas relacionadas con antiguos trabajos mineros, como Río Tinto, contienen grandes cantidades de minerales ricos en azufre y se caracterizan por agua muy ácidas. La caracterización de los constituyentes de las aguas en sitios contaminados con drenaje ácido de mina es muy importante porque se necesita para diseñar estrategias de tratamiento. Además, una detección precoz de las especies iónicas asociadas con las aguas ácidas sulfúricas puede ser de gran ayuda para predecir un potencial drenaje ácido de mina. Con este propósito, hemos utilizado la espectroscopía Raman *ex-situ*

como medio de caracterización de la hidrogeoquímica del área d Río Tinto. Sin embargo, actualmente estamos considerando la posibilidad de usar espectrómetros Raman portátiles para análisis *in-situ*, ya que los espectros preliminares obtenidos *in-situ* (Rull *et al.*, 2003) justifican la importancia de la espectroscopía Raman como herramienta potencial de caracterización del entrono de Río Tinto, así como de cualquier área que contenga drenaje ácido de mina.

Hemos estudiado la difusión de especies moleculares en el sistema ácido sulfúrico-agua mediante espectroscopía Raman, y hemos establecido un modelo químico-termodinámico de las propiedades de transporte de materia de las especies con parámetros optimizados. Se ha demostrado que la no-idealidad de este sistema juega un papel clave en las propiedades de transporte, las cuales sin embargo se han descrito en términos de un modelo de difusión para el sistema multicomponente. En resumen, los coeficientes de difusión no son constantes (son constantes en sistemas ideales), sino que son función de la concentración de las especies en solución. La concepción del modelo permite su adaptación a cualquier sistema multicomponente siempre que se conozcan los equilibrios entre especies. Se ha demostrado que la espectroscopía Raman puede proporcionar los medios para obtener la especiación y las concentraciones de las especies en sistemas multicomponente, y por tanto la medida Raman de las propiedades de difusión basadas en modelos se muestra como es una técnica robusta y precisa.

En esta tesis se han analizado sales eflorescentes de sulfato (recogidas en los mismos enclaves que las muestras acuosas) de Río Tinto. Se han encontrado las signaturas espectrales de varias formas de sulfatos de hierro, que se han usado para la identificación de las muestras. En las eflorescencias se han encontrado yeso y sulfatos ferrosos y férricos.

También se han caracterizado eflorescencias de sulfato de Iron Mountain formadas a partir de aguas extremadamente ácidas vía drenaje ácido de mina. Se han encontrado compuestos como yeso, ferricopiapita, melanterita, coquimbita y voltaíta. Sin embargo los espectros, al igual que los espectros de los sulfatos de Rio Tinto, son

difíciles de analizar, ya que muestran bandas superpuestas y hombros que generalmente son debidos la presencia de sulfatos e hidróxidos no identificados en la matriz principal del mineral.

No se han tomado espectros *in-situ*, aunque los últimos avances en óptica, láseres y detectores han permitido el desarrollo de instrumentos de campo compactos para análisis *in-situ*. En particular, la técnica Raman ha experimentado avances espectaculares en cuanto a portabilidad y robustez, de modo que hoy en día ya se comercializan instrumentos Raman ligeros, pequeños y compactos para aplicaciones de campo (*e.g.* B&W Tek Inc., 2006). No nos cabe duda que la técnica Raman se convertirá en una herramienta para análisis rutinarios de campo, y esperamos que el futuro trabajo de campo se beneficie en gran medida de los resultados de la investigación que se presentan en esta tesis.

Se ha utilizado un conjunto de técnicas en el laboratorio para investigar una serie de muestras de Río Tinto. Hemos mostrado los resultados de los espectros de reflectancia en el visible e infrarrojo-cercano que pueden ser comparados con las imágenes hiperespectrales de Marte de los espectrómetros CRISM y OMEGA, patrones de difracción de rayos-X que se pueden comparar con el instrumento Chemin de MSL, y espectros Raman que se esperan de ExoMars. Se ha detectado una gran variedad de fases minerales en las muestras que incluye K y Na-jarosita, yeso, goetita, copiapita y ferricopiapita. La difracción de rayos-X ha detectado cuarzo en algunas de las muestras, no así las otras técnicas.

Es probable que el sustrato de roca bajo las capas de sulfato evaporadas contenga cristales de cuarzo. Mientras que la reflectancia VNIR y el Raman, como técnicas no destructivas, consiguen información sólo de las capas más superficiales, el polvo usado para los análisis de rayos-X contenía granos de esas capas además de la roca substrato, y por tanto la información de esta última se incluye también en los patrones de difracción. La reflectancia permite identificar varios compuestos de sulfato en cada muestra, mientras que la difracción, y en especial el Raman sólo son capaces de detectar una o dos fases diferentes.

La espectroscopía VNIR ha demostrado ser muy potente para la caracterización de agua y aniones en minerales. Sin embargo el agua es un absorbente importante y puede llegar a enmascarar la reflectancia de las unidades cation-hidroxilo (M-OH, donde *M* representa un catión metálico). Es por esto que la identificación de las características espectrales asociadas a minerales hidratados en los espectros VNIR puede ser ambigua en ciertas ocasiones. Una de las ventajas de la espectroscopía Raman es que el agua es una unidad que apenas produce dispersión de fotones, y en consecuencia el stretching de hidroxilos en las unidades M-OH se puede resolver mejor, y por tanto se consigue una asignación de bandas más precisa. En cualquier caso, una de las grandes dificultades asociadas con los compuestos de sulfato del campo es que se encuentran a menudo en un estado poco cristalino, haciendo su análisis mediante técnicas de difracción muy complicado. Se puede emplear la difracción de rayos X para investigar estos compuestos, pero los patrones de difracción estarán dominados por las fases altamente cristalinas presentes en la matriz mineral, así como el cuarzo en el caso de las muestras de este estudio.

Las técnicas de espectroscopía vibracional suelen permitir una mejor detección de los sulfatos. Sin embargo, la adquisición e interpretación de espectros Raman es a menudo difícil en materiales poco cristalinos. La microespectroscopía Raman permite en cierto modo solventar esta dificultad y analizar spots del orden de las 25-50 micras de diámetro. La desventaja es que al analizar áreas tan pequeñas, la investigación mineralógica se restringe a spots del tamaño del cristal, y por tanto los espectros Raman muestran información de una única fase cristalina. Por otro lado los espectros, en este trabajo se han adquirido espectros VNIR de zonas de un diámetro a aproximado de 1.5 cm, lo cual aumenta enormemente la probabilidad de encontrar varias fases en un único espectro. Se podría haber realizado un mapa Raman de las muestras para escanear regiones equivalentes a las de los espectros VNIR, pero esto hubiera requerido mucho tiempo además de estar fuera del alcance de esta tesis.

De cualquier modo, el principal objetivo de este análisis combinado era probar que las tres técnicas son totalmente complementarias y que pueden usarse simultáneamente para la caracterización de mineralogías ricas en sulfato y hierro sin

necesidad de preparar la muestra (salvo en la difracción de rayos-X), y con una resolución espacial que puede llegar en algunos casos hasta el tamaño del cristal (Raman). En muestras donde hay presentes varios sulfatos hidratados, Raman y DRX son un buen complemento a la reflectancia VNIR ya que pueden distinguir diferentes fases con menos ambigüedad. En muestras poco cristalinas, el Raman puede proporcionar una identificación mineral definitiva al superar las dificultades asociadas con el DRX en estas circunstancias.

El ruido y la línea base tienen que ser atenuados (o eliminados si es posible) tras la adquisición de un espectro Raman para eliminar la información espectral no asociada a la dispersión Raman. Además, los espectros ensanchados instrumentalmente deben ser procesados para reducir el ensanchamiento, y obtener un equivalente al verdadero espectro Raman. Existe software comercial (*e.g.* BRUKER Optics Inc., 2006; Thermo Fisher Scientific Inc., 2008) que permite realizar el tratamiento espectral necesario para recuperar sólo la información relacionada con las vibraciones moleculares. Sin embargo, este tipo de software incluye código propietario que ofrece interfaces gráficas poco intuitivas y difíciles de usar, junto con rutinas de cálculo rígidas que, desde nuestro punto de vista, hacen del tratamiento de espectros Raman una tarea tediosa donde el usuario pierde el control sobre el significado físico de los datos, en el mejor de los casos. Entendemos que cada espectro Raman es único, y por tanto se necesitan rutinas de tratamiento muy flexibles (aunque robustas) para su correcto análisis. Por esta razón hemos desarrollado nuestro propio software de post-procesado de espectros Raman. Las rutinas que se han concebido y desarrollado como parte fundamental de esta tesis se han aplicado sistemáticamente a todos los espectros adquiridos. Las rutinas se han implementado en in Microsoft's Visual Basic for Applications (VBA) (Clinick, 2001) de Excel. Los usuarios potenciales de este software sólo necesitan estar familiarizados con el entorno gráfico de Excel y el uso de hojas de cálculo para poder desarrollar un completo análisis de los espectros Raman a través del vistoso entorno gráfico que hemos desarrollado en el marco de Excel.

El software incluye rutinas de reducción de ruido basadas en la Transformada Rápida de Fourier, cálculos de la línea de base por medio de interpolación lineal,

posibilidad de auto-deconvolución Fourier, y capacidad para ajuste de bandas basada en el método de Marquardt. Además se ha desarrollado una rutina de comparación en base de datos para la estimación en-línea de los compuestos predominantes en mezclas minerales. La construcción de bases de datos exhaustivas por medio de sistemas de adquisición de espectros sistemáticos es una tarea crucial. Estamos trabajando en ello; se implementan espectros Raman de muestras orgánicas e inorgánicas en la base de datos continuamente. Nuestro software tarda menos de 1000 milisegundos en realizar un postprocesado profundo automático de los espectros Raman recién adquiridos usando procesadores actuales (*e.g.* Intel® Core™2 Duo), y es capaz de proporcionar la composición mineral de la muestra si se comparan los datos espectroscópicos con la base de datos adecuada.

B.2. Contribuciones de esta tesis

En resumen, las principales contribuciones de esta tesis son:

- El desarrollo e implementación de rutinas de procesado automático de espectros Raman. Las rutinas se han escrito en Microsoft Visual Basic for Applications y se accede a ellas a través de la interfaz de fácil uso proporcionada por Microsoft Excel.

- Una modelización exhaustiva basada en Raman de los equilibrios químicos, la especiación, y las propiedades de transporte de materia de soluciones sintéticas que se aproximan a la composición de muestras de agua afectadas por drenaje ácido de mina.

- Una caracterización detallada con espectroscopía Raman de muestras d agua de Río Tinto y minerales de hierro y sulfato de Río Tinto e Iron Mountain Mine.

- Un análisis combinado de sulfatos de Río Tinto mediante espectroscopía de reflectancia en el visible e infrarrojo cercano, espectroscopía Raman y difracción de rayos-X.

B.3. Líneas futuras

Los resultados que hemos presentado representan sólo el primer paso en el conocimiento y los avances que se pueden conseguir por medio de la investigación espectroscópica Raman en sistemas acuosos y minerales relacionados con el drenaje ácido de mina. Los novedosos resultados que hemos obtenido y discutido en esta tesis dan pie a la investigación de futuro sobre los temas tratados. En particular, los siguientes puntos pueden ser objeto de más investigación:

1. La caracterización sistemática de minerales naturales de hierro y sulfato por medio de espectroscopía Raman, espectroscopía de reflectancia en el visible e infrarrojo cercano, difracción de rayos-X, y LIBS (laser-induced breakdown spectroscopy), entre otras. Se he demostrado que estas técnicas son totalmente complementarias (*e.g.*, Figura 6.1). Unos análisis detallados de laboratorio en muestras sólidas naturales selectas revelaría propiedades importantes de las fases minerales presentes tales como la cristalinidad, estado de hidratación, substitución catiónica y descomposición térmica.

2. Estas propiedades se pueden correlacionar con la naturaleza de los sistemas acuosos a partir de los cuales se forman los minerales, permitiendo el establecimiento de modelos de precipitación (secuencias) para cada una de las fases minerales encontradas en las muestras de acuerdo a variaciones de temperatura día-noche y estacionales en el

campo. Estos modelos son en realidad una definición del rango de estabilidad medioambiental de cada mineral, *i.e.*, una clasificación de los minerales en función de su orden de precipitación, o de su solubilidad en un sistema acuoso dado. La aplicación inversa de estos modelos de precipitación a los actuales sulfatos marcianos podría por ejemplo ayudar a obtener una idea más clara de las características de las aguas ácidas que una vez inundaron la superficie de Marte, mediante la descripción de relaciones de fase en esas aguas.

3. Por medio de una comparación entre los modelos de precipitación de sulfatos sintéticos y naturales en el seno del drenaje ácido de mina y en el seno de soluciones acuosas de ese tipo, se podría obtener información sobre la ocurrencia de fases minerales y sus principales características, y correlacionar ésta con las condiciones de presión, temperatura, y actividad biológica (si existe) de los sistemas acuosos. En línea con algunos objetivos de NASA Astrobiology Roadmap, estos resultados podrían servir de base para futuros intentos de modelización de los sistemas acuosos ácidos marcianos a partir de cuáles se cree que se formó la mineralogía actual de Marte, y en los cuales la presencia de microorganismos podría haber jugado un papel clave.

4. Se puede determinar y correlacionar la composición química del drenaje ácido de mina y su mineralogía asociada con las propiedades de las bandas en los espectros Raman. Esto serviría de base para el establecimiento de protocolos de medida de la concentración de especies en aguas sulfúricas ácidas basadas en espectroscopía Raman. Esta técnica podría ser extremadamente útil para una detección rápida y precisa de los productos del drenaje ácido en escenarios mineros, y asimismo representar una gran mejora en el actual estado-del-arte de la descripción del drenaje ácido de mina.

5. Es posible mejorar notablemente las medidas experimentales de concentración de especies y la geometría instrumental en los experimentos de difusión. La relación señal ruido y, muy probablemente, el límite de detección podrían ser mejoradas usando un cabezal microRaman para recoger la luz dispersada. Con respecto al modelo de difusión, el siguiente paso que estamos considerando consiste en conectar el modelo propuesto en esta tesis, o una versión revisada del mismo, con un modelo general termodinámico del equilibrio, especiación, y difusión en mezclas líquidas multicomponente.

6. La mejora de las rutinas de procesado de espectros Raman. Esto es necesario para avanzar en la automatización de las operaciones en los datos Raman y para minimizar la interacción del usuario en el proceso, manteniendo a la vez precisión y exactitud en el modelizado de las propiedades de las bandas Raman. Por otro lado, sería muy interesante construir librerías detalladas de muestras mediante programas sistemáticos de adquisición de espectros Raman, LIBS y VNIR, y patrones de difracción para conseguir una identificación más precisa de minerales mediante versiones posteriores, y mejoradas, del software que hemos presentado.

Appendix C

resumen

C.1. Capítulo 1: Introducción: contexto histórico y geo/bioquímico de la zona de Río Tinto, España

El Río Tinto debe su nombre al intenso color rojo de sus aguas, que fluyen a través de la Faja Pirítica Ibérica (Figura 1.1), una de las mayores formaciones de compuesto de azufre (Boulter, 1996; Leistel *et al.*, 1998). La Faja Pirítica Ibérica se extiende a lo largo de un área de más de 250 km de longitud, y su anchura alcanza los 75 km en algunos puntos. Se han encontrado más de 80 depósitos masivos de azufre, además de 300 depósitos de manganeso (Mellado *et al.*, 2006). Las minas de Río Tinto son probablemente las minas más antiguas del mundo. Al menos la riqueza mineral de la zona era legendaria ya en la Edad de Bronce, y de acuerdo con la mitología, éstas son las "minas del Rey Salomón". Independientemente de mitos o leyendas, es un hecho contrastado que la compañía británica Rio Tinto Company convirtió las minas de Río Tinto en uno de las mayores fuentes de hierro, cobre y azufre del mundo (Avery, 1974).

La intensiva actividad minera desarrollada en Río Tinto durante más de 5000 años (Avery, 1974) es la causa directa de la inusual acidez del río (pH medio de 2.3 (Amils *et al.*, 2002)) y de su color rojo. O al menos eso se pensaba. Los minerales de la superficie y el subsuelo proporcionan al área trazas de color azul, verde, amarillo, rojo y marrón (Figuras 1.4 a 1.8). Los procesos químicos que facilitan la formación de minerales de estas características se pueden resumir en el siguiente conjunto de reacciones (Nordstrom *et al.*, 2000):

$$2FeS_2 + 7O_2 + 2H_2O \rightarrow 2FeSO_4 + 2H_2SO_4 \quad (C.1)$$

$$2Fe^{2+} + 1/2\ O_2 + 2H^+ \rightarrow 2Fe^{3+} + H_2O \quad (C.2)$$

$$Fe^{3+} + 3H_2O \rightarrow Fe(OH)_3 + 3H^+ \quad (C.3)$$

$$FeS_2\ (s) + 15/4\ O_2 + 7/2\ H_2O \leftrightarrow 4H^+ + 2SO_4^- + Fe(OH)_3\ (s) \quad (C.4)$$

Esta es una receta típica para el drenaje ácido de mina (AMD). Como se observa en la Ecn (C.4) se liberan 4 moles de acidez por cada mol de pirita que se oxida.

Se diseñaron e incluso se financiaron programas de recuperación para mitigar el impacto medioambiental del AMD en las zonas mineras (Serrano *et al.*, 1995). En particular, las plantas y animales acuáticos se ven en gran medida perjudicados, y los acuíferos subterráneos se contaminan como consecuencia del AMD. Sin embargo, no toda la fauna acuática se ve afectada por el AMD. Hay una serie de microorganismos que desempeñan un papel crucial en los procesos de oxidación-reducción previamente descritos. De hecho, se cree que estos organismos (autótrofos) son la verdadera causa de las condiciones actuales de Río Tinto (López-Archilla *et al.*, 2001; Amils *et al.*, 2002).

El descubrimiento de hidróxidos/oxihidróxidos férricos, jarositas (sulfatos con contenido en hierro formados en ambientes acuosos) y otros minerales ricos en sulfato en la región Meridiani es la evidencia de que en algún momento fluyó agua líquida por la superficie de Marte (Klingelhöffer *et al.*, 2004; Rieder *et al.*, 2004; Lane *et al.*, 2004; Clark *et al.*, 2005). Dada la asociación de microorganismos tales como el *Acidithiobacillus ferrooxidans* con la oxidación acuosa de sulfuros en Río Tinto, e independientemente de que los sulfatos marcianos se hayan o no formado mediante procesos asistidos biológicamente, parece claro que los depósitos de sulfatos precipitados en Marte son los lugares idóneos para la búsqueda de vida pasada en el Planeta Rojo. En este contexto, Río Tinto se perfila como un escenario excelente donde los procesos (inorgánicos y bio-asistidos) que provocan la aparición de sulfatos en la Tierra pueden ser descritos y comprendidos.

C.2. Capítulo 2: Introducción: metodología e instrumentación

C.2.1. Fundamentos de espectroscopía Raman

La espectroscopía Raman ha experimentado un renacimiento importante debido fundamentalmente a los avances tecnológicos en láseres, detectores y sistemas ópticos. Sir Chandrasekhara Venkata Raman (Raman and Krishnan, 1928) demostró por primera vez la dispersión inelástica de luz, si bien el hecho fue descubierto simultáneamente por Grigory Landsberg and Leonid Mandelstam (Landsberg and Mandelstam, 1928).

Cuando la luz incide sobre una muestra, una pequeña fracción de los fotones incidentes (10^{-5} a 10^{-9}) interacciona con las vibraciones moleculares de la muestra y se dispersa a mayores o menores energías (dispersión Raman). La espectroscopía Raman consiste en cuantificar la diferencia energética entre la luz incidente y los fotones dispersados. Esta diferencia corresponde a transiciones vibracionales. Un espectro Raman es una representación de la intensidad de la radiación dispersada Raman en función de la diferencia de frecuencia con respecto a la radiación incidente. Esta diferencia se conoce como desplazamiento Raman, y se expresa habitualmente en unidades de número de onda, cm^{-1}.

Un espectrómetro Raman se compone típicamente de tres partes: el láser, el dispositivo recolector de luz y el espectrógrafo. Se utiliza luz láser porque proporciona radiación monocromática con la intensidad suficiente para generar una cantidad significante de luz dispersada Raman. Un cabezal recoge esta luz, filtra la luz no dispersada y envía la información Raman al espectrógrafo. Éste elemento separa espacialmente las diferentes longitudes de onda del haz recogido y las proyecta en un detector que recoge la intensidad de la señal Raman a cada longitud de onda individual.

Existen en la bibliografía excelentes libros de referencia sobre la teoría e instrumentación Raman (Woodward, 1967; Chantry, 1971; Gilson and Hendra, 1972; Clark, 1975; Long, 1977). En esta sección nos hemos centrado en la espectroscopía

Raman de una molécula de importancia capital en este tesis, el sulfato, y en la instrumentación empleada en este trabajo.

C.2.2. Espectroscopía Raman del ión sulfato

El ión sulfato consiste en un átomo central de azufre rodeado por cuatro átomos de oxígeno dispuestos en configuración tetraédrica. El ión sulfato libre corresponde al grupo puntual T_d, de gran simetría. Sus cuatro modos de vibración fundamentales son activos en Raman (Nakamoto, 1997), y se representan en la Figura 2.2.

Existen numerosos trabajos en la literatura sobre los iones sulfato y bisulfato en solución acuosa, incluyendo sus equilibrios (*e.g.* Irish and Chen, 1970; Chen and Irish, 1971a, 1971b; Davis *et al.*, 1974; Dawson *et al.*, 1986; Haldna *et al.*, 1987; Myhre *et al.*, 2003). Todos estos trabajos comparten la asignación de bandas para las vibraciones moleculares de los iones sulfato y bisulfato. Dicha asignación se recoge en la Tabla 2.1., y es la que se usa a lo largo de esta tesis.

Si la simetría del ión sulfato se reduce por efecto de solvatación, "metal complexation", o protonación, se aprecian cambios en el perfil de los espectros Raman asociados. Chio *et al.* (2005) y Wang *et al.* (2006) han demostrado que los picos asociados a los modos fundamentales de stretching del sulfato sufren un desplazamiento hacia menores números de onda cuando aumenta el grado de hidratación de la molécula. Frost *et al.* (2000, 2005, 2006b) han publicado estudios espectrales exhaustivos de diferentes sulfatos, naturales y sintéticos. Sin embargo, es claro que los espectros Raman de muestras naturales difieren considerablemente de los espectros de muestras sintéticas. Además, los diferentes procesos geoquímicos de formación y degradación de los materiales y las diferentes geometrías experimentales, instrumentos, etc., quedan invariablemente reflejados en los espectros Raman. Por esta razón, en lugar de utilizar asignaciones de bandas publicadas en la literatura, en esta tesis se han analizado los espectros Raman de los minerales de forma individual,

buscando en cada uno de ellos las signaturas espectrales de vibraciones moleculares conocidas.

C.2.3. Instrumentación Raman

En este trabajo se han utilizado varios equipos Raman con el fin de obtener los mejores resultados posibles. Los factores determinantes a la hora de seleccionar un equipo para realizar determinadas medidas experimentales fueron las características propias de las muestras a analizar y la naturaleza del estudio. Los principios de funcionamiento de los equipos utilizados se describen esquemáticamente en la Figura 2.3. En las secciones 2.3.1 a 2.3.4 se detallan los equipos utilizados en las Universidades de Valladolid (España), Oslo (Noruega) y Hawaii (USA) y en el centro SETI (USA).

C.2.4. Técnicas complementarias

C.2.4.1. Espectroscopía de reflectancia en el visible e infrarrojo cercano (VNIR)

Cuando la luz solar incide en la superficie de un material, se puede transmitir, absorber o reflejar. Qué longitudes de onda sufren qué fenómeno, depende del material. Un espectro de reflectancia de un material es una representación de la fracción de radiación reflejada en función de la longitud de onda de la radiación incidente y sirve como signatura única del material. Los espectros de reflectancia se midieron usando un FieldSpec®ProFR de Analytical Spectral Devices (ASD) con una sonda y un fuente de luz solar simulada.

C.2.4.2. Difracción de rayos-X

La técnica DRX es una herramienta capaz de identificar la composición elemental y la orientación cristalográfica de una muestra. Cuando los rayos-X interaccionan con la materia se obtiene un patrón de difracción de los mismos. Los rayos difractados poseen información angular y de intensidad. El instrumento de DRX usado para los análisis mineralógicos es un Terra (inXitu Inc.), también conocido como “mini-Chem” ya que se basa en el mismo concepto que el Chemin IV, una versión portátil del instrumento Chemin a bordo de la misión MSL de NASA.

C.3. Capítulo 3: Desarrollo de software

C.3.1. Introducción

Un espectro Raman típico se puede considerar como la respuesta en forma de señal a cierto estímulo, dada por un sistema físico. En la mayoría de los casos, la entrada se compone no sólo de información proveniente de la muestra sino por señales de fondo. Por otro lado, el instrumento de medida introduce cierto ruido que se refleja invariablemente en los espectros como una línea base, aunque también podría contribuir de otras formas. Como consecuencia, un espectro Raman como el mostrado en la Figure 3.1 es el resultado de la combinación de una señal determinística, o información Raman de la muestra, y otras contribuciones. En las secciones siguientes se muestran las bases matemáticas y físicas del software que se ha desarrollado con el fin de minimizar el impacto del ruido y las señales de fondo en los espectros Raman.

Todos los espectros Raman adquiridos a los largo de esta tesis fueron pre-procesados para obtener la máxima información Raman. Los espectros fueron tratados mediante una serie de rutinas para eliminar el ruido y la línea base. Se aplicaron rutinas de auto-deconvolución Fourier y ajuste de bandas para tratar los espectros cuando se requería información cuantitativa. Aunque las rutinas para el procesado de los espectros Raman se pueden automatizar, y de hecho han sido automatizadas para determinadas aplicaciones (Sobron *et al.*, 2008a), a menudo se requiere la interacción con el usuario para un tratamiento de datos refinado. Hemos desarrollado una aplicación basada en el lenguaje de programación de macros llamada VBA para Microsoft Office Excel. Las posibilidades de la programación en VBA en Excel proporcionan una interfaz cómoda para el usuario que permite usar datos desde la misma hoja de cálculo como parámetros de control de las rutinas de procesado de espectros descritas en las secciones 3.2 a 3.5. La hoja de cálculo se convierte pues en una interfaz al código, permitiendo una fácil interacción con el código y con lo que calcula (Figura 3.14).

C.3.2. Mejora de la relación señal-ruido

Un procedimiento de mejora de la relación señal-ruido (SNR) necesita de una caracterización precisa de la componente de ruido de la señal. El ruido es una señal aleatoria distribuida a lo largo de todo el rango espectral que se superpone a las bandas Raman. Sin embargo, en un dominio transformado mediante una transformada de Fourier, el ruido se localiza en la zona de tiempos cortos, mientras que la información Raman se encuentra en la región de tiempos largos, tal y como explica el análisis de Fourier (Ewing, 1997). El objetivo es truncar el espectro en el dominio transformado para conservar sólo la información Raman. Una vez se realiza la transformada inversa del espectro truncado, el ruido se reduce considerablemente mientras que las bandas Raman se conservan prácticamente igual.

C.3.3. Supresión de la línea base

Al igual que en caso de la mejora de SNR, se necesita una buena caracterización de la línea base para evitar la pérdida de información. La rutina para la supresión de línea base incluida en el software desarrollado genera una línea base mediante interpolación lineal a partir de un determinado número de puntos espectrales, que luego es sustraída punto a punto del espectro. Los puntos que se usan en la construcción de línea base son típicamente algunos de los mínimos de intensidad locales, que se calculan de nuevo usando rutinas basadas en la Transformada Rápida de Fourier o FFT.

C.3.4. Comparación con bases de datos

Se ha implementado una base de datos (BD) que contiene parámetros espectrales Raman de la mayoría de los minerales que se sabe (o se especula) existen en Marte y en los análogos marcianos ricos en sulfatos. El proceso de comparación de los espectros recogidos con la base de datos es una versión preliminar del software de

vuelo que se incorporará a bordo de la misión ExoMars, concretamente en el instrumento Raman/LIBS. Se necesita desarrollar las rutinas más robustas y adecuadas para solventar problemas como el más que probable pobre SNR de los espectros Raman en Marte. La prueba de instrumentos Raman de tipo "vuelo" en condiciones de atmósfera marciana (mediante cámaras de simulación) será crucial para comprender la respuesta de los instrumentos en condiciones de misión, y ayudará sin duda a mejorar el software para la detección automática de fases minerales en la superficie de Marte. Aunque la rutina de comparación que aquí se presenta está consagrada al instrumento Raman/LIBS de ExoMars, se puede extrapolar a cualquier aplicación que requiera una identificación mineral automática a partir de espectros Raman.

En la actualidad, nuestra BD está organizada como una matriz estructurada de campos que contiene información relacionada con más de setenta compuestos y la intensidad, anchura y posición de la(s) banda(s) asignadas a ellos. Los campos se distribuyen tal y como se muestra en la Tabla 3.1. La rutina de comparación compara cada banda de la BD con todas las bandas del espectro bajo análisis.

C.3.5. Auto-deconvolución Fourier de bandas y ajuste de bandas

Como se explica en la sección 3.1, el sistema de medida y la geometría del experimento, entre otros, afectan invariablemente a los espectros Raman. Más concretamente, el ensanchamiento instrumental de bandas es común en las medidas Raman que se basan en espectrómetros de tipo dispersivo, como los usados en esta tesis. Este ensanchamiento de bandas se puede reducir hasta el punto que bandas completamente superpuestas se pueden resolver mediante un proceso llamado deconvolución de Fourier.

C.4. Capítulo 4: Soluciones y aguas ácidas sulfúricas

Este capítulo describe el estudio de sistemas ácidos acuosos llevado a cabo en esta tesis. Se han investigado muestras sintéticas y naturales. Se ha analizado la físico-química de dos sistemas sintéticos de especial relevancia en el marco del drenaje ácido de mina: sulfato de hierro(II)-ácido sulfúrico-agua y hierro(III)-ácido sulfúrico-agua. Las propiedades de transporte de materia de un tercer sistema, ácido sulfúrico-agua se han caracterizado. Además, se ha analizado la espectroscopía Raman de muestras selectas de agua de Río Tinto.

C.4.1. Equilibrios termodinámicos en el sistema sulfato de hierro(II)-ácido sulfúrico-agua

El sistema simplificado representa una buena primera aproximación a la hidrogeoquímica de Rio Tinto puesto que están involucrados dos de las especies mayoritarias en el agua de Rio Tinto: hierro(II) y sulfato. La caracterización de este sistema se basa en la identificación de las especies químicas principales y la determinación de sus concentraciones en sus estados básicos de equilibrio. La espectroscopía Raman es una herramienta ideal para el estudio de soluciones acuosas ya que la mayoría de especies moleculares originan bandas únicas y características en los espectros Raman. La técnica Raman también permite una identificación en tiempo real de las especies y una rápida cuantificación de su abundancia. Además, debido a la naturaleza no-invasiva y no-destructiva de la técnica, los equilibrios en el sistema no se ven afectados por las medidas.

Se han preparado varias soluciones de ácido sulfúrico que contienen sulfato de hierro(II) en el rango 0 a 1.65 mol/kg, y se han realizado análisis cualitativos y cuantitativos de los iones presentes mediante espectroscopía Raman. Las características intrínsecas de la técnica Raman permiten la identificación de las especies en solución por medio de un ajuste de bandas sobre los espectros Raman. Se ha calculado además el producto de coeficientes de actividad del mencionado sistema

en función de la concentración de sal, y se han corroborado algunos resultados previamente publicados sobre la formación de complejos de hierro(II) hexahidratados.

C.4.2. Especiación en el sistema hierro(III)-ácido sulfúrico-agua

Los complejos procesos de interacción entre bacterias extremófilas y el substrato del área de Río Tinto aceleran la oxidación de hierro(II) a hierro(III) (González-Toril *et al.*, 2003). El sistema hierro(III)-ácido sulfúrico-agua representa una buena aproximación a las soluciones acuosas de Río Tinto ya que el hierro(III) y el ión sulfato son dos de los principales componentes de las aguas altamente ácidas (López-Archilla *et al.*, 1993). La espectroscopía Raman permite obtener una precisión y una repetibilidad que son críticas para los análisis cualitativos y cuantitativos. En particular, las vibraciones moleculares de los complejos de hierro(III) quedan determinadas por longitudes de onda específicas en los espectros Raman. Los cambios en la intensidad y la anchura de las bandas en los espectros se cuantifican de forma rápida. Además, las soluciones no requieren preparación anterior a la adquisición de espectros, lo cual es muy importante en potenciales análisis *in-situ* de entornos contaminados por el drenaje ácido de mina.

Se han preparado soluciones sintéticas que se asemejan a las condiciones reales del agua de Río Tinto con ácido sulfúrico 0.09 mol/kg y concentraciones variables de hierro(III) en el rango 0.01 a 1.5 mol/kg. Los espectros Raman de las soluciones revelan un fuerte interacción hierro(III)-sulfato a nivel de esfera interior a través de la banda del sulfato a 981 cm^{-1} y un hombro a 1005 cm^{-1}. La interacción hierro(III)-sulfato también puede ser facilitada mediante puentes de hidrógeno y cuantificada en los espectros Raman a través de la banda de stretching simétrico del bisulfato a 1052 cm^{-1} y un hombre a 1040 cm^{-1}. Se encuentran otras bandas en la región de bajas frecuencias de los espectros Raman que se atribuyen igualmente a la formación de complejos con puentes de hidrógeno.

C.4.3. Difusión de especies moleculares en el sistema ácido sulfúrico-agua

Se ha propuesto y validado un modelo de difusión de las especies químicas disueltas en el sistema acido sulfúrico-agua con medidas experimentales Raman de la concentración de iones sulfato y bisulfato. La optimización del modelo proporciona unos coeficientes de difusión que son funciones lineales de las concentraciones, aunque el equilibrio termodinámico entre especies sea una función compleja de la concentración de ión sulfato.

Los procesos de difusión o transporte de materia implican el transporte de moléculas como respuesta a un gradiente de concentración dentro de un sistema físico. Estos procesos juegan un papel determinante en muchos campos de la física y la química, siendo la descarga posterior difusión de ácido y metales en sistemas acuáticos un tema de enorme importancia en aspectos medioambientales. El drenaje ácido de roca (ARD) es un buen ejemplo de contaminación de aguas fluviales y de acuíferos. Cuando los sulfuros metálicos son oxidados y hay suficiente agua para movilizar los iones disueltos, se produce ácido sulfúrico. Aunque el ARD es un proceso puramente natural, determinadas actividades humanas como la minería aceleran las reacciones geoquímicas que lo producen a base de exponer minerales al aire y al agua a través de las minas y los desperdicios que generan.

El ácido sulfúrico generado en los procesos de ARD se disocia rápidamente en sulfato y bisulfato, tal y como se explica en la sección 4.2, siendo esta disociación la causa directa de la acidificación de las aguas. La acidificación ocurre cuando las soluciones acuosas que contienen SO_4^{2-}, H^+, Fe^{2+} difunden en aguas corrientes Nordstrom and Alpers, 1999b). Los contaminantes disueltos migran hacia aguas de superficie y subsuelo mediante fenómenos difusivos. Sería muy interesante modelizar estos procesos con el fin de predecir las propiedades del ARD basadas, por ejemplo, en la tasa de formación de ácido. Estos modelos deben tener en cuenta todas las especies (mayoritarias y minoritarias) en solución, además de los procesos de asociación-disociación entre ellos. Estos sistemas son mezclas líquidas multicomponente no ideales cuya estructura no se conoce principalmente porque hay una gran

incertidumbre en los datos disponibles para los coeficientes de actividad en sistemas multicomponente.

En esta tesis nos hemos centrado en el estudio de las propiedades de difusión del sistema acuoso más simple que se aproxima al ARD, ácido sulfúrico-agua, como punto natural de partida para modelizar la físico-química de la difusión en el ARD. Hemos propuesto un modelo de difusión de ácido sulfúrico acuoso en agua que (1) se basa en la difusión individual de las especies moleculares presentes en el sistema, (2) tiene en cuenta los fenómenos de asociación-disociación entre dichas especies y (3) hace uso un coeficiente efectivo de difusión no constante. Asumimos que el coeficiente de difusión es una función lineal de la concentración de las especies, lo que es práctica común cuando se describen procesos físicos. De hecho, esta dependencia lineal se confirma experimentalmente. Llamamos efectivo al coeficiente de difusión ya que deja de ser una propiedad física para convertirse en un parámetro del modelo asociado a la difusión de una especie individual *i* en un medio compuesto por todas las especies (agua, sulfato, bisulfato y protones). El coeficiente efectivo de difusión se usa como parámetro ajustable que se optimiza para minimizar la desviación entre los valores de la concentración de las especies calculados teórica y experimentalmente como función del tiempo y el espacio. Las concentraciones experimentales se calculan como perfiles temporales por medio de la espectroscopía Raman. Esta técnica permite una medida directa y rápida de la concentración absoluta de las especies en el sistema, y al ser no invasiva no afecta los equilibrios entre especies.

C.4.4. Espectroscopía Raman del agua de Río Tinto

La técnica Raman permite un análisis efectivo y rápido de soluciones acuosas naturales, sin necesidad de preparación. Las muestras de agua de Rio Tinto analizadas provienen de antiguas zonas mineras y presentan una acidez elevada y un color rojo en la mayoría de los casos. Se han encontrado cantidades variables de sulfato y bisulfato en las muestras, que sugieren diferentes niveles de acidez. Además se han calculado

las concentraciones relativas de ambos iones. Los resultados están acorde con otros trabajos publicados sobre aguas ácidas, y prueban la importancia de la espectroscopía Raman como herramienta para análisis preciso y no invasivos de aguas ácidas.

C.5. Capítulo 5: Mineralogía asociada a aguas ácidas

En este capítulo de presentan las investigaciones en muestras naturales de minerales ricos en sulfato seleccionadas de Río Tinto y de otro entorno característico del drenaje ácido de mina, the Richmond Mine en Iron Mountain, California. Además, presentamos un estudio combinado Raman/Reflectancia/Difracción de rayos-X de muestras minerales de Río Tinto.

C.5.1. Espectroscopía Raman de sales eflorescentes de sulfato del Iron Mountain Superfund Site, California

Iron Mountain, California, alberga grandes depósitos de sulfuros que fueron explotados para la extracción de cobre, zinc, oro, plata y pirita (para ácido sulfúrico) entre los años 1860s y principios de los 1960s. La Richmond mine en Iron Mountain se caracteriza por tener aguas extremadamente ácidas, con (pH de 0.5) y que contienen grandes cantidades de sulfato, hierro, y otros metales (Alpers *et al.*, 2003).

El estudio de las eflorescencias ricas en sulfato es importante para comprender los equilibrios de fase líquido-sólido en entornos contaminados por drenaje ácido de mina; esto puede ayudar indudablemente al desarrollo de protocolos de recuperación y puede facilitar la detección precoz de contaminación por aguas ácidas. En este trabajo presentamos y discutimos los espectros Raman de sales eflorescentes de sulfato recogidas en Richmond Mine en Iron Mountain, California. A partir de los espectros Raman de las muestra se han identificado compuestos como la coquimbita, melanterita, copiapita y voltaíta.

C.5.2. Espectroscopía Raman, espectroscopía por reflectancia en el visible e infrarrojo cercano (VNIR), y difracción de rayos-X (DRX) de sales eflorescentes y precipitados de sulfato de Río Tinto

El entorno de Río Tinto se caracteriza por la presencia de precipitados y eflorescencias ricas en sulfato. En este trabajo se han caracterizado varias de estas muestras mediante espectroscopía Raman, habiéndose encontrado fundamentalmente yeso y otros óxidos hidratados de hierro(II)/(III) pertenecientes al grupo de la copiapita.

Un subconjunto de sulfatos de Río Tinto se sometió a un análisis combinado mediante las técnicas Raman, VNIR y DRX. Estas técnicas han sido, y hasta cierto punto aún son, consideradas como técnicas de laboratorio. Sin embargo se han diseñado en los últimos tiempos sistemas específicos para uso en el campo y en exploración planetaria, en modo de contacto o remoto. En este contexto, el instrumento de contacto combinado Raman/LIBS ha obtenido la calificación de "Instrumento Fundamental" para la misión ExoMars de ESA, y el difractómetro de rayos-X está asimismo considerado como "Instrumento Muy Importante" (ESA Pasteur Progress Letter 4, 2004). La espectroscopía por reflectancia también ah demostrado durante muchos años ser una herramienta mineralógica muy sensible para estudios geológicos y geoquímicos de superficies planetarias (Gendrin *et al.*, 2005).

Las pequeñas diferencias observadas de la interpretación de los resultados que las tres técnicas han obtenido sobre las muestras naturales de Río Tinto permiten obtener una perspectiva global de la composición mineralógica de las muestras. Los componentes mayoritarios encontrados en las muestras son yeso, K-jarosita, copiapita, ferricopiapita y goetita. Además se ha detectado Na-jarosita, ferryhidrita y cuarzo en cantidades menores. Las tres técnicas utilizadas en este trabajo nos han permitido obtener una identificación única y precisa de la composición química de los sulfatos naturales, justificando por tanto su uso combinado.

Unidad Asociada
Universidad de Valladolid-CSIC a través del Centro de Astrobiología (CSIC-INTA)